Cell cycle dynamics regulate H3K27 and H3K9 histone modifications

Liyne Nogay [1, 2], Ananthakrishnan Vijayakumar Maya § [1, 2], Lara Heckmann § [1, 2], Francesco Cardamone [1, 2, 3], Isabelle Grass [1, 4], Aakriti Singh [1, 2], Anna Frey [1, 5], Laurin Ernst [1, 2], Nicola Iovino [3, 4], Anne-Kathrin Classen [1, 4, *]

§ shared co-authors

* corresponding author: anne.classen@biologie.uni-freiburg.de

1 Faculty of Biology, University of Freiburg, Freiburg, Germany

2 International Max Planck Research School for Epigenetics, Biophysics and Metabolism, Freiburg, Germany

3 Max Planck Institute of Immunobiology and Epigenetics, Freiburg, Germany

4 CIBSS Centre for Integrative Biological Signalling Studies, University of Freiburg, Freiburg, Germany

5 Spemann Graduate School of Biology and Medicine (SGBM), University of Freiburg Germany

ABSTRACT

Cell cycle progression presents a fundamental challenge to genome integrity, particularly due to the need to reestablish post-translational histone modifications (PTMs) following DNA replication. Although proliferative and differentiating tissues exhibit markedly different cell cycle dynamics, how these differences shape the histone modification landscape in vivo remains largely unexplored. Here, we show that levels of H3K27ac, H3K27me3, and H3K9me3 are tightly linked to cell cycle dynamics in the *Drosophila* wing imaginal disc. We demonstrate that both physiological and pathological elongation of the cell cycle led to an accumulation of H3K9me3 and H3K27me3, whereas cell cycle acceleration reduces their levels. In contrast, H3K27ac exhibits the opposite pattern: levels decrease in arrested cells and increase with faster cycling. Genome-wide CUT&Tag analysis reveals that these changes predominantly affect genomic loci already modified in normally proliferating tissue. Importantly, the regulation of methylation levels at H3K9 and H3K27 is not solely mediated by the cell cycle machinery but reflects a metabolically guided process in which the rate of methylation is coupled to the rate of cell proliferation through metabolic activity, including signaling via the Insulin/PI3K/Akt pathway. Our study thus reveals key principles for understanding histone methylation in proliferating, senescent, and differentiating cells. In contrast, H3K27 acetylation is regulated through a distinct, cell cycle-coupled mechanism. We find that CBP/Nejire-mediated acetylation of H3K27 peaks during S-phase and is reversed by HDAC1, as cells exit replication. Disruption of this acetylation cycle leads to replication stress and a G2 cell cycle arrest via a DNA damage checkpoint. Notably, this genome-protective function of CBP/Nejire depends specifically on acetylation of the H3K27 residue itself, revealing a novel role for H3K27ac beyond its well-established function in transcriptional activation. Together, our findings establish a robust link between cell cycle progression and histone modification dynamics, highlighting the necessity of maintaining balanced PTM levels under varying proliferative states. These insights have broad implications for our understanding of development, aging, and tumor growth.

INTRODUCTION

The cell cycle and the regulation of chromatin need to be tightly coordinated preserve epigenetic integrity. Specifically, progression through S-phase poses several challenges: chromatin must become transiently accessible for DNA replication, pre-existing post-translationally modified histones must be evenly distributed between daughter genomes and newly incorporated histones must acquire appropriate modifications to compensate for the semi-conservative dilution of modifications. These demands are complicated by the fact that cell cycle progression and dynamics differ drastically across biological contexts, ranging from rapid divisions in embryonic and regenerating tissues to complete arrest in terminally differentiated cells. How chromatin states are maintained across diverse proliferative tissue environments *in vivo* is still insufficiently understood.

In actively proliferating tissues, entry into the cell cycle at the G1/S transition, and progression through subsequent cycle phases, are tightly regulated. This regulation is mediated by Cyclins and Cyclin-dependent kinases (CDKs), as well as retinoblastoma (Rb) proteins and E2F transcription factors. Throughout the cell cycle, specific checkpoints respond to growth factors or cell size to modulate the rate of proliferation, as well as to DNA damage or chromosome misalignment to maintain the integrity of the genome (Matthews et al., 2022, Tapon et al., 2001, Lee and Orr-Weaver, 2003). As cells enter stages of differentiation, quiescence or senescence, they typically withdraw from active cycling by either prolonging their G1 phase or entering a stable cell cycle arrest known as G0. This transition away from proliferation often involves cyclin-dependent kinase (CDK) inhibitors, such as p21 and p27, which are intricately linked to gene expression programs that guide cell fate determination and differentiation (Buttitta and Edgar, 2007, Huang et al., 2022, de Morree and Rando, 2023, Ma et al., 2015). Progression through the cell cycle presents significant challenges for chromatin organization and epigenetic regulation - especially during S-phase but also during mitosis. Specifically, during S-phase, chromatin must become highly accessible to facilitate replication fork progression, nucleosome redistribution and de novo nucleosome incorporation in the replicated genomes (Stewart-Morgan et al., 2020, Alabert et al., 2015, Reveron-Gomez et al., 2018, Ma et al., 2015, Escobar et al., 2021, Ramos-Alonso and Chymkowitch, 2024). In contrast, in mitosis, chromatin must be tightly compacted to ensure accurate chromosome segregation (Ramos-Alonso and Chymkowitch, 2024, Zhou and Heald, 2020). Central to the regulation of chromatin organization are post-translational histone modifications (PTMs), which are also epigenetic regulators of transcriptional silencing and gene activation (Millan-Zambrano et al., 2022, Bhatnagar et al., 2023, Lopez-Hernandez et al., 2025). It is well-established that PTM dysregulation can lead to cell cycle defects by disrupting chromatin organization and entire gene regulatory networks (Brookes and Shi, 2014, Cavalli and Heard, 2019, Feinberg et al., 2016, Peterson and Laniel, 2004). While much attention has been dedicated to understanding how PTM dysregulation can drive pathogenesis by altering the expression of genes central to cell cycle regulation, less is known about how cell cycle dynamics connect to the maintenance and re-establishment of histone modifications. Yet, studies of the cell cycle-dependent regulation of the histone

methyltransferase PR-Set7 and histone demethylase PHF8 underscore the capacity of the cell cycle machinery to control specific histone modifications and thereby maintain chromatin function (Oda et al., 2010, Liu et al., 2010).

Some of the most abundant PTMs that regulate chromatin accessibility and transcriptional activity are acetylation and methylation of lysine residues on histone tails. While several lysine residues in histones can be acetylated or methylated, research has most strongly focused on dynamic acetylation and methylation of lysines 9 and 27 on histone H3 (H3K9 and H3K27), which represent some of the functionally most important histone modifications. In most species, trimethylation of H3K27 is mediated by Polycomb Repressive Complexes and relies on histone methyltransferases of the Enhancer of zeste E(z) family. H3K27me3 maintains the silencing of many genes required for cell fate specification during development, most famously Hox genes (Blackledge and Klose, 2021, Sparmann and van Lohuizen, 2006, Muller et al., 1995, Beuchle et al., 2001, Cao et al., 2002). In contrast, trimethylation of H3K9 (H3K9me3) is mediated by the enzymatic activity of Su(var)3-9 and is central to the formation and maintenance of constitutive heterochromatin at telomeres, centromeres and repetitive repeats (Padeken et al., 2022, Aagaard et al., 1999, Ebert et al., 2004). In *Drosophila*, H3K27 acetylation is mediated by the histone acetyltransferase (HAT) Nejire (Nej), a homolog of mammalian p300/CBP, and is reversed by the histone deacetylase HDAC1/Rpd3 (Willnow and Teleman, 2024, Petruk et al., 2001, Tie et al., 2009, Ciabrelli et al., 2023). H3K27ac is strongly associated with active promoters and enhancers, where it is thought to facilitate chromatin opening and transcriptional activation (Holmqvist and Mannervik, 2013, Philip et al., 2015, Boija et al., 2017, McConnell et al., 2012, Chen et al., 2022). As a consequence of these important functions, dysregulation of H3K9me3, H3K27me3 and H3K27ac is a common feature in cancer or other diseases characterized by alterations and defects in cell proliferation. Yet, importantly, it often remains unclear if defects in epigenetic modifications cause altered proliferation defects or if vice versa proliferation defects cause defects in epigenetic modifications (Brookes and Shi, 2014, Cavalli and Heard, 2019, Feinberg et al., 2016, Classen et al., 2009). Disentangling this relationship is key to understanding how epigenetic and proliferative states influence one another in development and disease.

Importantly, the semi-conservative nature of DNA replication during S-phase has a profound impact on the landscape of these histone modifications. As the DNA is duplicated, pre-existing histones bearing PTMs are equally distributed onto the newly synthesized strands. Naïve, newly synthesized histones are integrated to ensure proper packaging of the duplicated genomes but also necessitating the reestablishment of the now diluted PTM code (Escobar et al., 2021, Alabert and Groth, 2012, Escobar et al., 2019, Wenger et al., 2023). To reestablish the epigenetic histone modification landscape after incorporation of newly synthesized, naive histones, histone-modifying enzymes act post-replication by using the modifications on old recycled histones as a template to modify the newly incorporated histones (Stewart-Morgan et al., 2020, Annunziato, 2015, Flury and Groth, 2024). Importantly, in cultured cells, histone acetylation marks are typically restored immediately after replication often via a transcription-

124 dependent process, while histone methylation is generally re-established during subsequent gap phases
125 (Alabert et al., 2015, Zee et al., 2012, Reveron-Gomez et al., 2018, Petruk et al., 2013).
126
127 Of note, strong acetylation of newly synthesized histones plays a specific cell-cycle-dependent role during
128 S-phase. Hyperacetylation, for example at H4K5, H4K12, H3K14, H3K23 or H3K56, is observed during S-
129 phase and facilitates recognition of newly synthesized histones by histone chaperone complexes,
130 promoting their correct incorporation into newly synthesized chromatin. Hyperacetylation of histones
131 presumably occurs in the cytoplasm and may be mediated by B-type acetyltransferases like Hat1 (Li et
132 al., 2008, Masumoto et al., 2005, Tessarz and Kouzarides, 2014, Benson et al., 2006, Falbo and Shen, 2009,
133 Jackson et al., 1976, Lande-Diner et al., 2009, Ruiz-Carrillo et al., 1975, Annunziato and Hansen, 2000,
134 Sobel et al., 1995, Verreault et al., 1998).
135
136 Despite these insights, questions remain about how cell cycle progression influences histone modification
137 dynamics, especially in *in vivo* settings. For instance, to what extent are histone modifications regulated in
138 a cell cycle-dependent manner in developing tissues? How does the maintenance of these modifications
139 differ between rapidly proliferating cells and cells in quiescent, senescent, or post-mitotic states?
140 Moreover, how is the activity of histone-modifying enzymes coordinated with cell cycle checkpoints? To
141 begin to address these questions we used the developing *Drosophila* wing imaginal disc to characterize
142 cell cycle dependent histone modifications and reveal pronounced dynamics of H3K9 and H3K27
143 modifications in a developing tissue.
144
145 **RESULTS**
146
147 **(1) Post-translational modifications of H3K27 and H3K9 are linked to cell cycle dynamics**
148
149 To understand how cell cycle dynamics may affect chromatin dynamics, we aimed to identify post-
150 translational histone modifications that are sensitive to changes in cell cycle progression. Using the *rn-*
151 *GAL4* driver **(Fig S1.1A)**, under the control of a temperature-sensitive GAL80ts, we genetically manipulated
152 cell cycle progression in the pouch of developing wing imaginal discs for 24 hours by accelerating or
153 decelerating cell cycle dynamics. Within this timeframe of 24 h, we expect to disturb at least one cell cycle,
154 which lasts between 12 and 18 h in third instar wing imaginal discs (Neufeld et al., 1998, Milan et al., 1996,
155 Prober and Edgar, 2000, Crucianelli et al., 2022). First, we induced a cell cycle arrest in late G2 by
156 expressing *Cdk1-RNAi (Cosolo et al., 2019)*. Second, ectopic expression of the ERK-responsive ETS
157 transcription factor Pointed-P1 (PntP1) causes cells to arrest in either G1 or in G2 (Ito and Igaki, 2021). We
158 confirmed the arrest in our genotypes by observing the cell cycle reporter FUCCI and the absence of EdU
159 incorporation, a nucleotide analogue visualizing DNA replication, in nuclei of the *rn-GAL4* expression
160 domain **(Fig S1.1B-L)** (Zielke et al., 2014). Conversely, we accelerated the cell cycle by co-expressing of
161 dE2F1 and dDP (Buttitta et al., 2007, Neufeld et al., 1998). This did not alter the proportion of cells in G1 or

G2 but resulted in elevated EdU incorporation, reflecting the accelerated S-phase dynamics - both in frequency and speed (Crucianelli et al., 2022) - of this genotype **(Fig S1.1M-Q)**.

As post-translational histone modifications are numerous, we focused on prominent modifications mediated by well-known histone-modifying complexes. We analyzed modifications associated with gene regulation, such as H3K27ac (mediated by the p300/CBP nejire), H3K9ac (mediated by SAGA-HAT complex), H3K4me3 (mediated by the Trithorax (Trx)) and H3K27me3 (mediated by the Polycomb protein E(z)), or modifications associated with genome maintenance, such as H3K9me3 (mediated by Su(var)3-9), as well as examples of less well characterized modifications, such as H3K18ac and H4K8ac (mediated by p300/CBP, Gcn5, SAGA-HAT), H3K18 crotonylation (mediated by the p300/CBP nejire), and pan-H3K9 methylation or total lysine acetylation. We performed immunofluorescence staining for these modifications in wing imaginal discs with the induced cell cycle alterations described above.

Many of the histone modifications analyzed did not change upon manipulating cell cycle dynamics. For example, H3K18ac and H3K4me3 levels were not sensitive to cell cycle modulation **(Fig 1A-D, I-L, U-W, Fig S1.3A)**, and neither were H4K8ac, H3K9ac, H3K18 crotonylation, total H3K9 methylation nor levels of total lysine acetylation **(Fig S1.2, Fig S1.3B)**. Yet, strikingly, we found that H3K27ac levels were strongly reduced in cell cycle arrested genotypes, whereas levels of this modification were elevated when the cell cycle was accelerated **(Fig 1E-H, U-W)**. In contrast, H3K9me3 and H3K27me3 levels were elevated in arrested cells, whereas levels of both modifications were reduced when the cell cycle was accelerated **(Fig 1M-W)**. Importantly, alterations observed in cell cycle arrested cells were independent of which cell cycle phase the arrest occurred in. Specifically, H3K27ac reduction and H3K9me3 and H3K27me3 elevation was observed in both G1 and G2 arrested cell populations upon expression of *pntP1* **(Fig S1.1I, Fig 1G,O,S)**, suggesting that the elongation of either gap phase can produce the observed effects.

Taken together, we conclude that cell cycle dynamics have a surprising impact on histone modification in a proliferating tissue. First, only three tested modifications responded significantly to cell cycle dynamics in our assays, suggesting that only a subset of modifications is strongly linked to the cell cycle machinery. Second, these changes were not dependent to cells arresting in G1 or in G2, suggesting that overall cell cycle length is a defining factor rather than the gap phase position within a cell cycle. Third, if levels of histone modifications were primarily determined by the kinetics of restoring histone modifications after semi-conservative replication and the resulting histone PTM dilution, one may predict that modifications simply accumulate as the cell cycle lengthens. However, the reduction of H3K27ac in arrested cells defies a scenario in which continuous HAT activity restores H3K27ac levels after DNA replication. We thus wanted to better understand the relationship between histone methylation, histone acetylation and cell cycle dynamics.

(2) Cell cycle dependent changes in H3K27ac, H3K27me3 or H3K9me3 levels occur at preexisting target loci

To first identify the genomic regions affected by the cell-cycle-dependent changes in bulk levels of H3K27ac, H3K27me3, and H3K9me3, we performed CUT&Tag analysis on wing imaginal discs expressing *Cdk1-RNAi* under the control of *rn-GAL4* for 24 hours. Although *Cdk1-RNAi* is expressed in only a subset of cells within the wing disc (see **Fig S1.1A**) - limiting the magnitude of detectable differences - we consistently observed a decrease in H3K27ac levels, and an increase in levels of both H3K27me3 and H3K9me3 modifications. These changes occurred at genomic regions already carrying these modifications in wild type conditions, as evident from examples of genomic snapshots **(Fig 2 A,B)** and changes in average levels of modification on and around peaks identified in both wild type and *Cdk1-RNAi*-expressing discs **(Fig 2 C-F, Fig S2.1A, E)**. These findings are consistent with prior observations in mESCs, where H3K27me3 levels increase at pre-existing sites during prolonged G1 phases (Trouth et al., 2025).

Of note, many H3K27ac peaks identified only in wild type samples exhibited a significant reduction in H3K27ac levels in *Cdk1-RNAi*-expressing discs, suggesting that H3K27ac was indeed lost from pre-existing acetylated regions **(Fig S2.1B,E)**. In agreement with this conclusion, genomic sequences not identified as peaks by our algorithm in any sample showed little or no change in H3K27ac levels **(Fig S2.1D, E)**. In contrast, although increases in H3K27me3 and H3K9me3 levels in *Cdk1-RNAi* discs occurred at many pre-existing methylated sites **(Fig S2.1A, E)**, a substantial number of H3K27me3 and H3K9me3 peaks identified only in *Cdk1-RNAi* discs, as well as sequences in other genomic regions, also showed significantly elevated methylation compared to wild-type controls **(Fig S2.1C,D,E)**. This indicates that the accumulation of H3K27me3 and H3K9me3 in *Cdk1-RNAi* discs may extend beyond canonical methylation target sites identified in wild type discs. We conclude that cell-cycle-dependent changes to bulk levels of H3K27ac, H3K27me3 or H3K9me3 predominantly affect existing target sites; however, the increase in methylation may also affect other genomic regions. Importantly, the magnitude of changes compared to levels of methylation in control discs is similar for all genomic regions, suggesting that changes to H3K27me3 or H3K9me3 levels occur at the same rate across the genome.

Our conclusions are further supported by our observations that the histone-modifying enzymes responsible for H3K27 acetylation and H3K27methylation do not compete for the same histone residues *in vivo*. Specifically, when we performed a knock-down of the H3K27 methyltransferase E(z), we observed an expected loss of H3K27me3 **(Fig S2.2 A,B)**, but importantly, no corresponding increase in H3K27ac **(Fig S2.2 C,D)**. Conversely, when we performed a knock-down of the H3K27 acetyltransferase CBP/Nej (Nejire), we observed an expected loss of H3K27ac **(Fig S2.2 E,F)**, but no corresponding increase in H3K27me3 **(Fig S2.2 G,H)**. We conclude that, even though studies propose local antagonism of H3K27me3 and H3K27ac at the same residues (Tie et al., 2016, Philip et al., 2015, Tie et al., 2009), the cell-cycle-length-dependent decrease of H3K27ac and increase of H3K27me3 bulk levels upon expression of *Cdk1-*

RNAi are not driven by competition for the same H3K27 residues but instead reflect their natural occurrence of these distinct PTMs in distinct genomic contexts.

(3) H3K27 or H3K9 modifications are linked to cell cycle dynamics during development

If bulk histone modifications in wing discs are affected by cell cycle progression, can we provide evidence that this also occurs in a physiologically relevant state? During larval development, cells in the wing imaginal disc actively proliferate. However, the future wing margin forms a zone of non-proliferating cells (ZNC), where cells arrest in either G1 or G2 **(Fig S3.1 A-C)** (Johnston and Edgar, 1998). In addition to the ZNC, two clusters of G2-arrested cells with senescent markers can be found surrounding the wing pouch **(Fig S3.1 D)** (Zang et al., 2025). Strikingly, arrested cells in the ZNC **(Fig 3 A-C)** and senescent clusters **(Fig 3 D-F)** show a decrease in H3K27ac levels and an increase in H3K9me3 and H3K27me3, consistent with our previous conclusions upon cell cycle elongation by expression of *Cdk1-RNAi* or *UAS-pntP1*. Importantly, none of the other histone modifications recapitulated this pattern, again reinforcing the specific association between H3K9me3, H3K27me3 and H3K27ac levels and the dynamics of cell cycle progression **(Fig S3.1 E-H)**.

To begin to understand if there are consequences for cell-cycle-dependent PTM modulation during development, we analyzed, as an example of three PTMs, H3K27me3-dependent regulation of cell fates. H3K27me3 mediates Polycomb-dependent silencing of genes typically required for cell fate specification (Blackledge and Klose, 2021, Sparmann and van Lohuizen, 2006, Beuchle et al., 2001). In imaginal disc with either arrested (*Cdk1-RNAi*) or accelerated (*Dp,E2F1*) cell cycle dynamics, the expression of Polycomb targeted genes required for wing disc differentiation, such as Antp, Ubx/AbdA, En/inv, Nub, Wg, Ptc and Cut was not altered **(Fig S3.2)**. These observations demonstrate that reduced or elevated H3K27me3 levels observed upon changing cell cycle dynamics still ensure robust Polycomb target gene outputs, suggesting that a H3K27me3 levels buffer gene silencing against a range of cell cycle dynamics.

Surprisingly, our subsequent experiments revealed that the cell cycle-dependent regulation of H3K9me3, H3K27me3, and H3K27ac arises through mechanistically distinct pathways. Specifically, methylation and acetylation marks exhibit fundamentally different dynamics. Given these divergent mechanisms, we present our findings in two consecutive sections: first, we detail how H3K9me3 and H3K27me3 levels are coupled to the cell cycle via growth signaling pathways **(Fig. 4)**, followed by an independent analysis of the function of H3K27ac in preventing replication stress during S-phase **(Figs. 5 and 6)**.

(4) H3K27me3 or H3K9me3 are coupled to cell cycle dynamics via metabolic signaling

Previous studies suggest that H3K27me3 and H3K9me3 modifications after DNA-replication are reestablished after DNA replication through slow and continuous methyltransferase activity in subsequent

275 gap phases (Alabert et al., 2015, Zee et al., 2012, Reveron-Gomez et al., 2018). Our findings are consistent
276 with these observations: in all our imaginal disc models, levels of H3K9me3 and H3K27me3 increase in
277 conditions with elongated cell cycles (and thus infrequent S-phase events, reducing replication-
278 associated dilution of these marks), and decrease in conditions with shortened cell cycles (increasing the
279 frequency of S-phase and thereby enhancing dilution). These results suggest that H3K9 and H3K27
280 methylation is driven by a relatively constant rate of histone methyltransferase activity, which appears not
281 to be affected by genetic alterations of the cell cycle machinery. If the rate of histone methylation can
282 indeed be genetically separated from the frequency of cell cycling, what mechanisms then govern the
283 restoration of histone methylation to the appropriate levels, particularly for H3K9me3, which is essential
284 for heterochromatin architecture, and H3K27me3, which is critical for gene silencing? To address this
285 question, we decided to manipulate cell cycle progression upstream of direct regulators of the cell cycle
286 by activating a proliferative pathway with important metabolic functions. Specifically, we expressed a
287 constitutively active Insulin receptor (InR^{DA}) under the control of *rn-GAL4* for 24 h, which promotes PI3K/Akt
288 signaling. The resulting metabolic changes can be visualized by higher rates of protein synthesis reflecting
289 higher biosynthetic capacity, accelerated cell proliferation visualized by high EdU incorporation and
290 ultimately, larger wing pouch size **(Fig 4A-C, Fig S4 A-E)**. Of note, expression of InR^{DA} did not alter the FUCCI
291 cell cycle profile, demonstrating that the higher metabolic activity shortens the overall cell cycle length,
292 rather than affecting specific cell cycle phases **(Fig S4F,G)**.
293
294 Importantly, we found that expression of InR^{DA} alone did not give rise to changes in H3K27 or H3K9
295 methylation levels, despite the accelerated cell divisions **(Fig 4 D,E,H, I)**. This demonstrates that the
296 metabolic potential can tune the rate of H3K27 and H3K9 methylation, to keep levels of H3K27 or H3K9
297 methylation comparable to wild type levels, despite accelerated cell cycle progression. To now
298 functionally separate metabolic potential from cell cycle progression, we also arrested the cell cycle by
299 co-expressing the constitutively active Insulin receptor with a *Cdk1-RNAi*. As expected from our previous
300 experiments, levels of H3K27me3 and H3K9me3 increased, but most strikingly, levels of H3K27me3 and
301 H3K9me3 were even higher than in discs expressing *Cdk-1-RNAi* alone **(Fig 4F,G,J,K)**. These results
302 demonstrate that rates of H3K27 or H3K9 methylation are intimately linked to the metabolic potential of a
303 cell - with the purpose to match the rate of H3K27 or H3K9me3 methylation with the speed of cell cycle
304 progression and thus the frequency of S-phase linked histone dilution **(Fig 4 P,Q)**. Of note, levels of
305 H3K4me3 were not affected by these manipulations **(Fig 4 L-O)**, indicating that a modification maintaining
306 steady levels of bulk transcriptional activity is not - and even should not be - linked to metabolic rates or
307 the rate of cell cycle progression.
308
309 We wanted to better understand the functional implications of our findings. The link between levels of
310 H3K9me3 and cell cycle progression becomes relevant in physiological and pathological setting of
311 senescence, where cytotoxic stress or oncogenic mutations provide metabolic activation that is
312 juxtaposed to a senescent cell cycle arrest program. Accordingly, in senescent G2-arrested cells at the

313 center of inflammatory tissue damage in wing imaginal discs induced by ectopic expression of the TNFα
314 homologue eiger (egr) **(Fig S4.2 A-F)** (Cosolo et al., 2019, Floc'hlay et al., 2023, Jaiswal et al., 2023, Smith-
315 Bolton et al., 2009), we observed high levels of H3K9 methylation **(Fig S4.2G-I, purple)**. Importantly, levels
316 in senescent cells with inflammatory metabolism were higher than in quiescent cells at the disc periphery,
317 which exhibit low insulin-signaling activity **(Fig S4.2G-I, yellow)** (Maya et al., 2024). These observations
318 support our conclusions that high and low metabolic activity coupled to cell cycle arrest produce different
319 levels of H3K9me3. We thus propose that the widely reported senescence-associated
320 heterochromatinization associated with elevated H3K9me3 during oncogene-induced senescence may
321 not be a feature of the senescence program *per se* but rather a consequence of continuous H3K9
322 trimethylation driven by metabolic activation from oncogenic mutations in the absence of cell division
323 (Hernandez-Segura et al., 2018, Huang et al., 2022, Narita et al., 2003). Finally, in agreement with our
324 previous conclusions, we found that cells undergoing fast regenerative proliferation around the site of
325 inflammatory damage have lowest levels of H3K9me3 **(Fig S4.2G-I, cyan)**.
326
327 **(5) CBP/nejire-mediated H3K27 acetylation is high during S-phase**
328
329 Having revealed how H3K9me3 and H3K27me3 dynamics are coupled via metabolic cues to the cell cycle,
330 we now wanted to characterize the observed cell cycle dynamics of H3K27 acetylation. The
331 downregulation of H3K27ac by cell cycle elongation and the upregulation of H3K27ac by cell cycle
332 acceleration contradicts the simple explanation that an enzymatic activity acetylates H3K27 at a constant
333 rate. To better understand H3K27ac dynamics, we performed a detailed analysis of H3K27ac levels
334 throughout the cell cycle by correlating H3K27ac with FUCCI reporters in wing imaginal discs. We
335 specifically excluded mitotic cells from this analysis, as the highly condensed nature of their
336 chromosomes and the cells' extreme apical position prevented a direct comparison to other cell cycle
337 stages.
338
339 Using this approach, we found that H3K27ac levels were significantly increased in nuclei of early and late
340 S-phase cells if compared to G1 and G2 phases **(Fig 5A-C)**. This increase, and especially the much higher
341 levels in late S-phase in comparison to G2, could only partially be recapitulated by changes in total H3 or
342 total acetyl-Lysine levels **(Fig S5.1 A-F)**. Of note, fluctuation of H3 and total lysine acetylation in our
343 microscopy assays can be mostly explained by S-phase dependent histone synthesis and histone
344 acetylation, as well as fluctuating morphology of interphase nuclei (Stein et al., 1975, Mendiratta et al.,
345 2019, Verreault et al., 1998). Our finding that H3K27ac levels are higher throughout S-phase are consistent
346 with our earlier observations: cells which cycle fast repeatedly enter S-phase and cells which cycle slowly
347 are not often found in S-phase, hence bulk H3K27ac levels in a proliferating and arrested tissue will appear
348 high and low, respectively.
349

350 These results suggest that the enzymes responsible to regulate H3K27 acetylation may exhibit cell-cycle-
351 dependent regulation. Knock-down of the H3K27ac HAT CBP/nej via RNAi (*neijire-RNAi*) expressed for 24
352 h under the control *rn-GAL4*, completely abolished H3K27ac staining in the wing pouch, confirming that
353 CBP/nej is the main source of H3K27 acetylation in the wing disc **(Fig 5 D-E)** (Willnow and Teleman, 2024).
354 To provide specific proof that CBP/nej mediates S-phase-dependent H3K27 acetylation, we overexpressed
355 CBP/nej for 24 h under the control of *rn-GAL4* and correlated H3K27ac levels with cell-cycle phases using
356 the FUCCI reporter. While global H3K27ac increased upon CBP/nej overexpression **(Fig 5F,G,J; Fig S5.1**
357 **G,H)**, we observed a disproportionate increase of H3K27ac in late S-phase cells **(Fig 5J')**. This
358 demonstrates that CBP/nej-driven acetylation of H3K27 is especially pronounced during S-phase and
359 indicates that H3K27ac accumulates ectopically in late S-phase cells when CBP/nej levels are too high. In
360 support of a model where CBP/nej is specifically active during S-phase, we found that levels of two other
361 CBP/nej-mediated modification (H3K18ac and H4K8ac) showed a less pronounced but still detectable
362 increase in S-phase cells of normally proliferating wild type tissue **(Fig S5.2 A-F)**, which is consistent with
363 the reduced CBP/nej substrate specificity for these two residues, as well as for H3K18 crotonylation,
364 observed in CBP/nej-RNAi experiments **(Fig S5.2 G-N)**.
365
366 As these targeted overexpression experiments suggested that CBP/nej levels may influence S-phase-
367 dependent activity, we examined a CBP/nej-GFP fusion protein expressed from the endogenous locus to
368 assess if CBP levels fluctuate during the cell cycle (Marsh et al., 2025). We found that, in proliferating wing
369 discs, nuclear GFP levels were mostly uniform in all cells **(Fig S5.2 O)**, indicating that regulation of CBP/nej
370 enzymatic activity, rather than cell cycle dependent changes in protein levels, underlies the S-phase-
371 specific activity. Indeed, in cultured cells, CBP/p300 activity may be regulated by cyclin-dependent
372 kinases at the G1/S transition (Ait-Si-Ali et al., 1998).
373
374 The pronounced reduction of H3K27ac in late-S-phase, and subsequently in G2-phase or G1-phase cells,
375 which we observed in development, in arrested cell populations and upon CBP/nej overexpression or
376 knock-down, demonstrates that the removal of H3K27ac in late S-phase must be a highly controlled
377 process. Removal of acetylation from the H3K27 residue would likely be mediated by HDAC activity. We
378 thus depleted the primary H3K27 deacetylase HDAC1 (Rpd3) via expression of an RNAi construct under
379 the control of *rn-GAL4* for 24 h (Willnow and Teleman, 2024). HDAC1 knockdown led to a mild but
380 detectable overall increase in H3K27ac, consistent with its role in H3K27ac removal **(Fig 5 H, I, K; Fig S5.1**
381 **I,J)**. Yet, importantly, we observed a disproportionate increase of H3K27ac in late S-phase cells, supporting
382 a model where HDAC1 is required to specifically remove H3K27ac in late S-phase **(Fig 5K')**.
383
384 **(6) CBP/nej activity and H3K27acetylation is required to prevent replication stress during S-phase**
385
386 We finally wanted to understand what function elevated CBP/nej activity during S-phase may serve. To
387 analyze if elevated CBP/nej activity may reflect a specific requirement during DNA replication, we

388 conducted a knock-down of *CBP/nej* in the wing pouch under the control of *rn-GAL4* for 24 h. We first
389 analyzed DNA replication by EdU incorporation and found a wide-spread decrease in the number of cells
390 entering S-phase and in DNA replication activity, suggesting that both S-phase entry and progression was
391 severely slowed within 24 h of *CBP/nej* knock-down **(Fig 6A-C)**. To determine if DNA replication during
392 *CBP/nej* knock-down had proceeded successfully, we investigated if *CBP/nej-RNAi*-expressing cell
393 experienced replication stress. We thus analyzed levels of phosphorylated γH2A, a marker of DNA double
394 strand breaks which can arise at stalled replication forks (Madigan et al., 2002, Petermann et al., 2010). In
395 all wild type tissues, we observed a similar number of high intensity nuclei positive for γH2A, likely
396 representing physiological cell death or (unspecific) binding of the antibody in mitotically active cells
397 (Khan et al., 2017). However, the majority of nuclei are negative for γH2A **(Fig 6D,F)**. Strikingly, in all nuclei
398 of *CBP/nej-RNAi* -expressing cells, we observed a pronounced increase in nuclear γH2A levels - which were
399 represented by medium fluorescence intensities. The γH2A signal covered the entire nuclei, suggesting
400 wide-spread DNA damage **(Fig 6E,G,H)**. We conclude that CBP/nej is specifically required to prevent
401 genome-wide replication stress during S-phase. Accordingly, *CBP/nej-RNAi*-expressing cells cannot
402 progress through the cell cycle and completely arrest in G2 **(Fig 6I,J)**. In tissue damage models of wing
403 discs, cells arrest in G2 as a consequence of stress-dependent activation of JNK-signaling, which
404 downregulates *cdc2/stg* (Cosolo et al., 2019). Yet, co-expressing a dominant-negative JNKK (bskDN) in
405 *CBP/nej-RNAi*-expressing caused pronounced downregulation of JNK activation **(Fig S6A-C)**, but still
406 resulted in G2 arrested cells **(Fig S6D)**. This strongly indicates that a very specific function of CBP/nej in
407 DNA replication caused a G2 cell cycle arrest by activation of a DNA damage checkpoint, rather than the
408 non-specific activation of cellular stress signaling through JNK. These observations are thus consistent
409 with a model were high levels of CBP/nej-mediated H3K27ac are specifically required to ensure faithful
410 DNA replication and to prevent DNA damage and consequently, a DNA damage induced cell cycle arrest
411 in G2. Of note, analysis of *CBP/nej*-overexpressing tissues revealed normal patterns of EdU incorporation
412 and distribution, suggesting that cells with high - but still cell-cycle-dependent - levels of H3K27ac
413 proliferate normally **(Fig S6E-G)**.
414
415 CBP/nej targets a wide range of substrates, including several non-histone proteins (Stauffer et al., 2007,
416 Cazzalini et al., 2014, Dutto et al., 2018, Tillhon et al., 2012, Ramadan et al., 2025, Ogiwara et al., 2011).
417 We thus wanted to determine, if the function of CBP/nej in preventing replication stress is mediated by its
418 substrate H3K27. Especially, since H3K27 was the histone substrate most sensitive to the loss of CBP/nej
419 activity in our assays **(**refer to **Fig S5.2 G-N)**. To test this, we generated mosaic clones homozygous for a
420 deletion of the entire histone gene cluster (ΔHisC), whose viability was rescued by 12 copies of a histone
421 gene unit in which wild type H3 was replaced with a non-modifiable H3K27R amino acid substitution
422 (Pengelly et al., 2013). As previously reported, these clones lose Polycomb gene silencing function
423 normally mediated by H3K27me3, and exhibit derepression of Hox genes such as *AbdB* **(Fig S6H,I)**
424 (Pengelly et al., 2013). When we assessed if these cells also exhibit replication stress, we observed broad
425 and elevated levels of γH2A in the H3K27R-substituted clones **(Fig 6K)**. These findings suggest that the

426 function of CBP/nej in mitigating replication stress during DNA replication may be, at least in part,
427 mediated through its modification of H3K27 **(Fig 6I)**.
428
429 **DISCUSSION**
430
431 Our work dissects the link between H3K27ac, H3K27me3, and H3K9me3 modification dynamics and
432 dynamics of the cell cycle in proliferating tissues *in vivo*. We demonstrate that both physiological and
433 genetically induced elongation of the cell cycle leads to elevated bulk levels of H3K27me3 and H3K9me3.
434 Conversely, accelerated cell cycle progression specifically decreases these histone marks. Genome-wide
435 analyses using CUT&tag assays revealed that these changes occur predominantly at their distinct pre-
436 existing genomic target loci, implicating canonical histone readers and modifiers in mediating these cell
437 cycle-dependent changes. Importantly, despite cell cycle-dependent changes in bulk H3K27me3 levels,
438 expression patterns of Polycomb target genes remained unaffected, implying that H3K27me3-dependent
439 gene silencing at target loci is buffered even under altered cell cycle conditions. Mechanistically, we found
440 a tight coupling between histone methylation rates and cell division frequency, mediated by cellular
441 metabolic activity. Specifically, H3K27me3 and H3K9me3 levels remained normal upon expression of a
442 constitutively active Insulin receptor, suggesting that cells channeled the higher metabolic activity into
443 accelerated cell divisions and maintained H3K27me3 and H3K9me3 levels proportional to cell division
444 rates. Remarkably, active Insulin receptor-expressing cells forced to arrest their cell cycle accumulated
445 levels of H3K27me3 and H3K9me3 to much higher levels than arrested wild type cells, demonstrating that
446 metabolic rate tunes the rate of histone methylation to match the frequency of S-phase occurrence, i.e.
447 the frequency of cell divisions. These observations have important implications for chromatin
448 dysregulation in pathological conditions, such as cancer, where the tight coordination between metabolic
449 and cell cycle rates becomes compromised. An important implication of our findings relates to the
450 emergence senescence-associated heterochromatin, a phenomenon well-documented during oncogene-
451 induced senescence (Hernandez-Segura et al., 2018, Huang et al., 2022, Narita et al., 2003). Our data
452 suggest that H3K9me3 accumulation in senescence-associated heterochromatin may reflect persistent
453 methyltransferase activity driven by aberrant metabolic stimuli in the absence of replication-dependent
454 dilution. Thus, the observed chromatin state in senescent cells may be a consequence of the mismatch
455 between metabolic and cycling rate, rather than an intrinsic feature of the senescence phenotype itself.
456 An important implication of our findings is that post-mitotic and differentiating cells, such as neurons,
457 must tightly regulate histone-modifying activities to prevent the aberrant accumulation of repressive
458 marks, such as H3K9me3 and H3K27me3.
459
460 Furthermore, we observed that H3K27ac exhibits a unique, cell cycle–dependent profile, peaking
461 significantly during S-phase. While hyperacetylation of newly synthesized histones at various residues
462 during S-phase is well-established, an S-phase dependent increase in nuclear acetylation of H3K27 has
463 not been reported (Li et al., 2008, Masumoto et al., 2005, Tessarz and Kouzarides, 2014, Benson et al.,

464 2006, Falbo and Shen, 2009, Jackson et al., 1976, Lande-Diner et al., 2009, Ruiz-Carrillo et al., 1975,
465 Annunziato and Hansen, 2000, Sobel et al., 1995). We propose this peak in acetylation during S-phase is
466 mediated by CBP/nej, potentially regulated by cyclin-dependent kinases at the G1/S transition (Ait-Si-Ali
467 et al., 1998). Correspondingly, our data is consistent with the idea that H3K27 becomes deacetylated
468 during late S-phase by HDAC1. Generally, HDAC activity is reported to remove hyperacetylation on newly
469 synthesized histone at the end of S-phase to reestablish higher order chromatin organization (Annunziato
470 and Seale, 1983). However, whether the H3K27 acetylation cycle mediated by CBP and HDAC 1 occurs on
471 old histones, newly synthesized histones, or on newly incorporated histones cannot be resolved with our
472 methods. Yet, the observed H3K27 acetylation cycle reveals novel cell cycle dependent targets of CBP/nej
473 and HDAC1.
474
475 Functionally, we demonstrate that CBP/nej activity is essential during S-phase to prevent DNA damage
476 from replication stress and consequently delays in cell cycle progression mediated by a replication
477 checkpoint. In fact, previous studies find that CBP/nej and ATR mei-41 are required for the replication
478 checkpoint itself to function properly (Smolik and Jones, 2007, Stauffer et al., 2007). This may be explained
479 by acetylation non-histone substrates by CBP/p300, which stabilizes key DNA damage repair factors,
480 including PCNA, ATR and ATM, thereby facilitating DNA repair following damage (Stauffer et al., 2007,
481 Cazzalini et al., 2014, Dutto et al., 2018, Tillhon et al., 2012, Ramadan et al., 2025, Ogiwara et al., 2011).
482 Consistent with this, mutations in EP300 result in persistent replication stress, replication fork collapse,
483 genomic instability, and embryonic proliferation defects (Barreto-Galvez et al., 2023; Yao et al., 1998).
484 (Barreto-Galvez et al., 2023, Yao et al., 1998). Collectively, these findings underscore the essential role of
485 CBP/p300-mediated acetylation in regulating replication integrity and genomic stability beyond traditional
486 cell cycle regulation. Importantly, our findings extend this previous work by providing mechanistic insight,
487 indicating that *in vivo* this function is mediated by acetylation of H3K27, a target commonly regulated by
488 CBP/nej and HDAC1. Notably, cells carrying the H3K27R mutation exhibit derepression of Hox genes,
489 closely resembling the phenotype associated with loss-of-function mutations in PRC1 and PRC2
490 complexes(Pengelly et al., 2013, Classen et al., 2009, Beuchle et al., 2001). However, H3K27R cells also
491 display a pronounced, albeit not complete, reduction in overall H3K27ac levels – in contrast to the nearly
492 complete loss of H3K27ac observed after 24 h of CBP/nej RNAi-expression. This suggests that CBP/nej-
493 mediated acetylation of K27 may occur on both H3 and H3.3 variants, with the anti-H3K27ac antibody likely
494 recognizing both forms and the broad substrate specificity of CBP/nej likely targeting both histone variants.
495 Importantly, acetylation of H3 and H3.3 at K27 may carry distinct functional implications. H3.3 variants
496 appear to be particularly critical for enhancer-associated H3K27ac thereby serving roles in interphase
497 cells (Trovato et al., 2020), whereas acetylation of canonical H3 may regulate chromatin function and DNA
498 replication in S-phase. Indeed, associations of H3K27ac with Origin Recognition Complex-binding sites
499 and its requirement for gene amplification during endoreplication (Aggarwal and Calvi, 2004, Eaton et al.,
500 2011, Hua and Orr-Weaver, 2017, McConnell et al., 2012), suggests that elevated levels of H3K27ac may
501 be essential to establish an open chromatin environment necessary for efficient DNA replication.

Collectively, these findings position H3K27ac as a central regulator integrating chromatin structure, DNA replication and genome integrity.

In conclusion, our findings establish a robust mechanistic link between cell cycle dynamics, metabolic signaling and histone modification of H3K27 and H3K9, and specifically implicate H3K27ac as critical mediator of replication fidelity and chromatin organization. These insights highlight the necessity of maintaining balanced histone modification levels to preserve genomic stability, particularly under varying proliferative and metabolic states, with broad implications for developmental biology, aging, and cancer biology.

512 **EXPERIMENTAL PROCEDURES**

513

514 ***Drosophila* genetics**

515 All experiments were performed on *Drosophila melanogaster*. Fly strains (see Table S1) were maintained
516 on standard fly food (10L water, 74,5g agar, 243g dry yeast, 580g corn flour, 552ml molasses, 20.7g
517 Nipagin, 35ml propionic acid) at 18°C – 22°C. Larvae from experimental crosses were allowed to be fed on
518 Bloomington formulation (175.7g Nutry-Fly,1100ml water 20g dry yeast, 1.45g Nipagin in 15ml Ethanol,
519 4.8ml Propionic acid) and raised at 18°C or 30°C to control GAL80ts-dependent induction of GAL4/UAS. To
520 drive expression of UAS-constructs, such as *UAS-Cdk1-RNAi*, under the control of *rn-GAL4* in the wing
521 pouch, experiments were conducted following protocols from Smith-Bolton et al. (2009), La Fortezza et al.
522 (2016), and Cosolo et al. (2019), with slight modifications. Briefly, larvae with the genotype *rn-GAL4, tub-*
523 *GAL80^{ts}* and appropriate UAS-transgenes were staged by a 6 hours egg collection and raised at 18°C with
524 a density of 50 larvae per vial. Transgene expression was activated by shifting the temperature to 30°C for
525 24 hours on day 7 after egg deposition (AED). Unless otherwise noted, dissections were performed
526 immediately after this induction period (recovery time point R0). Control genotypes were derived from
527 either rn^{ts} control crosses or sibling animals (+/TM6c). All experiments were performed with at least ≥ 2
528 independent experimental replicates. Our experimental design did not consider differences between
529 sexes unless for genetic crossing schemes.

530

531 **FLP/FRT-Mediated Clone Induction**

532 Mitotic recombination to generate mosaic clones of the *Drosophila* histone gene cluster (ΔHisC) was
533 induced using the FLP/FRT system. Adult flies were allowed to lay eggs for 72 hours at 25 °C. FLP
534 recombinase expression was triggered by a 1-hour heat shock at 37 °C. Larvae were dissected either 48 or
535 72 hours after heat shock for subsequent analysis. Transgene cassettes providing a total of 12 copies of
536 the Histone gene unit with a H3K27R point mutation (12×His-GUH3-K27R) rescues cell viability of (ΔHisC)
537 mutant clones (see (Pengelly et al., 2013)).

538

539 **Immunohistochemistry of wing imaginal discs**

540 To visualize histone modifications, wing discs from third instar larvae were dissected and fixed for 10
541 minutes at room temperature in 4% paraformaldehyde in PBS. Washes were performed in PBS containing
542 0.1% TritonX-100 (PBT). The discs were then incubated with primary antibodies (**Table S1**) in 0.1% PBT,
543 gently mixing 2-overnights at 4°C. During incubation with cross-absorbed secondary antibodies coupled
544 to Alexa Fluorophores (Table S1) at 4°C for 1-overnight, tissues were counterstained with DAPI (0.25 ng/µL,
545 Sigma, D9542). Tissues were mounted using SlowFade Gold Antifade (Invitrogen, S36936). To visualize
546 DNA damage using the anti-H2AvD phosphoS137 antibody, wing discs were fixed 5 minutes at room
547 temperature in 4% paraformaldehyde in PBS. Washes were performed in PBS containing 0.5% TritonX-100.
548 The primary antibody was incubated in 0.5% PBT overnight at 4°C and the secondary antibody in 0.5% PBT
549 for 2 hours at room temperature. For all other staining protocols, discs were fixed for 15 minutes at room

550 temperature in 4% paraformaldehyde in PBS. All washes and incubations were performed in PBS
551 containing 0.1% TritonX-100 as described above.To maintain consistency in staining across genotypes,
552 control and experimental wing discs were processed together in the same vial throughout the protocol and
553 mounted on the same slide whenever possible. Images were acquired using the Leica TCS SP8
554 Microscope, using the same confocal settings for linked samples and processed using tools in Fiji. Figure
555 panels were assembled in Affinity Designer 2.
556
557 **EdU labelling**
558 EdU incorporation was performed using the Click-iT Plus EdU Alexa Fluor 647 Imaging Kit (Table S1). Briefly,
559 larval cuticles were inverted in Schneider's medium and incubated with EdU (10μM final concentration) at
560 RT for 15 minutes. Cuticles were then fixed in 4% PFA/PBS for 15 minutes, washed for 30 minutes in PBT
561 0.5%. EdU-Click-iT labeling was performed according to manufacturer's guidelines. Tissues were washed
562 in PBT 0.1%, after which immunohistochemistry, sample processing and imaging were carried out as
563 described above.
564
565 **SA-β-Gal staining**
566 CellEvent senescence detection kit from Invitrogen (Table S1) was used to check senescence-associated
567 β-galactosidase activity, following the manufacturer instructions. Briefly, larvae were dissected in PBS,
568 fixed with 4% PFA, washed with 1% BSA (in PBS), and then incubated in working solution for 2h at 37°C.
569 Washing steps were performed in PBS and PBS containing 0.1% TritonX-100 (PBT). Tissues were
570 counterstained with DAPI (0.25 ng/μl). Further immunohistochemistry analysis and sample mounting was
571 performed as described above.
572
573 **Protein synthesis assay using OPP- Click-iT staining**
574 OPP Assays were performed using Click-iT® Plus OPP Protein Synthesis Assay Kits (Invitrogen Molecular
575 Probe) according to manufacturer's instructions. Briefly, larvae were dissected and inverted cuticles were
576 incubated with a 1:1000 dilution of Component A in Schneider's medium for 15 minutes on a nutator.
577 Larval cuticles were fixed with 4% paraformaldehyde for 15 minutes, rinsed twice in 0.1% PBT, and
578 permeabilized with 0.5% PBT for 15 minutes. The cuticles were then stained with the Click-iT® cocktail for
579 30 minutes at room temperature, protected from light. Further immunohistochemistry analysis and
580 sample mounting was performed as described above.
581
582 **CUT&Tag sample preparation**
583 Briefly, for each genotype around 80-100 wing discs were dissected in ice cold Schneider's medium,
584 collected, snap frozen and stored at -80°C until further use. Nuclei were isolated with the help of a
585 mechanical pestle and processed for CUT&Tag analysis as previously described (Zenk et al., 2023,
586 Cardamone et al., 2025). For normalizing the levels of histone H3 modifications and as a proxy of the
587 starting material in each condition, we also generated samples for total histone H3. Libraries were

prepared by supplementing the NEBNext HighFidelity 2× PCR Master Mix with 1 pg of Tn5-tagmented lambda DNA (New England Biolabs, #N3011S) as a spike-in normalizer. The library indexing was performed using Illumina i5 and i7 (Buenrostro et al., 2015) through 15 cycles (1 x 5 min at 72 °C, 1 x 30 sec at 98°C, 13 x 10 s at 98 °C, 30 sec at 63 °C, 1 x 1 min at 72 °C, hold at 4 °C). The libraries were purified using Nucleomag NGS Clean-up and Size Select beads (Macherey-Nagel, #744970.50). Quality checks were done with Qbit DNA HS Assay (ThermoScientific, #Q32854) and Bioanalyzer (Agilent). Finally, two independent library replicates were sent for next generation sequencing.

QUANTIFICATIONS, BIOINFORMATIC ANALYSIS AND STATISTICS

General comments

For all quantifications of imaging data, control and experimental samples were processed together and imaged in parallel, using the same confocal settings. Images were processed, analyzed and quantified using tools in Fiji (ImageJ 2.9.0) (Schindelin et al., 2012). Extreme care was taken to apply consistent methods (i.e., number of projected sections, thresholding methods, processing) for image analysis. Figure panels were assembled using Affinity Designer 2.6.2. Statistical analyses were performed in Graphpad Prism. Illustrations were created in Biorender.

Quantification of histone modifications

For quantification of levels of histone modifications, an xy-representation containing the maximum number of pouch and hinge cells was generated using a sum projection of the relevant channel. Three square regions of interest (ROIs) measuring 15 × 15 µm were placed in distinct areas of either the pouch or the hinge, carefully excluding regions with developmentally arrested cells. The mean intensity of the modification signal was measured within each ROI. For each disc, the average pouch signal was normalized to the average hinge signal and reported as a pouch-to-hinge intensity ratio.

Quantification of EdU incorporation

Figure S1.1: To first create a nuclear mask, an xy- representation containing the maximum number of pouch nuclei was generated using a sum projection of the DAPI channel. The background signal was reduced using the “Subtract Background” function with a rolling ball radius of 100 pixels. Local contrast was enhanced with the “Enhance Local Contrast (CLAHE)” function, using a block size of 127, 256 histogram bins, and a maximum slope of 3. Automatic thresholding was performed using the “Moments” method with the “dark” option selected, and the image was then converted into a binary mask of DAPI-positive nuclear areas. A nuclear ROI was generated from this mask using the selection tool. The pouch region was manually selected based on wing fold morphology. To isolate the nuclei within the pouch, a binary “AND” operation was used to combine nuclear mask and pouch selection. This final pouch-specific DAPI mask was used to measure EdU signal intensity.

Figure 6: To create an EdU mask, an xy- representation containing the maximum number of pouch nuclei was generated using a sum projection of the EdU channel. A "Gaussian blur" ($\sigma = 2$) was applied to reduce noise and smooth the signal. Automatic thresholding was then performed using the "Moments" method with the "dark" option selected. The image was converted into a binary EdU mask with a black background. A ROI was generated from this mask using the selection tool to define EdU-positive pixels. Separately, the pouch region was manually selected based on wing fold morphology. To isolate EdU-positive pixels specifically within the pouch, a binary "AND" operation was applied to combine the EdU selection with the pouch selection. This final pouch-specific EdU mask was used to measure EdU signal intensity.

To assess changes in the number of proliferating cells, pouch-specific DAPI and EdU masks were generated as described above. A binary "AND" operation was used to extract EdU-positive nuclei located within DAPI-positive regions in the pouch. The area of EdU-positive nuclei was then divided by the total area of EdU and DAPI-positive regions within the pouch to calculate the fraction of proliferating cells. This EdU-to-DAPI area ratio was calculated per disc and used for comparative analysis.

Quantification of OPP levels in wing imaginal discs

An xy-representation containing the maximum number of pouch cells was generated using a sum projection of the relevant channels. In both control and constitutively active insulin receptor-expressing discs, the pouch region was manually selected based on wing fold morphology. Mean OPP intensity was then measured within the defined pouch region for each disc.

Quantification of pouch size

For both control and constitutively active insulin receptor-expressing discs, a slice containing the maximum number of pouch cells was selected. In each case, the pouch region was manually defined based on wing fold morphology. The area size of the selected pouch region was then measured for each disc.

Cell cycle phase classification using FUCCI and quantifications of H3, Total Acetyl Lysine, H3K27ac, H3K18ac and H4K8ac level

To classify nuclei in the wing pouch according to cell cycle phase and to quantitatively correlate levels of H3 and acetylation levels with each phase, a custom image analysis workflow was implemented in ImageJ/Fiji. A single z-slice containing the highest number of pouch cells was selected from each control disc. The image stack was split into individual channels (e.g., DAPI, GFP-E2f1$^{1-230}$, mRFP-NLS-CycB$^{1-266}$, H3K27ac). To generate a nuclear mask, the DAPI, GFP, RFP, and other nuclear markers were averaged sequentially using the Image Calculator. The resulting image was thresholded using the Otsu method (upper limit set to 255) and converted into a binary mask defining nuclear pixels. A nuclear pixel selection was generated from the binary image and added to the ROI Manager. The pouch region was manually defined based on wing fold morphology. A binary "AND" operation was used to restrict the nuclear pixel mask to the pouch, producing a final pouch-specific nuclear mask. This mask was overlaid on the GFP,

RFP, and other nuclear marker channels, and the X/Y coordinates of each ROI were used to extract signal intensities for each nuclear pixel. Threshold values for GFP and RFP determined based on average intensity of 5 nuclei in early S-phase. Each nuclear pixel was classified into a cell cycle phase using these thresholds, following FUCCI-based criteria: G2 phase: GFP > threshold, RFP > threshold; G1 phase: GFP > threshold, RFP ≤ threshold; Early/mid S phase: GFP ≤ threshold, RFP ≤ threshold; Late S phase: GFP ≤ threshold, RFP > threshold. For each nuclear pixel, the intensity of the corresponding nuclear markers (e.g., H3, acetyl-lysine, H3K27ac) was recorded. To account for inter-sample variability, intensity values within each cell cycle phase were normalized by dividing them by the total nuclear marker signal summed across all phases (G1, early S, late S, and G2) within the same disc. This normalization provided the relative contribution of each cell cycle phase to the total signal, allowing for direct comparisons across samples.

γH2Av intensity quantifications

To create a nuclear mask, an xy- representation containing the maximum number of pouch nuclei was generated using a sum projection of the DAPI channel. The background signal was reduced using the "Subtract Background" function with a rolling ball radius of 100 pixels. Local contrast was enhanced with the "Enhance Local Contrast (CLAHE)" function, using a block size of 127, 256 histogram bins, and a maximum slope of 3. Automatic thresholding was performed using the "Moments" method with the "dark" option selected, and the image was then converted into a binary mask. A nuclear ROI was generated from this mask using the selection tool. The pouch region was manually selected based on wing fold morphology. To isolate the nuclear pixels within the pouch, a binary "AND" operation was used to combine nuclear mask and pouch selection. This final mask was used to measure γH2Av and DAPI intensities for each disc. γH2Av intensities were normalized to the corresponding DAPI intensity.

CUT&Tag Bioinformatic Analysis

The CUT&Tag data processing was performed as described before with some modifications (Atinbayeva et al., 2024, Ibarra-Morales et al., 2021, Cardamone et al., 2025). As our quantitative CUT&Tag sequencing libraries contained DNA from *D. melanogaster* and spike-in of *lambda* phage genome (Genbank: J02459.1), we mapped the raw paired-end reads to a constructed hybrid dm6 and *Lambda* phage genome using *snakePipes-v3.0.0 DNA-mapping* (Bhardwaj et al., 2019) with updated Bowtie2 mapping parameters, as well as adapter trimming and MAPQ ≥ 1 filtering (*DNAmapping --mapq 1 --trim --fastqc --properPairs --dedup --cutntag --DAG --alignerOpts='--local --very-sensitive-local --no-discordant --no-mixed -I 10 -X 700'*). To assess reproducibility of both replicates, we utilised the *multiBamSummary* and *plotCorrelation* from *deepTools-v.2.5.7* to compute the Spearman correlation between the two replicates. Aligned replicates were merged before normalization to both H3 and spike-in signals. The code used for the H3 and *Lambda* normalization analysis was based on work done by Yinxiu Zhan (https://github.com/zhanyinx/atinbayeva_paper_2023) for (Atinbayeva et al., 2024). CUT&Tag peaks were called using *snakePipes-v3.0.0 ChIPseq* with *MACS2-v 2.2.9.1* (*ChIPseq -d Output_spikein hybrid.yaml H3_spikein_config.yaml --peakCaller MACS2 --cutntag --peakCallerOptions "--broad --qvalue 0.5 -f*

701 *BAMPE" --DAG*). Normalized bigWig and bam files were generated with *deepTools-v3.5.6* and used to
702 compute matrices of signal enrichment +/− 5kb around transcription start sites (TSS) or peak centers of
703 shared or unique peaks for *wt* and *Cdk1KD*. Coverage heatmaps and profiles were created using
704 *plotHeatmap* or *plotProfile* from *deepTools-v.2.5.7*.
705 For the quantification, the number of PE reads were counted in each shared or unique peak for *wt* and
706 *Cdk1KD* (*multiBamSummary BED-file --bamfiles <input files> --extendReads --outRawCounts <file>*) as
707 well as in 500 bp bins across the dm6 genome (*multiBamSummary bins --bamfiles <input files> --binSize*
708 *500 --extendReads --outRawCounts <file>*). The *DESeq2-v1.38.3* analysis was performed using the
709 previously computed H3 and spike-in scaling factors from merged data for size factor. Bins and peaks with
710 basemean (average read count across samples) of less than or equal to 25 read counts were discarded.
711 The design matrix was setup to compare the samples by condition and correct for replicate effects
712 (*design = ~replicate + condition*). Finally, we executed the *DESeq2* shrinkage of log2 fold changes
713 (*type = 'normal'*).
714
715 **CODE AND DATA AVAILABILITY**
716
717 All data, workflows and FIJI based algorithms necessary to interpret the imaging data are included within
718 the manuscript. Original imaging data and any additional information required to reanalyze the data
719 reported in this paper will be shared by AKC upon request. The code used for the mapping, normalization,
720 peak calling and signal quantification is available on Github:
721 https://github.com/LaraH9/nogay_et_al_2025. The CUT&Tag sequencing data generated in this study is
722 provided on NCBI SRA: https://www.ncbi.nlm.nih.gov/sra/PRJNA1300380.
723
724 **AUTHOR CONTRIBUTIONS**
725
726 Conceptualization LN, AKC; Data curation LN, LH, AKC; Formal analysis LN, LH, AKC; Funding acquisition
727 AKC; Investigation LN, AVM; Methodology LN, AVM, LH, FC, IG, AS, AF, LE, AKC; Project administration IG,
728 AKC; Supervision NI, AKC; Validation LN, AVM, FC, IG; Visualization LN, LH, AKC; Writing – original draft
729 LN, AKC; Writing – review & editing LN, AVM, LH, AKC
730
731 **ACKNOWLEDGEMENTS**
732
733 We thank the staff of the Life Imaging Center (LIC) in the Hilde Mangold House (HMH) of the Albert-
734 Ludwigs-University of Freiburg for help with their confocal microscopy resources, and
735 the excellent support in image recording. We specifically thank the DFG for supporting our imaging work
736 through project number 414136422. We thank the Bioinformatics and Sequencing facilities at the MPI-IE
737 for supporting this work. We thank Galina Erikson for supporting our bioinformatic analysis. We thank
738 Laura Bauttita, Melissa Harrison, Iswar Hariharan, Dirk Bohmann and Jürg Müller for sharing reagents and

the Bloomington *Drosophila* Stock Center (BDSC), the Vienna *Drosophila* Stock Collection (VDRC), the University of Zurich ORFeome Project (FlyORF) and the Developmental Studies Hybridoma Bank (DSHB) for providing fly stocks and antibodies. We thank the IMPRS-EBM and SGBM graduate schools for supporting our doctoral researchers.

FUNDING

Funding for this work was provided by the Deutsche Forschungsgemeinschaft (DFG, German Research Foundation) under Germany ś Excellence Strategy (CIBSS – EXC-2189), the DFG Heisenberg Program to AKC (668189), as well as DFG grants to AKC (667603) and the Boehringer Ingelheim Foundation (BIF Plus3 & Rise Up) to AKC. The funders had no role in study design, data collection and analysis, decision to publish, or preparation of the manuscript.

DECLARATION OF INTEREST

The authors declare no competing interests.

REFERENCES

AAGAARD, L., LAIBLE, G., SELENKO, P., SCHMID, M., DORN, R., SCHOTTA, G., KUHFITTIG, S., WOLF, A., LEBERSORGER, A., SINGH, P. B., REUTER, G. & JENUWEIN, T. 1999. Functional mammalian homologues of the Drosophila PEV-modifier Su(var)3-9 encode centromere-associated proteins which complex with the heterochromatin component M31. *EMBO J,* 18**,** 1923-38.

AGGARWAL, B. D. & CALVI, B. R. 2004. Chromatin regulates origin activity in Drosophila follicle cells. *Nature,* 430**,** 372-6.

AIT-SI-ALI, S., RAMIREZ, S., BARRE, F. X., DKHISSI, F., MAGNAGHI-JAULIN, L., GIRAULT, J. A., ROBIN, P., KNIBIEHLER, M., PRITCHARD, L. L., DUCOMMUN, B., TROUCHE, D. & HAREL-BELLAN, A. 1998. Histone acetyltransferase activity of CBP is controlled by cycle-dependent kinases and oncoprotein E1A. *Nature,* 396**,** 184-6.

ALABERT, C., BARTH, T. K., REVERON-GOMEZ, N., SIDOLI, S., SCHMIDT, A., JENSEN, O. N., IMHOF, A. & GROTH, A. 2015. Two distinct modes for propagation of histone PTMs across the cell cycle. *Genes Dev,* 29**,** 585-90.

ALABERT, C. & GROTH, A. 2012. Chromatin replication and epigenome maintenance. *Nat Rev Mol Cell Biol,* 13**,** 153-67.

ANNUNZIATO, A. T. 2015. The Fork in the Road: Histone Partitioning During DNA Replication. *Genes (Basel),* 6**,** 353-71.

ANNUNZIATO, A. T. & HANSEN, J. C. 2000. Role of histone acetylation in the assembly and modulation of chromatin structures. *Gene Expr,* 9**,** 37-61.

ANNUNZIATO, A. T. & SEALE, R. L. 1983. Histone deacetylation is required for the maturation of newly replicated chromatin. *J Biol Chem,* 258**,** 12675-84.

ATINBAYEVA, N., VALENT, I., ZENK, F., LOESER, E., RAUER, M., HERUR, S., QUARATO, P., PYROWOLAKIS, G., GOMEZ-AULI, A., MITTLER, G., CECERE, G., ERHARDT, S., TIANA, G., ZHAN, Y. & IOVINO, N. 2024. Inheritance of H3K9 methylation regulates genome architecture in Drosophila early embryos. *EMBO J,* 43**,** 2685-2714.

BARRETO-GALVEZ, A., NILJIKAR, M., GAGLIARDI, J., ZHANG, R., KUMAR, V., JURUWALA, A., PRADEEP, A., SHAIKH, A., TIWARI, P., SHARMA, K., GERHARDT, J., CAO, J., KATAOKA, K., DURBIN, A., QI, J., YE, B. H. & MADIREDDY, A. 2023. Acetyl transferase EP300 deficiency leads to chronic replication stress mediated by defective fork protection at stalled replication forks. *bioRxiv*.

BENSON, L. J., GU, Y., YAKOVLEVA, T., TONG, K., BARROWS, C., STRACK, C. L., COOK, R. G., MIZZEN, C. A. & ANNUNZIATO, A. T. 2006. Modifications of H3 and H4 during chromatin replication, nucleosome assembly, and histone exchange. *J Biol Chem,* 281**,** 9287-96.

BEUCHLE, D., STRUHL, G. & MULLER, J. 2001. Polycomb group proteins and heritable silencing of Drosophila Hox genes. *Development,* 128**,** 993-1004.

BHARDWAJ, V., HEYNE, S., SIKORA, K., RABBANI, L., RAUER, M., KILPERT, F., RICHTER, A. S., RYAN, D. P. & MANKE, T. 2019. snakePipes: facilitating flexible, scalable and integrative epigenomic analysis. *Bioinformatics,* 35**,** 4757-4759.

BHATNAGAR, A., KARNAY, A. M. & ELEFANT, F. 2023. Drosophila Epigenetics. *Handbook of Epigenetics*.

BLACKLEDGE, N. P. & KLOSE, R. J. 2021. The molecular principles of gene regulation by Polycomb repressive complexes. *Nat Rev Mol Cell Biol,* 22**,** 815-833.

794 BOIJA, A., MAHAT, D. B., ZARE, A., HOLMQVIST, P. H., PHILIP, P., MEYERS, D. J., COLE, P. A., LIS, J. T., STENBERG, P.
795 & MANNERVIK, M. 2017. CBP Regulates Recruitment and Release of Promoter-Proximal RNA Polymerase II.
796 *Mol Cell,* 68**,** 491-503 e5.

797 BROOKES, E. & SHI, Y. 2014. Diverse epigenetic mechanisms of human disease. *Annu Rev Genet,* 48**,** 237-68.

798 BUENROSTRO, J. D., WU, B., LITZENBURGER, U. M., RUFF, D., GONZALES, M. L., SNYDER, M. P., CHANG, H. Y. &
799 GREENLEAF, W. J. 2015. Single-cell chromatin accessibility reveals principles of regulatory variation. *Nature,*
800 523**,** 486-90.

801 BUTTITTA, L. A. & EDGAR, B. A. 2007. Mechanisms controlling cell cycle exit upon terminal differentiation. *Curr Opin*
802 *Cell Biol,* 19**,** 697-704.

803 BUTTITTA, L. A., KATZAROFF, A. J., PEREZ, C. L., DE LA CRUZ, A. & EDGAR, B. A. 2007. A double-assurance mechanism
804 controls cell cycle exit upon terminal differentiation in Drosophila. *Dev Cell,* 12**,** 631-43.

805 CAO, R., WANG, L., WANG, H., XIA, L., ERDJUMENT-BROMAGE, H., TEMPST, P., JONES, R. S. & ZHANG, Y. 2002. Role
806 of histone H3 lysine 27 methylation in Polycomb-group silencing. *Science,* 298**,** 1039-43.

807 CARDAMONE, F., PIVA, A., LOSER, E., EICHENBERGER, B., ROMERO-MULERO, M. C., ZENK, F., SHIELDS, E. J.,
808 CABEZAS-WALLSCHEID, N., BONASIO, R., TIANA, G., ZHAN, Y. & IOVINO, N. 2025. Chromatin landscape at
809 cis-regulatory elements orchestrates cell fate decisions in early embryogenesis. *Nat Commun,* 16**,** 3007.

810 CAVALLI, G. & HEARD, E. 2019. Advances in epigenetics link genetics to the environment and disease. *Nature,* 571**,**
811 489-499.

812 CAZZALINI, O., SOMMATIS, S., TILLHON, M., DUTTO, I., BACHI, A., RAPP, A., NARDO, T., SCOVASSI, A. I., NECCHI, D.,
813 CARDOSO, M. C., STIVALA, L. A. & PROSPERI, E. 2014. CBP and p300 acetylate PCNA to link its degradation
814 with nucleotide excision repair synthesis. *Nucleic Acids Res,* 42**,** 8433-48.

815 CHEN, Y. C., KOUTELOU, E. & DENT, S. Y. R. 2022. Now open: Evolving insights to the roles of lysine acetylation in
816 chromatin organization and function. *Mol Cell,* 82**,** 716-727.

817 CIABRELLI, F., RABBANI, L., CARDAMONE, F., ZENK, F., LOSER, E., SCHACHTLE, M. A., MAZINA, M., LOUBIERE, V. &
818 IOVINO, N. 2023. CBP and Gcn5 drive zygotic genome activation independently of their catalytic activity. *Sci*
819 *Adv,* 9**,** eadf2687.

820 CLASSEN, A. K., BUNKER, B. D., HARVEY, K. F., VACCARI, T. & BILDER, D. 2009. A tumor suppressor activity of
821 Drosophila Polycomb genes mediated by JAK-STAT signaling. *Nat Genet,* 41**,** 1150-5.

822 COSOLO, A., JAISWAL, J., CSORDAS, G., GRASS, I., UHLIROVA, M. & CLASSEN, A. K. 2019. JNK-dependent cell cycle
823 stalling in G2 promotes survival and senescence-like phenotypes in tissue stress. *Elife,* 8.

824 CRUCIANELLI, C., JAISWAL, J., VIJAYAKUMAR MAYA, A., NOGAY, L., COSOLO, A., GRASS, I. & CLASSEN, A. K. 2022.
825 Distinct signaling signatures drive compensatory proliferation via S-phase acceleration. *PLoS Genet,* 18**,**
826 e1010516.

827 DE MORREE, A. & RANDO, T. A. 2023. Regulation of adult stem cell quiescence and its functions in the maintenance
828 of tissue integrity. *Nat Rev Mol Cell Biol,* 24**,** 334-354.

829 DUTTO, I., SCALERA, C. & PROSPERI, E. 2018. CREBBP and p300 lysine acetyl transferases in the DNA damage
830 response. *Cell Mol Life Sci,* 75**,** 1325-1338.

EATON, M. L., PRINZ, J. A., MACALPINE, H. K., TRETYAKOV, G., KHARCHENKO, P. V. & MACALPINE, D. M. 2011. Chromatin signatures of the Drosophila replication program. *Genome Res,* 21**,** 164-74.

EBERT, A., SCHOTTA, G., LEIN, S., KUBICEK, S., KRAUSS, V., JENUWEIN, T. & REUTER, G. 2004. Su(var) genes regulate the balance between euchromatin and heterochromatin in Drosophila. *Genes Dev,* 18**,** 2973-83.

ESCOBAR, T. M., LOYOLA, A. & REINBERG, D. 2021. Parental nucleosome segregation and the inheritance of cellular identity. *Nat Rev Genet,* 22**,** 379-392.

ESCOBAR, T. M., OKSUZ, O., SALDANA-MEYER, R., DESCOSTES, N., BONASIO, R. & REINBERG, D. 2019. Active and Repressed Chromatin Domains Exhibit Distinct Nucleosome Segregation during DNA Replication. *Cell,* 179**,** 953-963 e11.

FALBO, K. B. & SHEN, X. 2009. Histone modifications during DNA replication. *Mol Cells,* 28**,** 149-54.

FEINBERG, A. P., KOLDOBSKIY, M. A. & GONDOR, A. 2016. Epigenetic modulators, modifiers and mediators in cancer aetiology and progression. *Nat Rev Genet,* 17**,** 284-99.

FLOC'HLAY, S., BALAJI, R., STANKOVIC, D., CHRISTIAENS, V. M., BRAVO GONZALEZ-BLAS, C., DE WINTER, S., HULSELMANS, G. J., DE WAEGENEER, M., QUAN, X., KOLDERE, D., ATKINS, M., HALDER, G., UHLIROVA, M., CLASSEN, A. K. & AERTS, S. 2023. Shared enhancer gene regulatory networks between wound and oncogenic programs. *Elife,* 12.

FLURY, V. & GROTH, A. 2024. Safeguarding the epigenome through the cell cycle: a multitasking game. *Curr Opin Genet Dev,* 85**,** 102161.

HERNANDEZ-SEGURA, A., NEHME, J. & DEMARIA, M. 2018. Hallmarks of Cellular Senescence. *Trends Cell Biol,* 28**,** 436-453.

HOLMQVIST, P. H. & MANNERVIK, M. 2013. Genomic occupancy of the transcriptional co-activators p300 and CBP. *Transcription,* 4**,** 18-23.

HUA, B. L. & ORR-WEAVER, T. L. 2017. DNA Replication Control During Drosophila Development: Insights into the Onset of S Phase, Replication Initiation, and Fork Progression. *Genetics,* 207**,** 29-47.

HUANG, W., HICKSON, L. J., EIRIN, A., KIRKLAND, J. L. & LERMAN, L. O. 2022. Cellular senescence: the good, the bad and the unknown. *Nat Rev Nephrol,* 18**,** 611-627.

IBARRA-MORALES, D., RAUER, M., QUARATO, P., RABBANI, L., ZENK, F., SCHULTE-SASSE, M., CARDAMONE, F., GOMEZ-AULI, A., CECERE, G. & IOVINO, N. 2021. Histone variant H2A.Z regulates zygotic genome activation. *Nat Commun,* 12**,** 7002.

ITO, T. & IGAKI, T. 2021. Yorkie drives Ras-induced tumor progression by microRNA-mediated inhibition of cellular senescence. *Sci Signal,* 14.

JACKSON, V., SHIRES, A., TANPHAICHITR, N. & CHALKLEY, R. 1976. Modifications to histones immediately after synthesis. *J Mol Biol,* 104**,** 471-83.

JAISWAL, J., EGERT, J., ENGESSER, R., PEYROTON, A. A., NOGAY, L., WEICHSELBERGER, V., CRUCIANELLI, C., GRASS, I., KREUTZ, C., TIMMER, J. & CLASSEN, A. K. 2023. Mutual repression between JNK/AP-1 and JAK/STAT stratifies senescent and proliferative cell behaviors during tissue regeneration. *PLoS Biol,* 21**,** e3001665.

JOHNSTON, L. A. & EDGAR, B. A. 1998. Wingless and Notch regulate cell-cycle arrest in the developing Drosophila wing. *Nature,* 394**,** 82-4.

KHAN, C., MULIYIL, S., AYYUB, C. & RAO, B. J. 2017. The initiator caspase Dronc plays a non-apoptotic role in promoting DNA damage signalling in D. melanogaster. *J Cell Sci,* 130**,** 2984-2995.

LANDE-DINER, L., ZHANG, J. & CEDAR, H. 2009. Shifts in replication timing actively affect histone acetylation during nucleosome reassembly. *Mol Cell,* 34**,** 767-74.

LEE, L. A. & ORR-WEAVER, T. L. 2003. Regulation of cell cycles in Drosophila development: intrinsic and extrinsic cues. *Annu Rev Genet,* 37**,** 545-78.

LI, Q., ZHOU, H., WURTELE, H., DAVIES, B., HORAZDOVSKY, B., VERREAULT, A. & ZHANG, Z. 2008. Acetylation of histone H3 lysine 56 regulates replication-coupled nucleosome assembly. *Cell,* 134**,** 244-55.

LIU, W., TANASA, B., TYURINA, O. V., ZHOU, T. Y., GASSMANN, R., LIU, W. T., OHGI, K. A., BENNER, C., GARCIA-BASSETS, I., AGGARWAL, A. K., DESAI, A., DORRESTEIN, P. C., GLASS, C. K. & ROSENFELD, M. G. 2010. PHF8 mediates histone H4 lysine 20 demethylation events involved in cell cycle progression. *Nature,* 466**,** 508-12.

LOPEZ-HERNANDEZ, L., TOOLAN-KERR, P., BANNISTER, A. J. & MILLAN-ZAMBRANO, G. 2025. Dynamic histone modification patterns coordinating DNA processes. *Mol Cell,* 85**,** 225-237.

MA, Y., KANAKOUSAKI, K. & BUTTITTA, L. 2015. How the cell cycle impacts chromatin architecture and influences cell fate. *Front Genet,* 6**,** 19.

MADIGAN, J. P., CHOTKOWSKI, H. L. & GLASER, R. L. 2002. DNA double-strand break-induced phosphorylation of Drosophila histone variant H2Av helps prevent radiation-induced apoptosis. *Nucleic Acids Res,* 30**,** 3698-705.

MARSH, A. J., PIROGOV, S., KAUR, Y., RUFFRIDGE, A. J., SAJWAN, S., GIBSON, T. J., HUNT, G., HARRISON, M. M. & MANNERVIK, M. 2025. Catalytic-dependent and independent functions of the histone acetyltransferase CBP promote pioneer-factor-mediated zygotic genome activation. *Mol Cell*.

MASUMOTO, H., HAWKE, D., KOBAYASHI, R. & VERREAULT, A. 2005. A role for cell-cycle-regulated histone H3 lysine 56 acetylation in the DNA damage response. *Nature,* 436**,** 294-8.

MATTHEWS, H. K., BERTOLI, C. & DE BRUIN, R. A. M. 2022. Cell cycle control in cancer. *Nat Rev Mol Cell Biol,* 23**,** 74-88.

MAYA, A. V., NOGAY, L., HECKMANN, L., GRASS, I., KIERDORF, K., BüSCHER, J. & CLASSEN, A.-K. 2024. PDK-1/S6K and mTORC1 bypass systemic growth restrictions to promote regeneration. *bioRxiv***,** 2024.08.05.606658.

MCCONNELL, K. H., DIXON, M. & CALVI, B. R. 2012. The histone acetyltransferases CBP and Chameau integrate developmental and DNA replication programs in Drosophila ovarian follicle cells. *Development,* 139**,** 3880-90.

MENDIRATTA, S., GATTO, A. & ALMOUZNI, G. 2019. Histone supply: Multitiered regulation ensures chromatin dynamics throughout the cell cycle. *J Cell Biol,* 218**,** 39-54.

MILAN, M., CAMPUZANO, S. & GARCIA-BELLIDO, A. 1996. Cell cycling and patterned cell proliferation in the wing primordium of Drosophila. *Proc Natl Acad Sci U S A,* 93**,** 640-5.

MILLAN-ZAMBRANO, G., BURTON, A., BANNISTER, A. J. & SCHNEIDER, R. 2022. Histone post-translational modifications - cause and consequence of genome function. *Nat Rev Genet,* 23**,** 563-580.

MULLER, J., GAUNT, S. & LAWRENCE, P. A. 1995. Function of the Polycomb protein is conserved in mice and flies. *Development,* 121**,** 2847-52.

NARITA, M., NUNEZ, S., HEARD, E., NARITA, M., LIN, A. W., HEARN, S. A., SPECTOR, D. L., HANNON, G. J. & LOWE, S. W. 2003. Rb-mediated heterochromatin formation and silencing of E2F target genes during cellular senescence. *Cell,* 113**,** 703-16.

NEUFELD, T. P., DE LA CRUZ, A. F., JOHNSTON, L. A. & EDGAR, B. A. 1998. Coordination of growth and cell division in the Drosophila wing. *Cell,* 93**,** 1183-93.

ODA, H., HUBNER, M. R., BECK, D. B., VERMEULEN, M., HURWITZ, J., SPECTOR, D. L. & REINBERG, D. 2010. Regulation of the histone H4 monomethylase PR-Set7 by CRL4(Cdt2)-mediated PCNA-dependent degradation during DNA damage. *Mol Cell,* 40**,** 364-76.

OGIWARA, H., UI, A., OTSUKA, A., SATOH, H., YOKOMI, I., NAKAJIMA, S., YASUI, A., YOKOTA, J. & KOHNO, T. 2011. Histone acetylation by CBP and p300 at double-strand break sites facilitates SWI/SNF chromatin remodeling and the recruitment of non-homologous end joining factors. *Oncogene,* 30**,** 2135-46.

PADEKEN, J., METHOT, S. P. & GASSER, S. M. 2022. Establishment of H3K9-methylated heterochromatin and its functions in tissue differentiation and maintenance. *Nat Rev Mol Cell Biol,* 23**,** 623-640.

PENGELLY, A. R., COPUR, O., JACKLE, H., HERZIG, A. & MULLER, J. 2013. A histone mutant reproduces the phenotype caused by loss of histone-modifying factor Polycomb. *Science,* 339**,** 698-9.

PETERMANN, E., ORTA, M. L., ISSAEVA, N., SCHULTZ, N. & HELLEDAY, T. 2010. Hydroxyurea-stalled replication forks become progressively inactivated and require two different RAD51-mediated pathways for restart and repair. *Mol Cell,* 37**,** 492-502.

PETERSON, C. L. & LANIEL, M. A. 2004. Histones and histone modifications. *Curr Biol,* 14**,** R546-51.

PETRUK, S., BLACK, K. L., KOVERMANN, S. K., BROCK, H. W. & MAZO, A. 2013. Stepwise histone modifications are mediated by multiple enzymes that rapidly associate with nascent DNA during replication. *Nat Commun,* 4**,** 2841.

PETRUK, S., SEDKOV, Y., SMITH, S., TILLIB, S., KRAEVSKI, V., NAKAMURA, T., CANAANI, E., CROCE, C. M. & MAZO, A. 2001. Trithorax and dCBP acting in a complex to maintain expression of a homeotic gene. *Science,* 294**,** 1331-4.

PHILIP, P., BOIJA, A., VAID, R., CHURCHER, A. M., MEYERS, D. J., COLE, P. A., MANNERVIK, M. & STENBERG, P. 2015. CBP binding outside of promoters and enhancers in Drosophila melanogaster. *Epigenetics Chromatin,* 8**,** 48.

PROBER, D. A. & EDGAR, B. A. 2000. Ras1 promotes cellular growth in the Drosophila wing. *Cell,* 100**,** 435-46.

RAMADAN, W. S., AHMED, S. B. M., TALAAT, I. M., LOZON, L., MOUFFAK, S., GEMOLL, T., MANSOUR, W. Y. & EL-AWADY, R. 2025. The histone acetyltransferase CBP participates in regulating the DNA damage response through ATM after double-strand breaks. *Genome Biol,* 26**,** 89.

RAMOS-ALONSO, L. & CHYMKOWITCH, P. 2024. Maintaining transcriptional homeostasis during cell cycle. *Transcription,* 15**,** 1-21.

940 REVERON-GOMEZ, N., GONZALEZ-AGUILERA, C., STEWART-MORGAN, K. R., PETRYK, N., FLURY, V., GRAZIANO, S.,
941 JOHANSEN, J. V., JAKOBSEN, J. S., ALABERT, C. & GROTH, A. 2018. Accurate Recycling of Parental Histones
942 Reproduces the Histone Modification Landscape during DNA Replication. *Mol Cell,* 72**,** 239-249 e5.

943 RUIZ-CARRILLO, A., WANGH, L. J. & ALLFREY, V. G. 1975. Processing of newly synthesized histone molecules.
944 *Science,* 190**,** 117-28.

945 SCHINDELIN, J., ARGANDA-CARRERAS, I., FRISE, E., KAYNIG, V., LONGAIR, M., PIETZSCH, T., PREIBISCH, S.,
946 RUEDEN, C., SAALFELD, S., SCHMID, B., TINEVEZ, J. Y., WHITE, D. J., HARTENSTEIN, V., ELICEIRI, K.,
947 TOMANCAK, P. & CARDONA, A. 2012. Fiji: an open-source platform for biological-image analysis. *Nat*
948 *Methods,* 9**,** 676-82.

949 SMITH-BOLTON, R. K., WORLEY, M. I., KANDA, H. & HARIHARAN, I. K. 2009. Regenerative growth in Drosophila
950 imaginal discs is regulated by Wingless and Myc. *Dev Cell,* 16**,** 797-809.

951 SMOLIK, S. & JONES, K. 2007. Drosophila dCBP is involved in establishing the DNA replication checkpoint. *Mol Cell*
952 *Biol,* 27**,** 135-46.

953 SOBEL, R. E., COOK, R. G., PERRY, C. A., ANNUNZIATO, A. T. & ALLIS, C. D. 1995. Conservation of deposition-related
954 acetylation sites in newly synthesized histones H3 and H4. *Proc Natl Acad Sci U S A,* 92**,** 1237-41.

955 SPARMANN, A. & VAN LOHUIZEN, M. 2006. Polycomb silencers control cell fate, development and cancer. *Nat Rev*
956 *Cancer,* 6**,** 846-56.

957 STAUFFER, D., CHANG, B., HUANG, J., DUNN, A. & THAYER, M. 2007. p300/CREB-binding protein interacts with ATR
958 and is required for the DNA replication checkpoint. *J Biol Chem,* 282**,** 9678-9687.

959 STEIN, G., PARK, W., THRALL, C., MANS, R. & STEIN, J. 1975. Regulation of cell cycle stage-specific transcription of
960 histone genes from chromatin by non-histone chromosomal proteins. *Nature,* 257**,** 764-7.

961 STEWART-MORGAN, K. R., PETRYK, N. & GROTH, A. 2020. Chromatin replication and epigenetic cell memory. *Nat Cell*
962 *Biol,* 22**,** 361-371.

963 TAPON, N., MOBERG, K. H. & HARIHARAN, I. K. 2001. The coupling of cell growth to the cell cycle. *Curr Opin Cell Biol,*
964 13**,** 731-7.

965 TESSARZ, P. & KOUZARIDES, T. 2014. Histone core modifications regulating nucleosome structure and dynamics. *Nat*
966 *Rev Mol Cell Biol,* 15**,** 703-8.

967 TIE, F., BANERJEE, R., FU, C., STRATTON, C. A., FANG, M. & HARTE, P. J. 2016. Polycomb inhibits histone acetylation
968 by CBP by binding directly to its catalytic domain. *Proc Natl Acad Sci U S A,* 113**,** E744-53.

969 TIE, F., BANERJEE, R., STRATTON, C. A., PRASAD-SINHA, J., STEPANIK, V., ZLOBIN, A., DIAZ, M. O., SCACHERI, P. C. &
970 HARTE, P. J. 2009. CBP-mediated acetylation of histone H3 lysine 27 antagonizes Drosophila Polycomb
971 silencing. *Development,* 136**,** 3131-41.

972 TILLHON, M., CAZZALINI, O., NARDO, T., NECCHI, D., SOMMATIS, S., STIVALA, L. A., SCOVASSI, A. I. & PROSPERI, E.
973 2012. p300/CBP acetyl transferases interact with and acetylate the nucleotide excision repair factor XPG.
974 *DNA Repair (Amst),* 11**,** 844-52.

975 TROUTH, A., RAVICHANDRAN, K., GAFKEN, P. R., MARTIRE, S., BOYLE, G. E., VERONEZI, G. M. B., LA, V., NAMCIU, S.
976 J., BANASZYNSKI, L. A., SARTHY, J. F. & RAMACHANDRAN, S. 2025. The length of the G1 phase is an essential
977 determinant of H3K27me3 landscapes across diverse cell types. *PLoS Biol,* 23**,** e3003119.

TROVATO, M., PATIL, V., GEHRE, M. & NOH, K. M. 2020. Histone Variant H3.3 Mutations in Defining the Chromatin Function in Mammals. *Cells,* 9.

VERREAULT, A., KAUFMAN, P. D., KOBAYASHI, R. & STILLMAN, B. 1998. Nucleosomal DNA regulates the core-histone-binding subunit of the human Hat1 acetyltransferase. *Curr Biol,* 8**,** 96-108.

WENGER, A., BIRAN, A., ALCARAZ, N., REDO-RIVEIRO, A., SELL, A. C., KRAUTZ, R., FLURY, V., REVERON-GOMEZ, N., SOLIS-MEZARINO, V., VOLKER-ALBERT, M., IMHOF, A., ANDERSSON, R., BRICKMAN, J. M. & GROTH, A. 2023. Symmetric inheritance of parental histones governs epigenome maintenance and embryonic stem cell identity. *Nat Genet,* 55**,** 1567-1578.

WILLNOW, P. & TELEMAN, A. A. 2024. Nuclear position and local acetyl-CoA production regulate chromatin state. *Nature,* 630**,** 466-474.

YAO, T. P., OH, S. P., FUCHS, M., ZHOU, N. D., CH'NG, L. E., NEWSOME, D., BRONSON, R. T., LI, E., LIVINGSTON, D. M. & ECKNER, R. 1998. Gene dosage-dependent embryonic development and proliferation defects in mice lacking the transcriptional integrator p300. *Cell,* 93**,** 361-72.

ZANG, Y., YOSHIMOTO, M. & IGAKI, T. 2025. Programmed cell senescence is required for sensory organ development in Drosophila. *iScience,* 28**,** 112048.

ZEE, B. M., BRITTON, L. M., WOLLE, D., HABERMAN, D. M. & GARCIA, B. A. 2012. Origins and formation of histone methylation across the human cell cycle. *Mol Cell Biol,* 32**,** 2503-14.

ZENK, F., CARDAMONE, F., IBARRA MORALES, D. A., ATINBAYEVA, N., ZHAN, Y. & IOVINO, N. 2023. Analyzing the Genome-Wide Distribution of Histone Marks by CUT&Tag in Drosophila Embryos. *Methods Mol Biol,* 2655**,** 1-17.

ZHOU, C. Y. & HEALD, R. 2020. Emergent properties of mitotic chromosomes. *Curr Opin Cell Biol,* 64**,** 43-49.

ZIELKE, N., KORZELIUS, J., VAN STRAATEN, M., BENDER, K., SCHUHKNECHT, G. F. P., DUTTA, D., XIANG, J. & EDGAR, B. A. 2014. Fly-FUCCI: A versatile tool for studying cell proliferation in complex tissues. *Cell Rep,* 7**,** 588-598.

1003 **Table S1 Experimental strains, reagents and software**

1004

Tool	Source	ID
w^{118}	David Bilder, University of California, Berkeley	FBal0018157
UAS-GFP^{S56T}	Bloomington *Drosophila* Stock Center	BDSC: 1521
$rn^{GAL4\text{-}DeltaS}$, tubGAL80^{ts}	Bloomington *Drosophila* Stock Center	BDSC: 8142; 7018 recombinant
$rn^{GAL4\text{-}5}$, UAS-egr, tubP-GAL80^{ts}	Iswar Hariharan, University of California, Berkeley	BDSC: 8142; 7018 recombinant
'E2F1-FUCCI, CycB-FUCCI'; Ubi-GFP.E2f1$^{1\text{-}230}$, Ubi-mRFP1.NLS.CycB$^{1\text{-}266}$	Bloomington *Drosophila* Stock Center	BDSC: 55123
UAS-Cdk1 RNAi [TRiP.HMS01531]	Bloomington *Drosophila* Stock Center	BDSC: 36117
If/CyO-GFP; UAS-E2F, UAS-DP/TM6b	Laura Buttitta, University of Michigan	PMID: 9657151
UAS-pnt.P1	Bloomington *Drosophila* Stock Center	BDSC: 869
UAS-E(z)-RNAi (TRiP.HMS00066)	Bloomington *Drosophila* Stock Center	BDSC: 33659
UAS-nejire-RNAi(TRiP.HMS01507)	Bloomington *Drosophila* Stock Center	BDSC: 37489
UAS-InR-DA (UAS-InR.A1325D)	Bloomington *Drosophila* Stock Center	BDSC: 8263
'TRE-RFP': TRE-DsRed.T4	Dirk Bohmann, University of Rochester Medical Center	PMID: 22509270
UAS-nejire	Bloomington *Drosophila* Stock Center	BDSC: 32573
UAS-HDAC1-RNAi (TRiP.HMS00607)	Bloomington *Drosophila* Stock Center	BDSC: 33725
CBP-GFP	Melissa Harrison, University of Wisconsin School of Medicine and Public Health	PMID: 40441155

w; Df(2L)HisC FRT40A/CyO, twi-GAL4, UAS-GFP; 6xHisGU^{H3K27R}/6xHisGU^{H3K27R}	Jürg Müller, Max Planck Institute of Biochemistry	PMID: 23393264
yw hs-flp122; hs-nGFP FRT40A; 6xHisGU$^{H3-K27R}$/SM5^TM6B	Jürg Müller, Max Planck Institute of Biochemistry	PMID: 23393264
hs-flp122; FRT40A ubi-GFP/CyO (GFP); Dr/TM6c		
UAS-bsk[DN]	Bloomington *Drosophila* Stock Center	BDSC: 6409
Chicken anti-GFP	Abcam	Cat. #: ab13970
Rabbit monoclonal anti-GFP	Invitrogen	Cat. #: G10362
Rat monoclonal anti-RFP	ChromoTek	Cat. #: 5F8 RRID: AB_2336064
Rabbit polyclonal anti-H3K9ac	Active motif	Cat. #: 39017 RRID: AB_2616593
Rabbit polyclonal anti-H4K8ac	Active motif	Cat. #: 61104 RRID: AB_2793506
Rabbit polyclonal anti-acetyl Lysine	Abcam	Cat. #: ab80178
Rabbit monoclonal anti-crotonyl Histone H3	PTMab	Cat. #: PTM-517RM
Rabbit polyclonal anti-H3K9me1me2me3	Active motif	Cat. #: 39242 RRID: AB_2793200
Rabbit polyclonal anti-H3K18ac	Active motif	Cat. #: 39756 RRID: AB_2714186
Mouse monoclonal anti-H3K27ac	Active motif	Cat. #: 39085 RRID: AB_2793305
Rabbit polyclonal anti-H3K4me3	Abcam	Cat. #: ab8580
Mouse monoclonal anti-H3K27me3	Abcam	Cat. #: ab6002
Rabbit polyclonal anti-H3K9me3	Abcam	Cat. #: ab8898
Rabbit polyclonal anti-H3	Abcam	Cat. #: ab1791
Rabbit polyclonal anti-Histone H2AvD phosphoS137	Rockland	Cat. #: 600-401-914
Mouse monoclonal anti-Cut	DSHB	Cat. #: 2B10 RRID: AB_528186
Mouse monoclonal anti-Engrailed/Invected	DSHB	Cat. #: 4D9 RRID: AB_528224

Mouse monoclonal anti-Nubbin	DSHB	Cat. #: 2D4 RRID: AB_2722119
Mouse monoclonal anti-Antp	DSHB	Cat. #: 8C11 RRID: AB_528083
Mouse monoclonal anti-Ptc	DSHB	Cat. #: Apa1 RRID: AB_528441
Mouse monoclonal anti Abd-B	DSHB	Cat. #: 1A2E9 RRID: AB_528061
Mouse monoclonal anti-Wg	DSHB	Cat. #: 4D4 RRID: AB_528512
Mouse monoclonal anti-Histone H3 (for CUT&Tag)	Active motif	Cat. #: 39763 RRID: AB_2650522
Rabbit polyclonal anti-H3K27ac (for CUT&Tag)	Diagenode	Cat. #: C15410196
Rabbit polyclonal anti-H3K27me3 (for CUT&Tag)	Diagendoe	Cat. #: C15410195
Rabbit monoclonal anti-H3K9me3 (for CUT&Tag)	Abcam	Cat. #: ab176916
DAPI	Sigma Aldrich	Cat #: D9564
Goat anti-mouse IgG Alexa Flour 488	Invitrogen	Cat. #: A-11001
Goat anti-chicken IgY Alexa Flour 488	Invitrogen	Cat. #: A-11039
Goat anti-rabbit IgG Alexa Flour 488	Invitrogen	Cat. #: A-11008
Goat anti-mouse IgG Alexa Flour 555	Invitrogen	Cat. #: A-21422
Goat anti-rat IgG Alexa Flour 555	Invitrogen	Cat. #: A-21434
Goat anti-mouse Alexa Flour 647	Invitrogen	Cat. #: A-21235
Donkey anti-mouse Alexa Flour 647 preabsorbed	Abcam	Cat. #: ab150111
Goat anti-rat Alexa Flour 647	Invitrogen	Cat. #: A-21247
Goat anti-rabbit Alexa Flour 647	Invitrogen	Cat. #: A-21244
Click-iT Plus EdU Alexa Fluor 647 Imaging Kit	Invitrogen	Cat. #: C10640
Click-iT Plus OPP Alexa Fluor 647 Imaging Kit	Invitrogen	Cat. #: C10458
CellEvent Senescence Green Detection Kit	Invitrogen	Cat. #: C10850
FIJI (ImageJ 1.54f)	(Schindelin et al., 2012)	https://fiji.sc/

GraphPad Prism	Graph Pad	version 9.5.0
Affinity Designer	Affinity	Up to version 2.6.3
Biorender	Science Suite Inc. DBA BioRender	Biorender

MAIN FIGURES

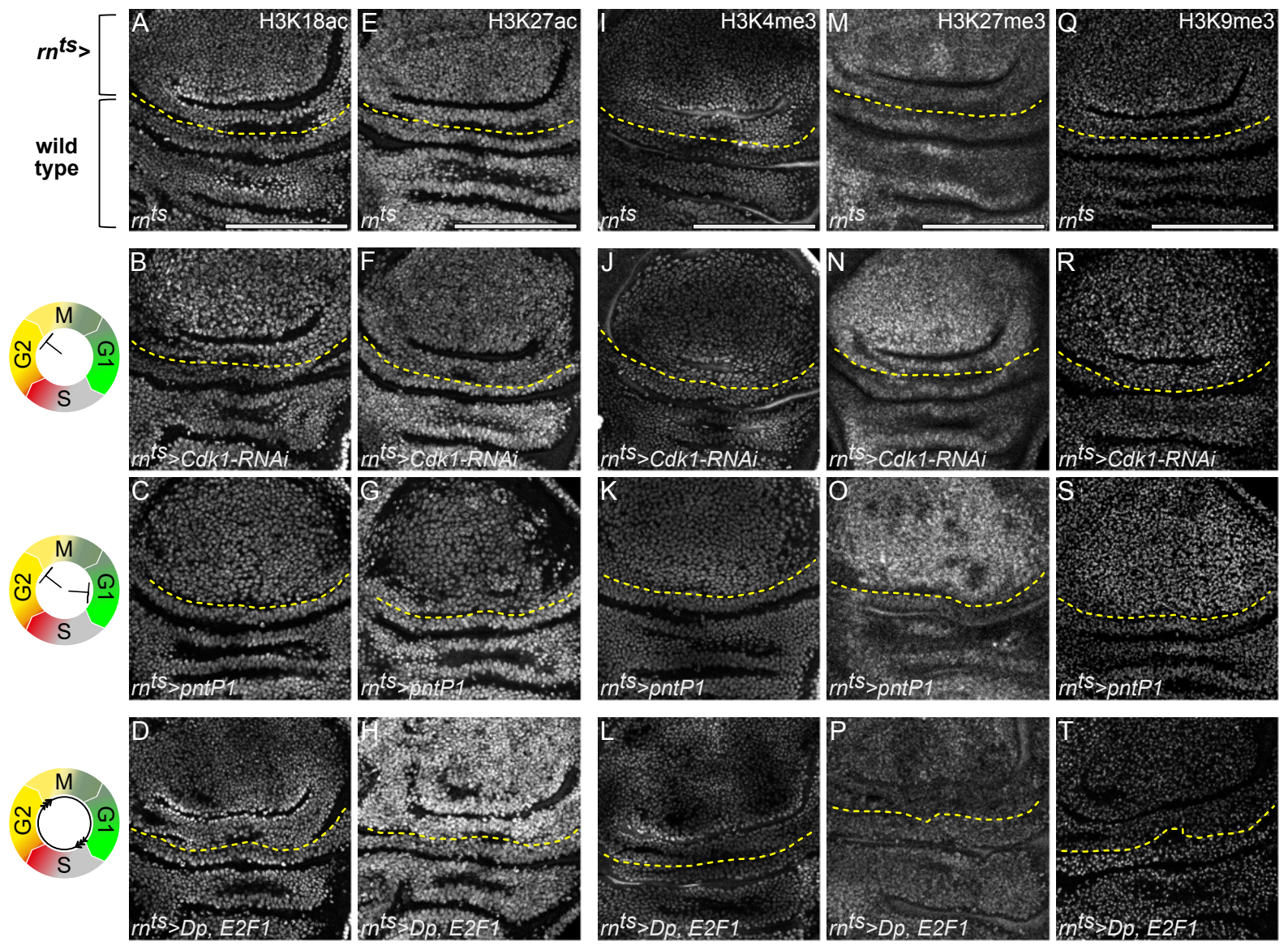
rnts>
wild type
A H3K18ac
E H3K27ac
I H3K4me3
M H3K27me3
Q H3K9me3
rnts
B
F
J
N
R
rnts>Cdk1-RNAi
C
G
K
O
S
rnts>pntP1
D
H
L
P
T
rnts>Dp, E2F1
M
G1
S
G2

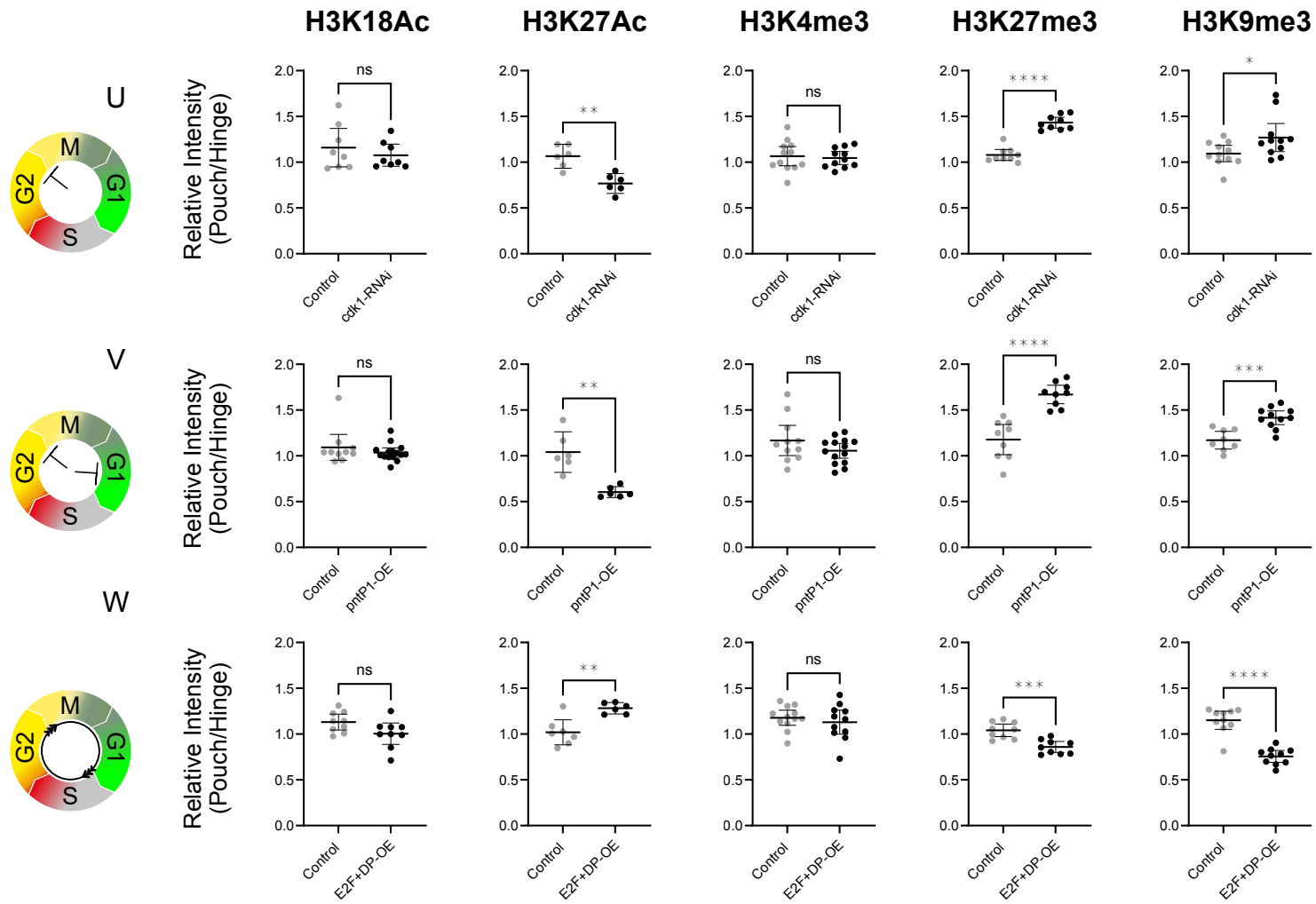
H3K18Ac
H3K27Ac
H3K4me3
H3K27me3
H3K9me3
U
V
W
Relative Intensity (Pouch/Hinge)
ns
**
****
*
***
Control
cdk1-RNAi
pntP1-OE
E2F+DP-OE
0.0
0.5
1.0
1.5
2.0

1

Figure 1. H3K27ac, H3K27me3, and H3K9me3 levels respond to changes in cell cycle dynamics

Icons represent the experimentally verified FUCCI cell cycle status in each condition: G2-phase arrest in *Cdk1-RNAi*-expressing discs, either G1 or G2-phase arrest in *pntP1*-expressing discs, and cell cycle acceleration in *Dp, E2F1*-overexpressing discs. For better guidance through subsequent figures, schemes already introduce FUCCI reporter read-outs for phase G1 (green), early S-phase (grey), late S-phase (red) and G2 (yellow).

A-D. Immunostaining for H3K18ac in control **(A)**, *Cdk1-RNAi*-expressing **(B)**, *pntP1*-expressing **(C)** and *Dp, E2F1*-expressing **(D)** discs. Expression was induced for 24 h in the wing pouch using *rn-GAL4*. The *rn-GAL4* expressing pouch domain is represented by the tissue above the yellow line (rn^{ts}>). The tissue below the yellow line represents wild type tissues of the hinge.

E-T. Immunostaining for H3K27ac **(E-H)**, H3K4me3 **(I-L)**, H3K27me3 **(M-P)**, H3K9me3 **(Q-T)** in control **(E,I,M,Q)**, *Cdk1-RNAi*-expressing **(F,J,N,R)**, *pntP1*-expressing **(G,K,O,S)** and *Dp, E2F1*-expressing **(H,L,P,T)** discs.

U. Quantification of relative signal intensities for H3K18ac, H3K27ac, H3K4me3, H3K27me3, and H3K9me3, presented as pouch-to-hinge ratios (i.e., rn^{ts}-to-wild-type-cell ratio) in *Cdk1-RNAi*-expressing discs. Mean and 95% CI is shown. Statistical significance was tested using two-tailed Mann-Whitney test, p value= 0.9591 for H3K18ac (control discs: n=8, *Cdk1-RNAi*-expressing discs: n=8); two-tailed Unpaired t test, p value=0.0012 for H3K27ac (control discs: n=6, *Cdk1-RNAi*-expressing discs: n=6); two-tailed Unpaired t test, p value=0.7334 for H3K4me3 (control discs: n=12, *Cdk1-RNAi*-expressing discs: n=11); two-tailed Unpaired t test, p value<0.0001 for H3K27me3 (control discs: n=9, *Cdk1-RNAi*-expressing discs: n=9); two-tailed Mann-Whitney test, p value=0.0473 for H3K9me3 (control discs: n=11, *Cdk1-RNAi*-expressing discs: n=11).

V. Quantification of relative signal intensities for H3K18ac, H3K27ac, H3K4me3, H3K27me3, and H3K9me3, presented as pouch-to-hinge ratios (i.e., rn^{ts}-to-wild-type-cell ratio) in *pntP1*-expressing discs. Mean and 95% CI is shown. Statistical significance was tested using two-tailed Mann-Whitney test, p value= 0.5671 for H3K18ac (control discs: n=10, *pntP1*-expressing discs: n=15); two-tailed Welch's t test, p value=0.0031 for H3K27ac (control discs: n=6, *pntP1*-expressing discs: n=6); two-tailed Unpaired t test, p value=0.1614 for H3K4me3 (control discs: n=11, *pntP1*-expressing discs: n=14); two-tailed Unpaired t test, p value<0.0001 for H3K27me3 (control discs: n=9, *pntP1*-expressing discs: n=9); two-tailed Unpaired t test, p value=0.0002 for H3K9me3 (control discs: n=8, *pntP1*-expressing discs: n=11).

W. Quantification of relative signal intensities for H3K18ac, H3K27ac, H3K4me3, H3K27me3, and H3K9me3, presented as pouch-to-hinge ratios (i.e., rn^{ts}-to-wild-type-cell ratio) in *Dp, E2F1*-coexpressing

discs. Mean and 95% CI is shown. Statistical significance was tested using two-tailed Unpaired t test, p value= 0.0609 for H3K18ac (control discs: n=9, *Dp, E2F1*-coexpressing discs: n=9); two-tailed Unpaired t test, p value=0.0019 for H3K27ac (control discs: n=7, *Dp, E2F1*-coexpressing discs: n=6); two-tailed Unpaired t test, p value=0.4837 for H3K4me3 (control discs: n=12, *Dp, E2F1*-coexpressing discs: n=11); two-tailed Unpaired t test, p value=0.0003 for H3K27me3 (control discs: n=9, *Dp, E2F1*-coexpressing discs: n=9); two-tailed Mann-Whitney test, p value<0.0001 for H3K9me3 (control discs: n=10, *Dp, E2F1*-coexpressing discs: n=10).

Fluorescence intensities are reported as arbitrary units.

Sum projections of multiple confocal sections are shown in **C**, **K**, **M-N**, **O** and **Q-R.**

Maximum projections of multiple confocal sections are shown in **A-B**, **E-F**, **G**, **H**, **I-J**, **P**, **S** and **T**.

Scale bars: 100 µm.

Please refer to **(Fig S1.3A)** for corresponding DAPI images of all discs shown.

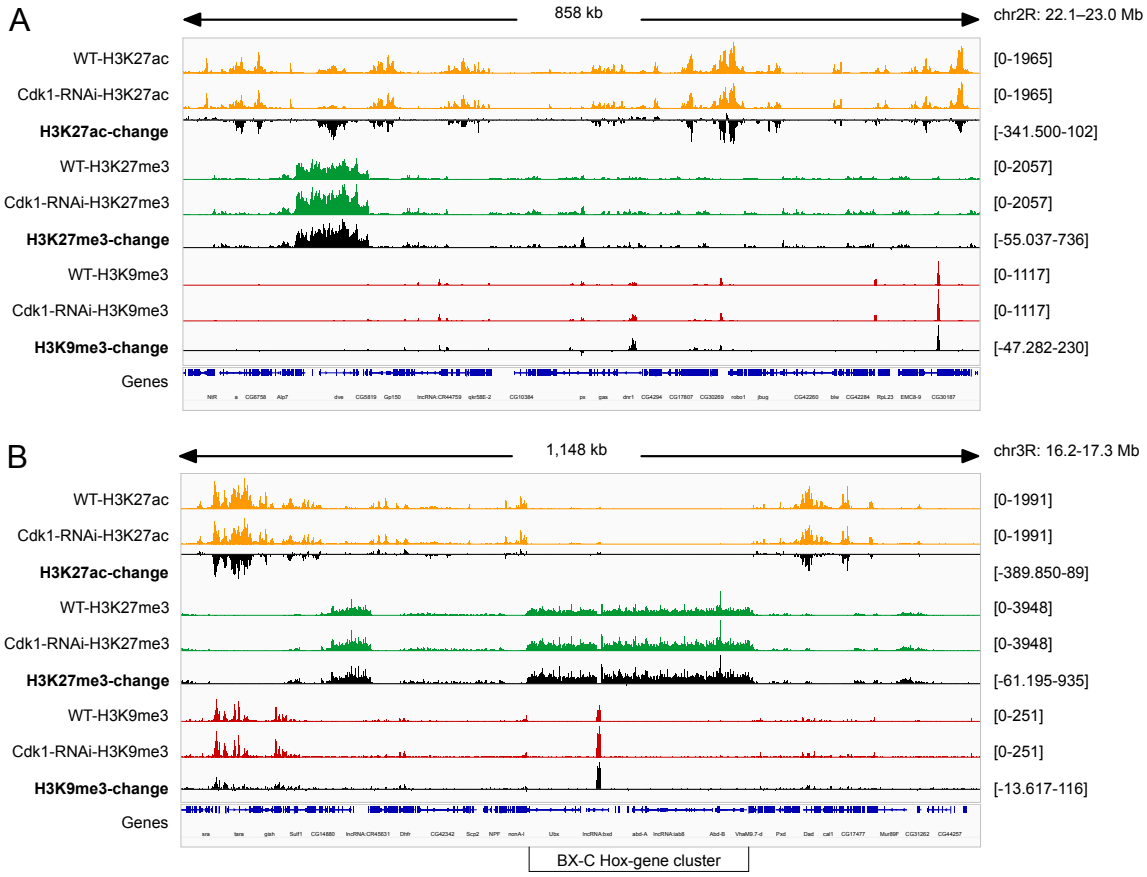
A
858 kb
chr2R: 22.1–23.0 Mb
WT-H3K27ac
Cdk1-RNAi-H3K27ac
H3K27ac-change
WT-H3K27me3
Cdk1-RNAi-H3K27me3
H3K27me3-change
WT-H3K9me3
Cdk1-RNAi-H3K9me3
H3K9me3-change
Genes
[0-1965]
[0-1965]
[-341.500-102]
[0-2057]
[0-2057]
[-55.037-736]
[0-1117]
[0-1117]
[-47.282-230]
B
1,148 kb
chr3R: 16.2-17.3 Mb
WT-H3K27ac
Cdk1-RNAi-H3K27ac
H3K27ac-change
WT-H3K27me3
Cdk1-RNAi-H3K27me3
H3K27me3-change
WT-H3K9me3
Cdk1-RNAi-H3K9me3
H3K9me3-change
Genes
[0-1991]
[0-1991]
[-389.850-89]
[0-3948]
[0-3948]
[-61.195-935]
[0-251]
[0-251]
[-13.617-116]
BX-C Hox-gene cluster

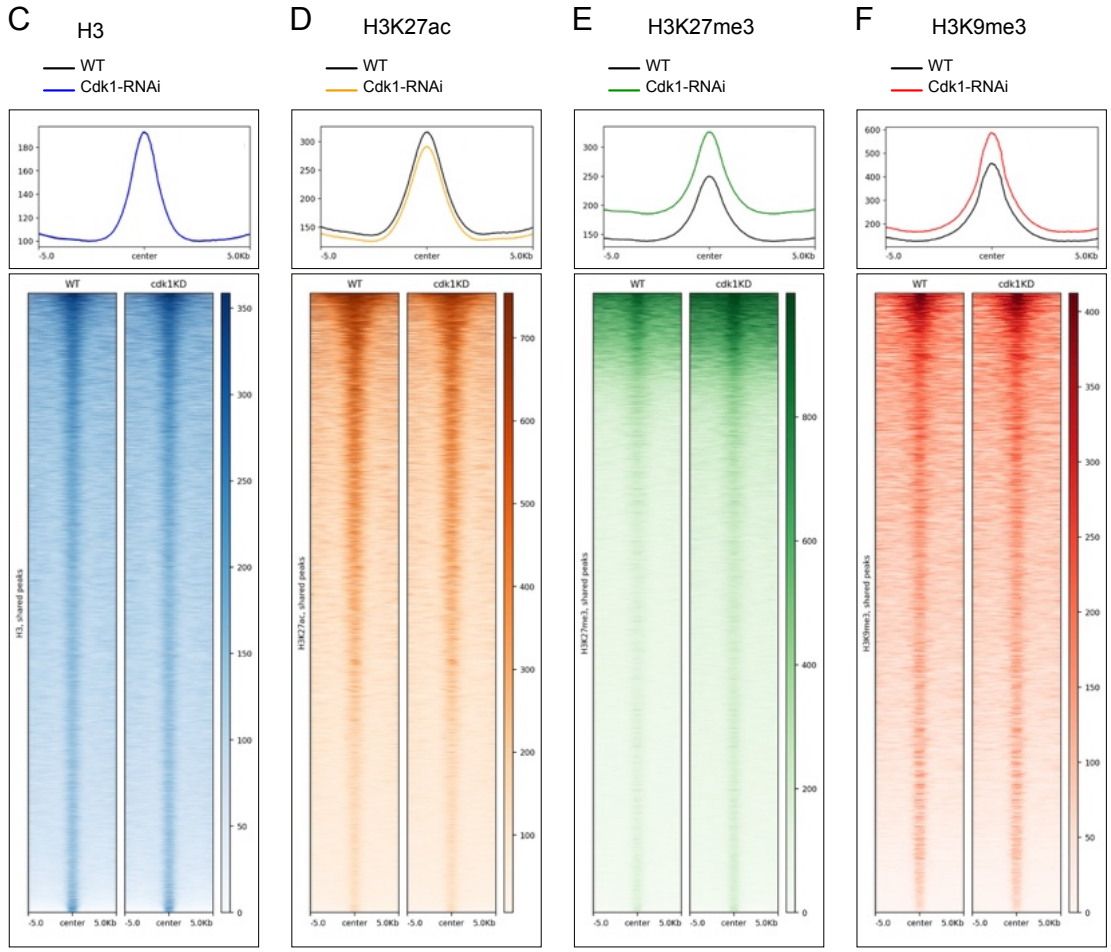
C
H3
WT
Cdk1-RNAi
D
H3K27ac
WT
Cdk1-RNAi
E
H3K27me3
WT
Cdk1-RNAi
F
H3K9me3
WT
Cdk1-RNAi
WT
cdk1KD
center
-5.0
5.0Kb

Figure 2. Cell cycle-dependent changes in H3K27ac, H3K27me3, and H3K9me3 occur at preexisting genomic sites

---

A-B. Two examples of genomic snapshots of CUT&Tag profiles comparing levels of H3K27ac, H3K27me3 and H3K9me3 in wild type wing discs and in wing discs having expressed *Cdk1*-RNAi for 24 h in the pouch region under the control of rn-GAL4. Tracks for H3K27ac (orange), H3K27me3 (green), and H3K9me3 (red) were normalized against H3 as described in the Materials and Methods and were then visualized using IGV. Black tracks represent the change between control and knockdown conditions computed by subtracting number of sequence reads in *Cdk1-RNAi*-expressing discs from wild type discs for each histone modification. Tracks in **(B)** cover the BX-C Hox gene cluster encoding Ubx, Abd-A and Abd-B targeted by Polycomb silencing.

C-F. Profile plots and heatmaps showing normalized CUT&Tag signals at peaks shared between wild type control and *Cdk1-RNAi*-expressing discs for H3 **(C)**, H3K27ac **(D)**, H3K27me3 **(E)**, and H3K9me3 **(F)** (see Materials and Methods). Averaged and individual signal intensities are centered ±5 kb around the shared peak.

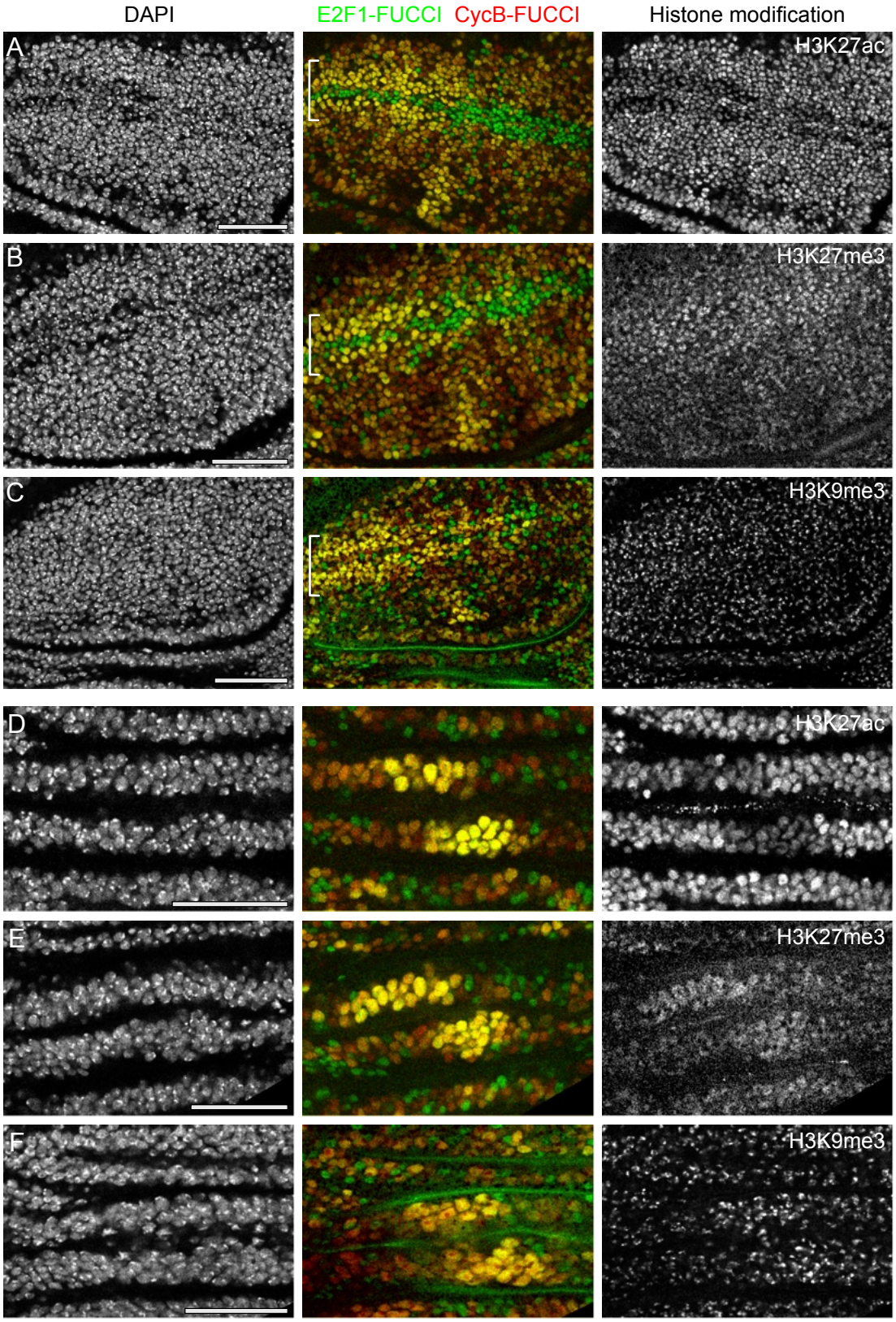
DAPI
E2F1-FUCCI CycB-FUCCI
Histone modification
A
H3K27ac
B
H3K27me3
C
H3K9me3
D
H3K27ac
E
H3K27me3
F
H3K9me3

Figure 3. Developmentally arrested cell populations under physiological conditions exhibit changes in H3K27ac, H3K27me3, and H3K9me3 levels

---

A-C. Immunostaining for H3K27ac **(A)**, H3K27me3 **(B)**, and H3K9me3 **(C)** in the zone of non-proliferating cells (ZNC) of developing wing discs. Cells in the ZNC (white brackets) are arrested in either G1 or G2 phase, and can be identified by the Fly-FUCCI reporter. Among the histone modifications examined, only H3K27ac, H3K27me3, and H3K9me3 exhibit cell cycle arrest associated changes in the ZNC.

D-F. Immunostaining for H3K27ac **(D)**, H3K27me3 **(E)** and H3K9me3 **(F)** in a hinge cell population undergoing programmed senescence in developing wing discs.

Discs were stained with DAPI to visualize nuclei.

Scale bars: 50 μm

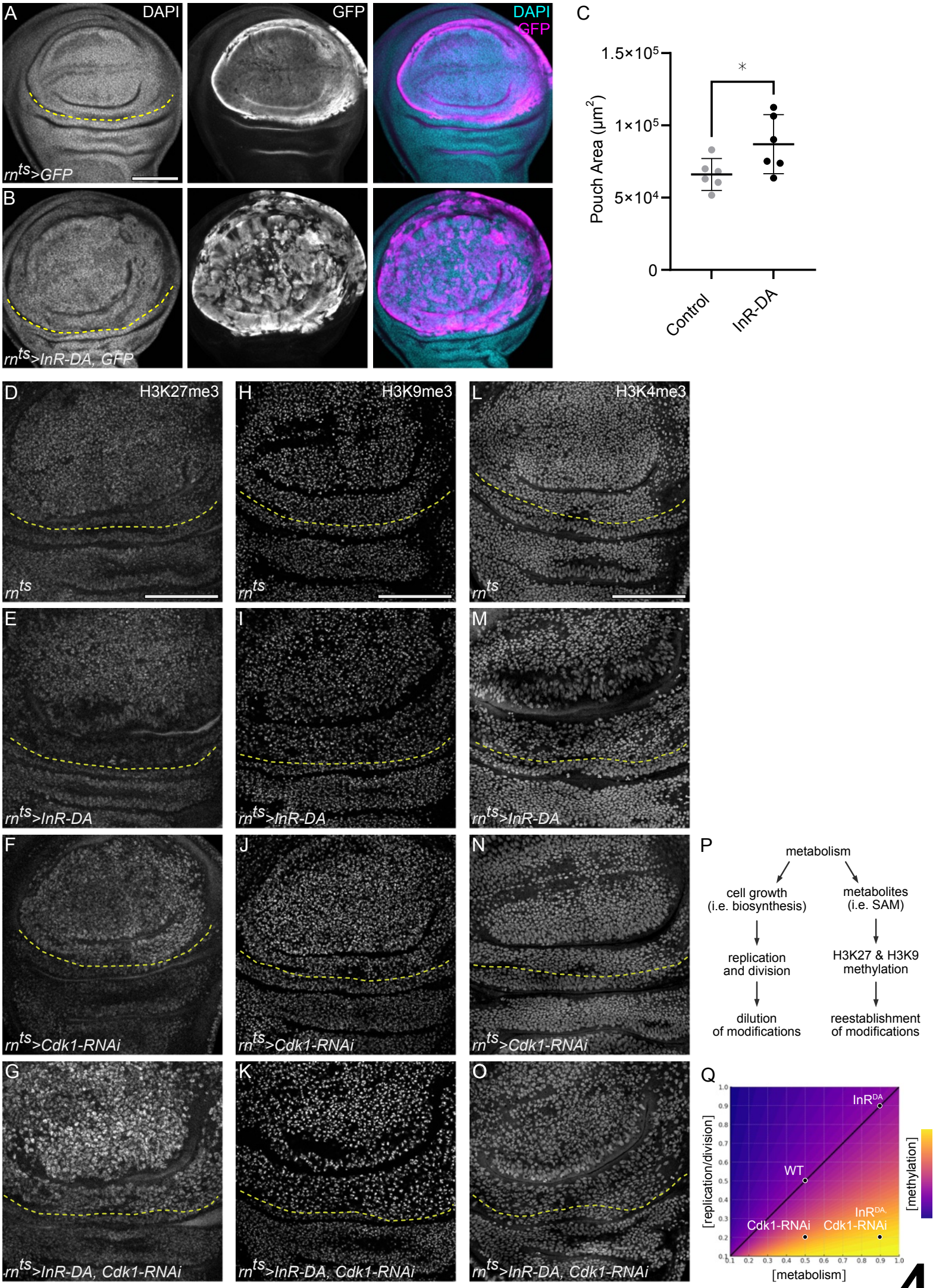
A
DAPI
GFP
DAPI
GFP
rn^ts>GFP
B
rn^ts>InR-DA, GFP
C
1.5×10^5
1×10^5
5×10^4
0
Pouch Area (μm^2)
*
Control
InR-DA
D
H3K27me3
rn^ts
E
rn^ts>InR-DA
F
rn^ts>Cdk1-RNAi
G
rn^ts>InR-DA, Cdk1-RNAi
H
H3K9me3
rn^ts
I
rn^ts>InR-DA
J
rn^ts>Cdk1-RNAi
K
rn^ts>InR-DA, Cdk1-RNAi
L
H3K4me3
rn^ts
M
rn^ts>InR-DA
N
rn^ts>Cdk1-RNAi
O
rn^ts>InR-DA, Cdk1-RNAi
P
metabolism
cell growth
(i.e. biosynthesis)
metabolites
(i.e. SAM)
replication
and division
H3K27 & H3K9
methylation
dilution
of modifications
reestablishment
of modifications
Q
InR^DA
WT
Cdk1-RNAi
InR^DA,
Cdk1-RNAi
[replication/division]
[metabolism]
[methylation]
4

Figure 4. Metabolic state sets the rate of H3K27 and H3K9 methylation

A-B. Control wing disc expressing GFP (magenta) for 24 h in the wing pouch domain under the control of *rn-GAL4* **(A)**. Wing disc expressing GFP and a constitutively active Insulin receptor (*InR-DA*) under the same conditions **(B)**. GFP expression visualizes the enlarged wing pouch domain in *InR-DA* expressing discs.

C. Quantification of pouch size area in control and *InR-DA*-expressing discs. Mean and 95% CI is shown. Statistical significance was tested using two-tailed Unpaired t test, p value=0.0432. (control discs: n=6, *InR-DA*-expressing discs: n=6).

D-G. Immunostaining for H3K27me3 in control **(D)**, *InR-DA*-expressing **(E)**, *Cdk1-RNAi*-expressing **(F)** and *InR-DA, Cdk1-RNAi*-coexpressing **(G)** discs.

H-K. Immunostaining for H3K9me3 in control **(H)**, *InR-DA*-expressing **(I)**, *Cdk1-RNAi*-expressing **(J)** and *InR-DA, Cdk1-RNAi*-coexpressing **(K)** discs.

L-O. Immunostaining for H3K4me3 in control **(L)**, *InR-DA*-expressing **(M)**, *Cdk1-RNAi*-expressing **(N)** and *InR-DA, Cdk1-RNAi*-coexpressing **(O)** discs. Expression was induced for 24 h in the wing pouch using *rn-GAL4*. Yellow dashed lines indicate the boundary between the wing pouch and hinge regions. The area above the line corresponds to the *rn-GAL4* expression domain, while the area below represents wild-type cells.

P. Illustration of the dual role of metabolism in regulating histone methylation levels. Metabolism contributes to the dilution of histone PTMs by accelerating the cell cycle, thereby increasing the frequency of DNA replication events. Simultaneously, it supports the re-establishment of these PTMs by supplying essential precursors and cofactors required for methyltransferase activity.

Q. Hypothetical model depicting the relationship between histone methylation levels, metabolic rate, and cell division rate. When metabolic activity and cell division are proportionally coupled (black diagonal), histone methylation levels are maintained at stable levels. However, when metabolism outpaces cell division, methylation accumulates.

Discs were stained with DAPI to visualize nuclei.
Sum projections of multiple confocal sections are shown in **A-B.**
Maximum projections of multiple confocal sections are shown in **D-K.**
Scale bars: 100 µm.

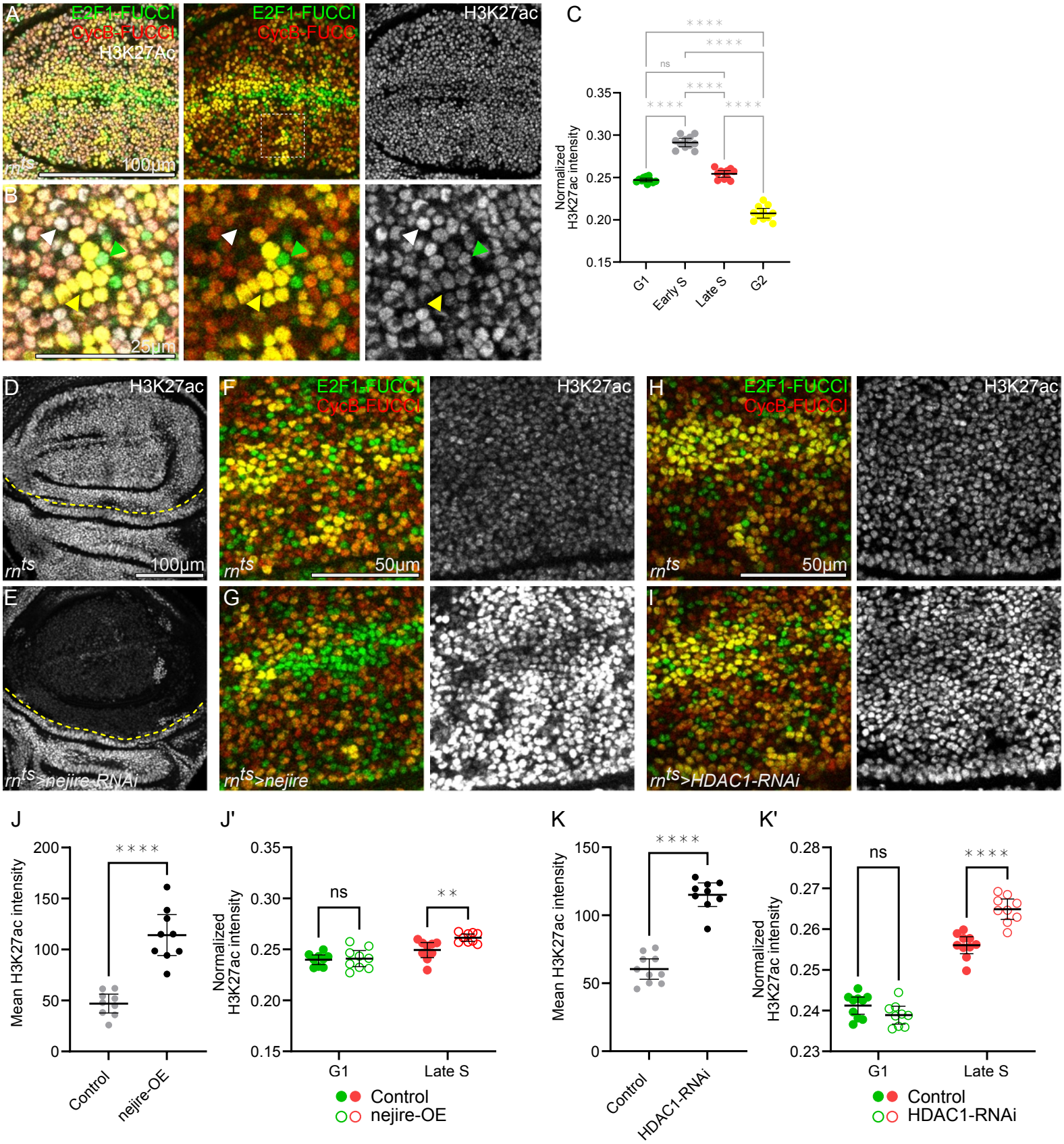
A
E2F1-FUCCI
CycB-FUCCI
H3K27Ac
rn^ts
100µm
H3K27ac
B
25µm
C
Normalized H3K27ac intensity
0.35
0.30
0.25
0.20
0.15
G1
Early S
Late S
G2
ns
D
H3K27ac
rn^ts
100µm
E
rn^ts>nejire-RNAi
F
E2F1-FUCCI
CycB-FUCCI
rn^ts
50µm
H3K27ac
G
rn^ts>nejire
H
E2F1-FUCCI
CycB-FUCCI
rn^ts
50µm
H3K27ac
I
rn^ts>HDAC1-RNAi
J
Mean H3K27ac intensity
200
150
100
50
0
Control
nejire-OE
J'
Normalized H3K27ac intensity
0.35
0.30
0.25
0.20
0.15
ns
G1
Late S
Control
nejire-OE
K
Mean H3K27ac intensity
150
100
50
0
Control
HDAC1-RNAi
K'
Normalized H3K27ac intensity
0.28
0.27
0.26
0.25
0.24
0.23
ns
G1
Late S
Control
HDAC1-RNAi

1135 **Figure 5. CBP/nejire-mediated H3K27 acetylation peaks during S phase**

1136

1137 **A-B.** Immunostaining for H3K27ac in a control disc expressing the FUCCI reporters *GFP-E2F1*$^{1-230}$ (green)
1138 and *mRFP-NLS-CycB*$^{1-266}$ (red) to visualize cell cycle phases **(A).** Magnified region in **(B)** is demarcated by a
1139 white dashed square in **(A).**

1140

1141 **C.** Quantification of normalized H3K27ac intensity level in different cell cycle phases in the pouch region
1142 of control discs. Normalization was performed against the average fluorescence intensity across all cell
1143 cycle phases. Mean and 95% CI is shown. Statistical significance was tested using Repeated Measures
1144 One-Way ANOVA followed by Tukey's post-hoc test for multiple comparison (n=11 discs). Adjusted
1145 $p<0.0001$ for G1 vs. Early S; $p=0.0838$ for G1 vs. Late S; $p<0.0001$ for G1 vs. G2; $p<0.0001$ for Early S vs.
1146 Late S; $p<0.0001$ for Early S vs G2 and $p<0.0001$ for Late S vs G2.

1147

1148 **D-E.** Immunostaining for H3K27ac in control **(D)** and *nejire-RNAi*-expressing **(E)** discs. Expression was
1149 induced for 24 h in the wing pouch using *rn-GAL4*. Yellow dashed lines indicate the boundary between the
1150 wing pouch and hinge regions.

1151

1152 **F-G.** Immunostaining for H3K27ac in control **(F)** and *nejire*-expressing **(G)** discs also expressing the FUCCI
1153 reporters *GFP-E2F1*$^{1-230}$ (green) and *mRFP-NLS-CycB*$^{1-266}$ (red) to visualize cell cycle phases. Expression of
1154 *nejire* was induced for 24 h in the wing pouch using *rn-GAL4*.

1155

1156 **H-I.** Immunostaining for H3K27ac in control **(H)** and *HDAC1-RNAi*-expressing **(I)** discs also expressing the
1157 FUCCI reporters *GFP-E2F1*$^{1-230}$ (green) and *mRFP-NLS-CycB*$^{1-266}$ (red) to visualize cell cycle phases.
1158 Expression of *HDAC1-RNAi* was induced for 24 h in the wing pouch using *rn-GAL4*.

1159

1160 **J.** Quantification of mean H3K27ac intensity in the pouch region of control or *nejire*-expressing discs.
1161 Expression was induced for 24 h in the wing pouch using *rn-GAL4*. Mean and 95% CI is shown. Statistical
1162 significance was tested using two-tailed Welch's t test, p value<0.0001. (control discs: n=9, *nejire*-
1163 expressing discs: n=9).

1164

1165 **J'.** Quantification of normalized H3K27ac in G1 phase and Late S phase in the pouch region of control or
1166 *nejire*-expressing discs. Expression was induced for 24 h in the wing pouch using *rn-GAL4*. Mean and 95%
1167 CI is shown. Statistical significance was tested using Repeated Measures Two-Way ANOVA followed by
1168 with Šidák's post hoc test for multiple comparisons (control discs: n=9, *nejire*-expressing discs: n=9).
1169 Adjusted p= 0.9482 for Control G1 vs nejire-OE G1; p=0.0064 for Control Late S vs nejire-OE Late S.

1170

1171 **K.** Quantification of mean H3K27ac intensity in the pouch region of control or *HDAC1-RNAi*-expressing
1172 discs. Expression was induced for 24 h in the wing pouch using *rn-GAL4*. Mean and 95% CI is shown.

Statistical significance was tested using two-tailed Mann-Whitney test, p value<0.0001. (control discs: n=10, *HDAC1-RNAi*-expressing discs: n=9).

K'. Quantification of normalized H3K27ac intensity level in G1 and Late S phases in the pouch region of control or *HDAC1-RNAi*-expressing discs. Expression was induced for 24 h in the wing pouch using *rn-GAL4*. Mean and 95% CI is shown. Statistical significance was tested using Repeated Measures Two-Way ANOVA followed by with Šidák's post hoc test for multiple comparisons (control discs: n=10, *HDAC1-RNAi*-expressing discs: n=9). Adjusted p= 0.1907 for Control G1 vs HDAC1-RNAi G1; p<0.0001 for Control Late S vs HDAC1-RNAi Late S.

Fluorescence intensities are reported as arbitrary units.

Sum projections of multiple confocal sections are shown in **D-E.**

Scale bars: 100 μm in **A** and **D-E**; 50 μm in **F-G** and **H-I**; 25 μm in **B**.

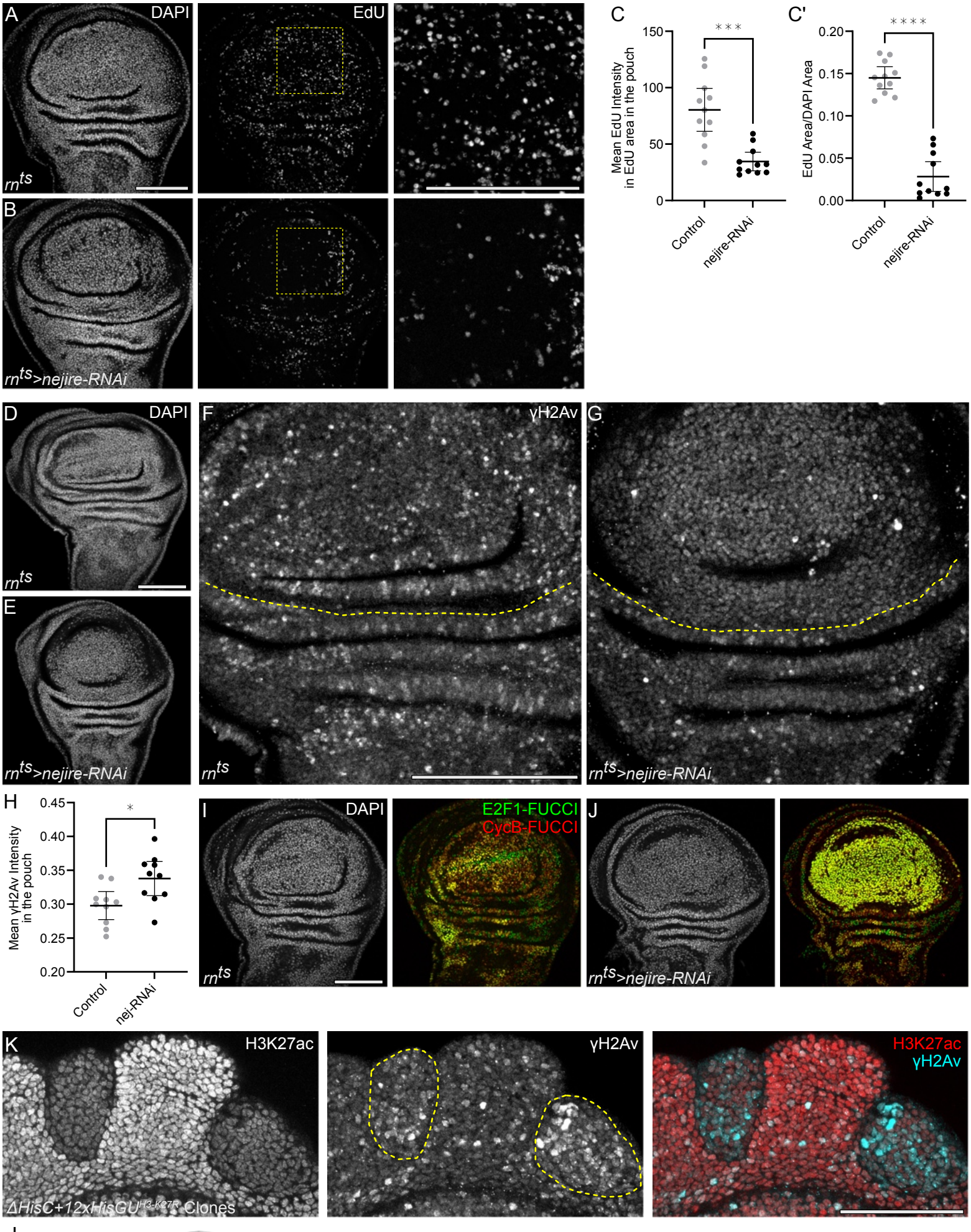
A
DAPI
EdU
rn^ts
B
rn^ts>nejire-RNAi
C
Mean EdU Intensity in EdU area in the pouch
150
100
50
0
***
Control
nejire-RNAi
C'
EdU Area/DAPI Area
0.20
0.15
0.10
0.05
0.00
****
Control
nejire-RNAi
D
DAPI
rn^ts
E
rn^ts>nejire-RNAi
F
γH2Av
rn^ts
G
rn^ts>nejire-RNAi
H
Mean γH2Av Intensity in the pouch
0.45
0.40
0.35
0.30
0.25
0.20
*
Control
nej-RNAi
I
DAPI
rn^ts
E2F1-FUCCI
CycB-FUCCI
J
rn^ts>nejire-RNAi
K
H3K27ac
ΔHisC+12xHisGU^H3-K27R Clones
γH2Av
H3K27ac
γH2Av
L
G1
S
G2
M
CBP/nej
H3K27ac
HDAC1
replication stress

Figure 6. CBP/Nejire activity and H3K27 acetylation prevent replication stress during S phase

A-B. EdU incorporation to visualize DNA replication in the pouch region of control **(A)** and *nejire-RNAi*-expressing **(B)** discs. Dashed yellow squares demarcate magnified regions shown in **(A', B').** Expression was induced for 24 h in the wing pouch using *rn-GAL4*.

C. Quantification of mean EdU intensity per EdU area in the pouch region of control and *nejire-RNAi*-expressing discs, serving as a proxy speed of DNA replication. Mean and 95% CI are shown. Statistical significance was tested using two-tailed Mann Whitney test, p value=0.0001 (control discs: n=11, *nejire-RNAi*-expressing discs: n=11).

C'. Quantification of EdU area per DAPI area in the pouch region of control and *nejire-RNAi*-expressing discs, serving as a proxy number of cells undergoing DNA replication. Mean and 95% CI are shown. Statistical significance was tested using two-tailed Mann Whitney test, p value<0.0001 (control discs: n=11, *nejire-RNAi*-expressing discs: n=11).

D-G. Immunostaining for γH2Av in control **(F)** and *nejire-RNAi*-expressing **(G)** discs. Expression was induced for 24 h in the wing pouch using *rn-GAL4*. γH2Av serves as a marker of DNA double strand breaks. DAPI staining was used to visualize the nuclei in control **(D)** and *nejire-RNAi*-expressing **(E)** discs. The *rn-GAL4* expression domain is represented by the tissue above the yellow line (rn^{ts}>). The tissue below the yellow line represents wild type tissues of the hinge.

H. Quantification of mean γH2Av intensity in the pouch region of control or *nejire-RNAi*-expressing discs. Mean and 95% CI are shown. Statistical significance was tested using two-tailed Unpaired t test, p value=0.0126 (control discs: n=10, *nejire-RNAi*-expressing discs: n=10).

K. Immunostaining for H3K27ac (red) and γH2Av (cyan) in wing imaginal discs with clones of *ΔHisC* mutant clones deleting the histone cluster and rescued by a *12×His-GU*$^{H3\text{-}K27R}$ transgene.

L. Illustration of the role of CBP/nej and HDAC1 in modulating levels of H3K27ac during S-phase to prevent replication stress

Discs were stained with DAPI to visualize nuclei.
Fluorescence intensities are reported as arbitrary units.
Sum projections of multiple confocal sections are shown in **A-B** and **D-G.**
Maximum projections of multiple confocal sections are shown in **K.**
Scale bars: 100 μm in **A-B**, **D-G**, **I-J** and **K.**

SUPPLEMENTARY FIGURES

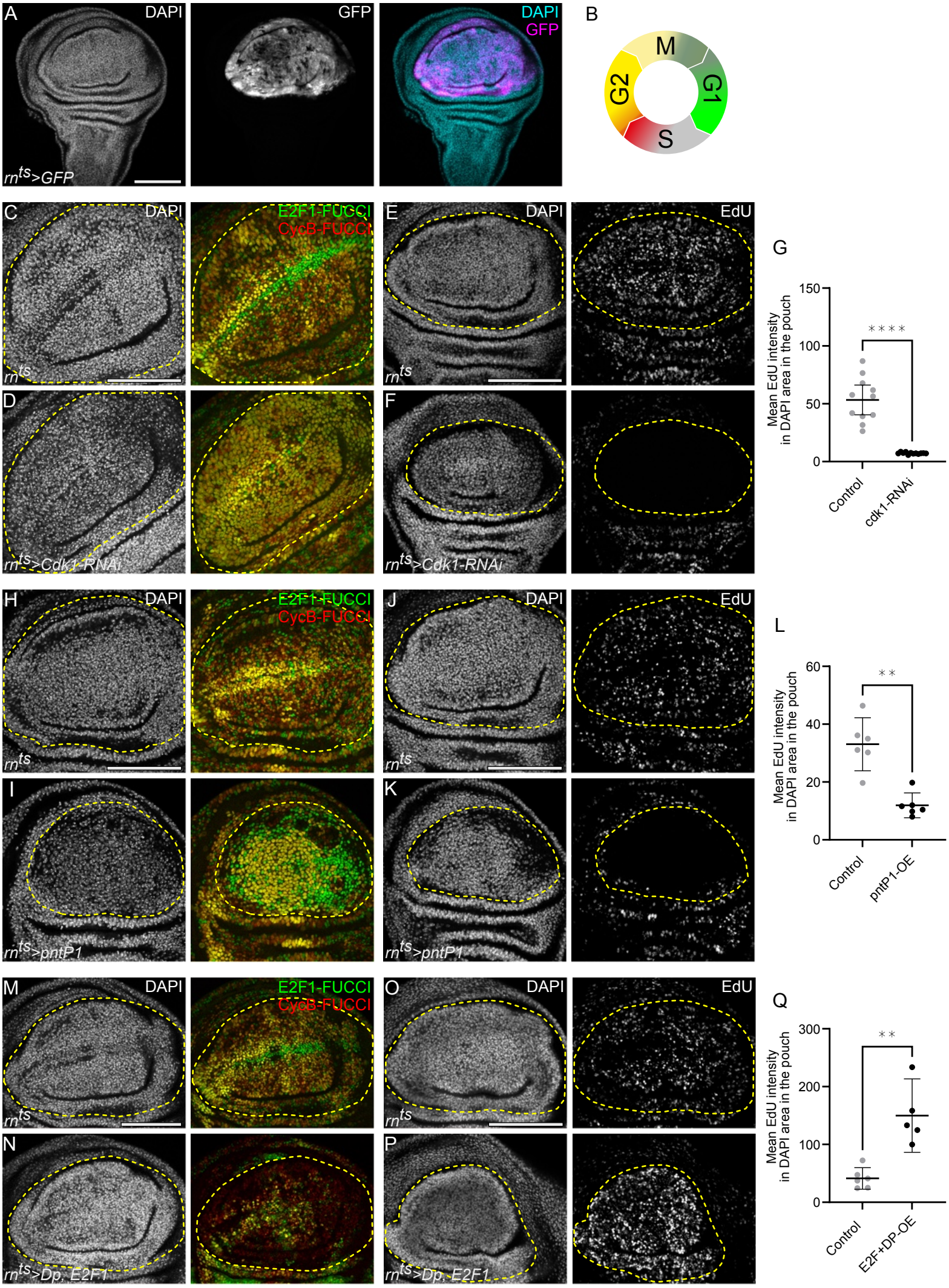
A
DAPI
GFP
DAPI
GFP
rn^ts>GFP
B
M
G1
S
G2
C
DAPI
E2F1-FUCCI
CycB-FUCCI
rn^ts
D
rn^ts>Cdk1-RNAi
E
DAPI
EdU
rn^ts
F
rn^ts>Cdk1-RNAi
G
Mean EdU intensity in DAPI area in the pouch
150
100
50
0
****
Control
cdk1-RNAi
H
DAPI
E2F1-FUCCI
CycB-FUCCI
rn^ts
I
rn^ts>pntP1
J
DAPI
EdU
rn^ts
K
rn^ts>pntP1
L
Mean EdU intensity in DAPI area in the pouch
60
40
20
0
**
Control
pntP1-OE
M
DAPI
E2F1-FUCCI
CycB-FUCCI
rn^ts
N
rn^ts>Dp, E2F1
O
DAPI
EdU
rn^ts
P
rn^ts>Dp, E2F1
Q
Mean EdU intensity in DAPI area in the pouch
300
200
100
0
**
Control
E2F+DP-OE

S1.1

Figure S1.1. Cell cycle manipulation models for assessing histone modification dynamics

A. A control wing disc after 24 h of *UAS-GFP*-expression in the pouch, under the control of the *rn-GAL4* (*rotund-GAL4*) driver. GFP-expression visualizes the tissue domain subject to manipulation throughout this study (magenta).

B. Schematic representation of the Fly-FUCCI cell cycle reporter system, utilizing the degradable *GFP-E2F1*$^{1-230}$ (green) and *mRFP-NLS-CycB*$^{1-266}$ (red) as sensors to visualize cell cycle phases. Individual fluorophore expression indicates cells in G1 or late S-phase, respectively. Combined expression of both GFP and RFP labels cells is observed in early and late G2. Cells in late mitosis and early S-phase lack expression of either GFP or RFP. Cells in early S-phase are specifically detected by EdU incorporation (Crucianelli et al., 2022; Zielke et al., 2014). Cells in mitosis are positioned in very apical positions of the tissue and are not represented in our study.

C-G. Cell cycle dynamics in control discs **(C, E)** and discs expressing *Cdk1-RNAi* for 24 h under the control of *rn-GAL4* **(D, F)**. FUCCI reporters *GFP-E2F1*$^{1-230}$ (green) and *mRFP-NLS-CycB*$^{1-266}$ (red) were used to visualize cell cycle phases **(C, D)** and EdU incorporation was used to detect DNA replication in S-phase cells **(E, F).** Cdk1 knockdown in the wing pouch domain leads to a cell cycle phase shift toward G2 phase **(D)**, and a corresponding loss of EdU incorporation **(F)** combined demonstrating a pronounced arrest in G2. **(G)** Quantification of mean EdU intensity per DAPI area in the pouch region of control and *Cdk1-RNAi*-expressing discs, serving as a proxy for relative DNA replication activity. Mean and 95% CI are shown. Statistical significance was tested using two-tailed Welch's test, p value <0.0001 (control discs: n=11, *Cdk1-RNAi*-expressing discs: n=12).

H-L. Cell cycle dynamics in control discs **(H, J)** and discs expressing *pntP1* **(I, K)** for 24 h under the control of *rn-GAL4*. FUCCI reporters *GFP-E2F1*$^{1-230}$ (green) and *mRFP-NLS-CycB*$^{1-266}$ (red) were used to visualize cell cycle phases **(H, I)** and EdU incorporation was used to detect DNA replication in S-phase cells **(J, K).** Pointed-P1 overexpression in the wing pouch domain leads to a cell cycle phase shift towards either the G1 or the G2 phase **(I)**, correlating with a loss of EdU incorporation **(K)**. Combined, this demonstrates a pronounced arrest in either G1 or G2. Mechanistically, the choice for either cell cycle phase is not known. **(L)** Quantification of mean EdU intensity per DAPI area in the pouch region of control and *pntP1*-expressing discs, serving as a proxy for relative DNA replication activity. Mean and 95% CI is shown. Statistical significance was tested using two-tailed Mann-Whitney test, p value=0.0043 (control discs: n=6, *pntP1*-expressing discs: n=6).

M-Q. Cell cycle dynamics in control discs **(M, O)** and discs expressing *Dp, E2F1* **(N, P)** for 24 h under the control of *rn-GAL4*. FUCCI reporters *GFP-E2F1*$^{1-230}$ (green) and *mRFP-NLS-CycB*$^{1-266}$ (red) were used to visualize cell cycle phases **(M, N)** and EdU incorporation was used to detect DNA replication in S-phase

cells **(O,P).** dDp and dE2F1 co-expression in the wing pouch domain reduces the number of cells in either G1 or G2 **(N)**, and an increase in S-phase cells as well as an elevation of EdU incorporation **(P)** in the wing pouch region, confirming frequent entry and rapid progression through the cell cycle. **(Q)** Quantification of mean EdU intensity per DAPI area in the pouch region of control and *Dp, E2F1*-coexpressing discs, serving as a proxy for relative DNA replication activity. Mean and 95% CI is shown. Statistical significance was tested using two-tailed Welch's t test, p value=0.0069 (control discs: n=6, *Dp, E2F1*-expressing discs: n=5).

Discs were stained with DAPI to visualize nuclei.

Fluorescence intensities are reported as arbitrary units.

Yellow dashed lines represent the pouch region of wing discs.

Sum projections of multiple confocal sections are shown in **A, E-F, J-K, M-N** and **O-P.**

Maximum projections of multiple confocal sections are shown in **C-D** and **H-I.**

Scale bars: 100 μm.

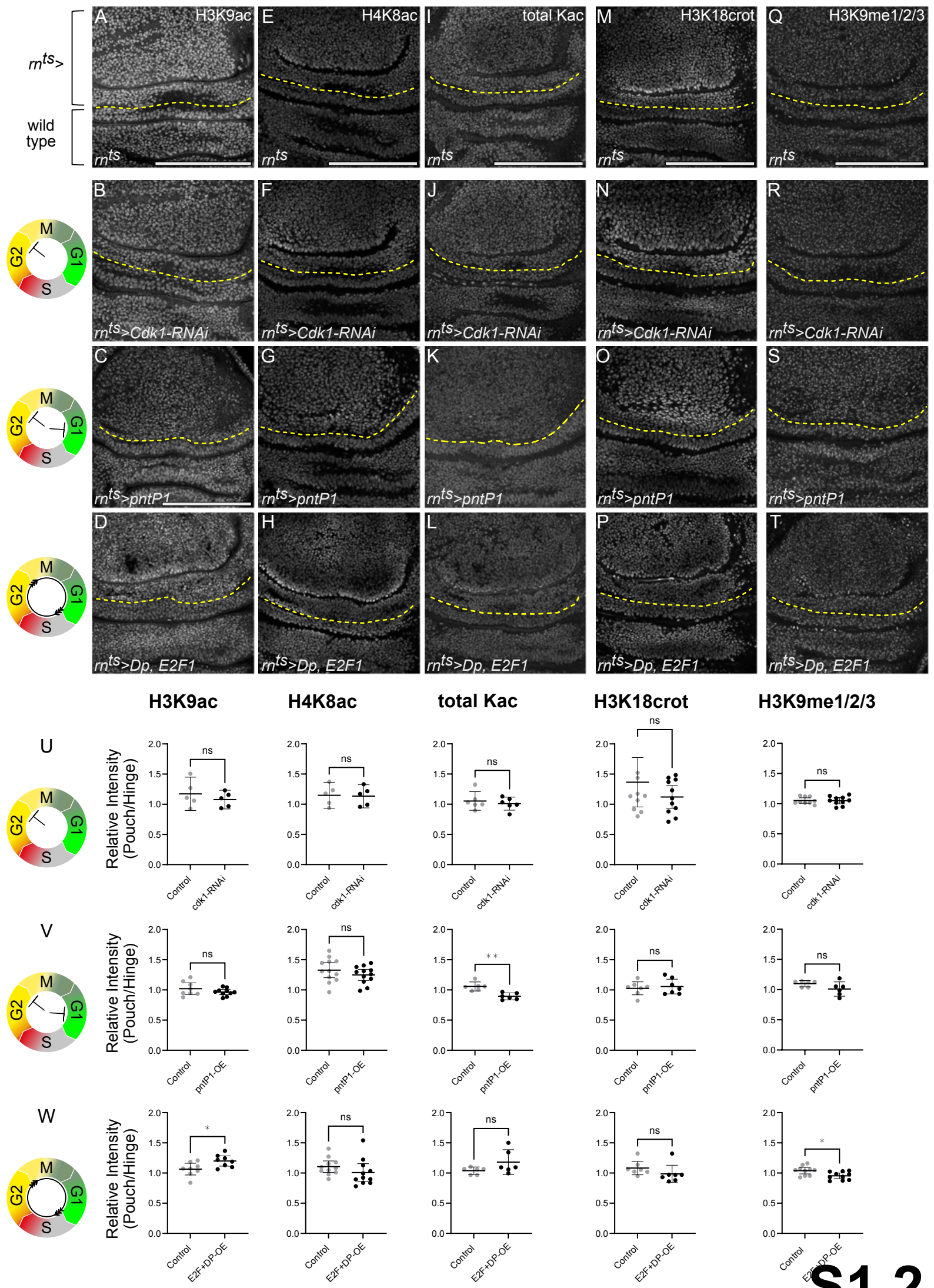
A H3K9ac
E H4K8ac
I total Kac
M H3K18crot
Q H3K9me1/2/3
rnts>
wild type
rnts
B
F
J
N
R
rnts>Cdk1-RNAi
C
G
K
O
S
rnts>pntP1
D
H
L
P
T
rnts>Dp, E2F1
M
G1
S
G2
H3K9ac
H4K8ac
total Kac
H3K18crot
H3K9me1/2/3
U
V
W
Relative Intensity (Pouch/Hinge)
2.0
1.5
1.0
0.5
0.0
ns
**
*
Control
cdk1-RNAi
pntP1-OE
E2F+DP-OE
S1.2

Figure S1.2. Histone modifications are largely insensitive to cell cycle manipulations

A-D. Immunostaining for H3K9ac in control **(A)**, *Cdk1-RNAi*-expressing **(B)**, *pntP1*-expressing **(C)** and *Dp, E2F1*-expressing **(D)** discs. Expression was induced for 24 h in the wing pouch using *rn-GAL4*. The *rn-GAL4* expression pouch domain is represented by the tissue above the yellow line (rn^{ts}>). The tissue below the yellow line represents wild type tissues of the hinge. Icons represent the experimentally verified FUCCI cell cycle status (see **Fig S1.1**) in each condition: G2-phase arrest in *Cdk1-RNAi*-expressing discs **(B)**, combined G1 and G2-phase arrest in *pntP1*-expressing discs **(C)**, and cell cycle acceleration in *Dp, E2F1*-coexpressing discs **(D)**.

E-H. Immunostaining for H4K8ac in control **(E)**, *Cdk1-RNAi*-expressing **(F)**, *pntP1*-expressing **(G)** and *Dp, E2F1*-coexpressing **(H)** discs.

I-L. Immunostaining for total acetylated lysines in control **(I)**, *Cdk1-RNAi*-expressing **(J)**, *pntP1*-expressing **(K)** and *Dp, E2F1*-coexpressing **(L)** discs.

M-P. Immunostaining for H3K18crotonylation in control **(M)**, *Cdk1-RNAi*-expressing **(N)**, *pntP1*-expressing **(O)** and *Dp, E2F1*-coexpressing **(P)** discs.

Q-T. Immunostaining for total H3K9me1/2/3 methylation in control **(I)**, *Cdk1-RNAi*-expressing **(J)**, *pntP1*-expressing **(K)** and *Dp, E2F1*-coexpressing **(L)** discs.

U. Quantification of relative signal intensities for H3K9ac, H4K8ac, total acetylated lysine, H3K18crotonylation, and H3K9me1/2/3, presented as pouch-to-hinge ratios (rn^{ts}-to-wild-type-cell ratio) in *Cdk1-RNAi*-expressing discs. Mean and 95% CI is shown. Statistical significance was tested using two-tailed Unpaired t test, p value= 0.4268 for H3K9ac (control discs: n=5, *Cdk1-RNAi*-expressing discs: n=5); two-tailed Unpaired t test, p value=0.8936 for H4K8ac (control discs: n=5, *Cdk1-RNAi*-expressing discs: n=5); two-tailed Unpaired t test, p value=0.5553 for total acetylated lysines (control discs: n=6, *Cdk1-RNAi*-expressing discs: n=6); two-tailed Mann-Whitney test, p value=0.4779 for H3K18crot (control discs: n=11, *Cdk1-RNAi*-expressing discs: n=11); two-tailed Unpaired t test, p value=0.9619 for H3K9me1/2/3 (control discs: n=9, *Cdk1-RNAi*-expressing discs: n=10).

V. Quantification of relative signal intensities for H3K9ac, H4K8ac, total acetylated lysine, H3K18crotonylation, and H3K9me1/2/3, presented as pouch-to-hinge ratios (rn^{ts}-to-wild-type-cell ratio) in *pntP1*-expressing discs. Mean and 95% CI is shown. Statistical significance was tested using two-tailed Unpaired t test, p value= 0.1975 for H3K9ac (control discs: n=8, *pntP1*-expressing discs: n=10); two-tailed Unpaired t test, p value=0.2752 for H4K8ac (control discs: n=12, *pntP1*-expressing discs: n=12); two-tailed Unpaired t test, p value=0.0012 for total acetylated lysines (control discs: n=6, *pntP1*-expressing discs:

n=6); two-tailed Unpaired t test, p value=0.6621 for H3K18crot (control discs: n=7, *pntP1*-expressing discs: n=7); two-tailed Mann-Whitney test, p value=0.2403 for H3K9me1/2/3 (control discs: n=6, *pntP1*-expressing discs: n=6).

W. Quantification of relative signal intensities for H3K9ac, H4K8ac, total acetylated lysine, H3K18crotonylation, and H3K9me1/2/3, presented as pouch-to-hinge ratios (rn^{ts}-to-wild-type-cell ratio) in *Dp, E2F1*-coexpressing discs. Mean and 95% CI is shown. Statistical significance was tested using two-tailed Unpaired t test, p value= 0.0282 for H3K9ac (control discs: n=8, *Dp, E2F1*-coexpressing discs: n=8); two-tailed Mann-Whitney test, p value=0.0759 for H4K8ac (control discs: n=11, *Dp, E2F1*-coexpressing discs: n=11); two-tailed Mann-Whitney test, p value=0.2403 for total acetylated lysines (control discs: n=6, *Dp, E2F1*-coexpressing discs: n=6); two-tailed Mann-Whitney test, p value=0.0728 for H3K18crot (control discs: n=7, *Dp, E2F1*-coexpressing discs: n=7); two-tailed Unpaired t test, p value=0.0154 for H3K9me1/2/3 (control discs: n=10, *Dp, E2F1*-coexpressing discs: n=10).

Fluorescence intensities are reported as arbitrary units.
Sum projections of multiple confocal sections are shown in **C-T.**
Scale bars: 100 µm.
Please refer to **(Fig S1.3B)** for corresponding DAPI images of all discs shown.

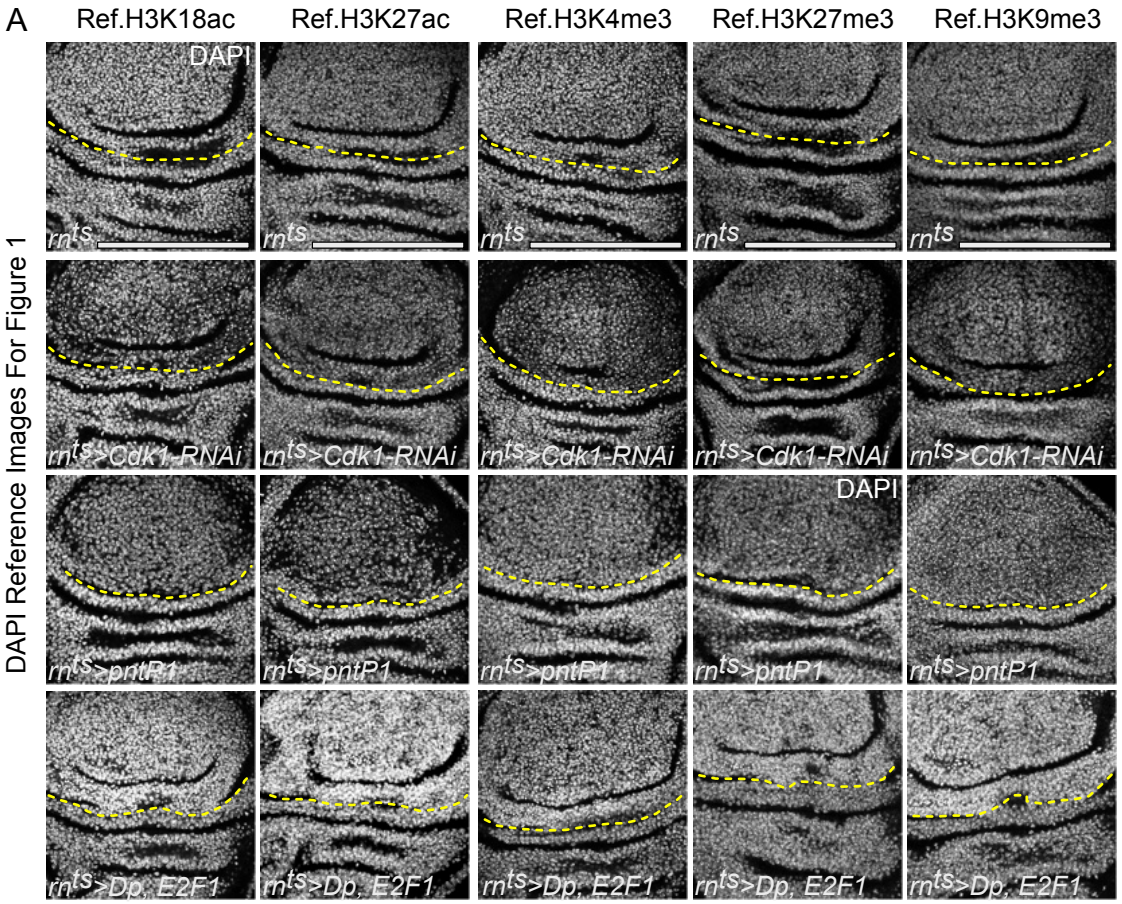
A
Ref.H3K18ac
Ref.H3K27ac
Ref.H3K4me3
Ref.H3K27me3
Ref.H3K9me3
DAPI
DAPI Reference Images For Figure 1
rn^ts
rn^ts>Cdk1-RNAi
rn^ts>pntP1
rn^ts>Dp, E2F1

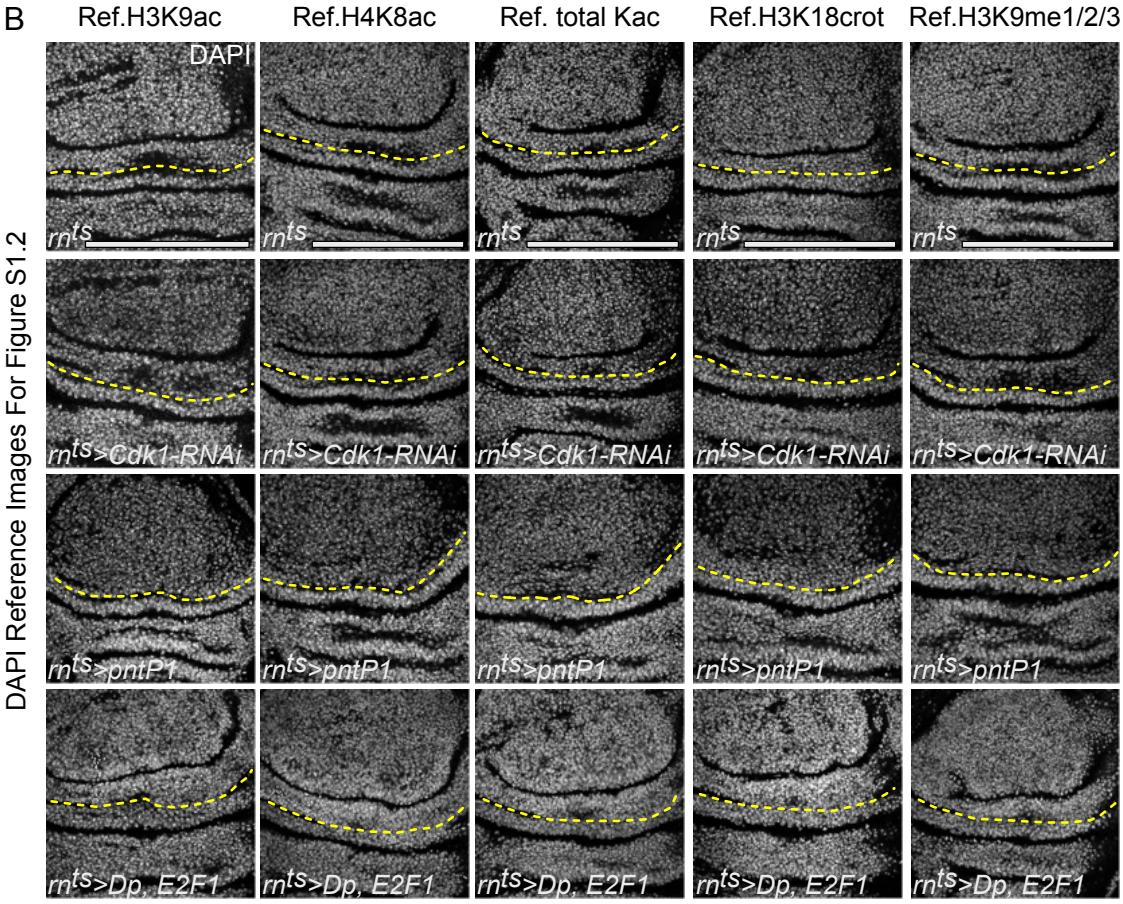
B
Ref.H3K9ac
Ref.H4K8ac
Ref. total Kac
Ref.H3K18crot
Ref.H3K9me1/2/3
DAPI
DAPI Reference Images For Figure S1.2
rn^ts
rn^ts>Cdk1-RNAi
rn^ts>pntP1
rn^ts>Dp, E2F1

S1.3

Figure S1.3 Corresponding DAPI images for Fig 1 and Fig S1.2

Representation of DAPI images matched to the images of histone modifications in control, *Cdk1-RNAi*-expressing, *pntP1*-expressing and *Dp, E2F1*-coexpressing wing discs shown in Fig 1 and Fig S1.2.

Discs were stained with DAPI to visualize nuclei.

Sum and max projections of multiple confocal sections are shown.

Scale bars: 100 μm.

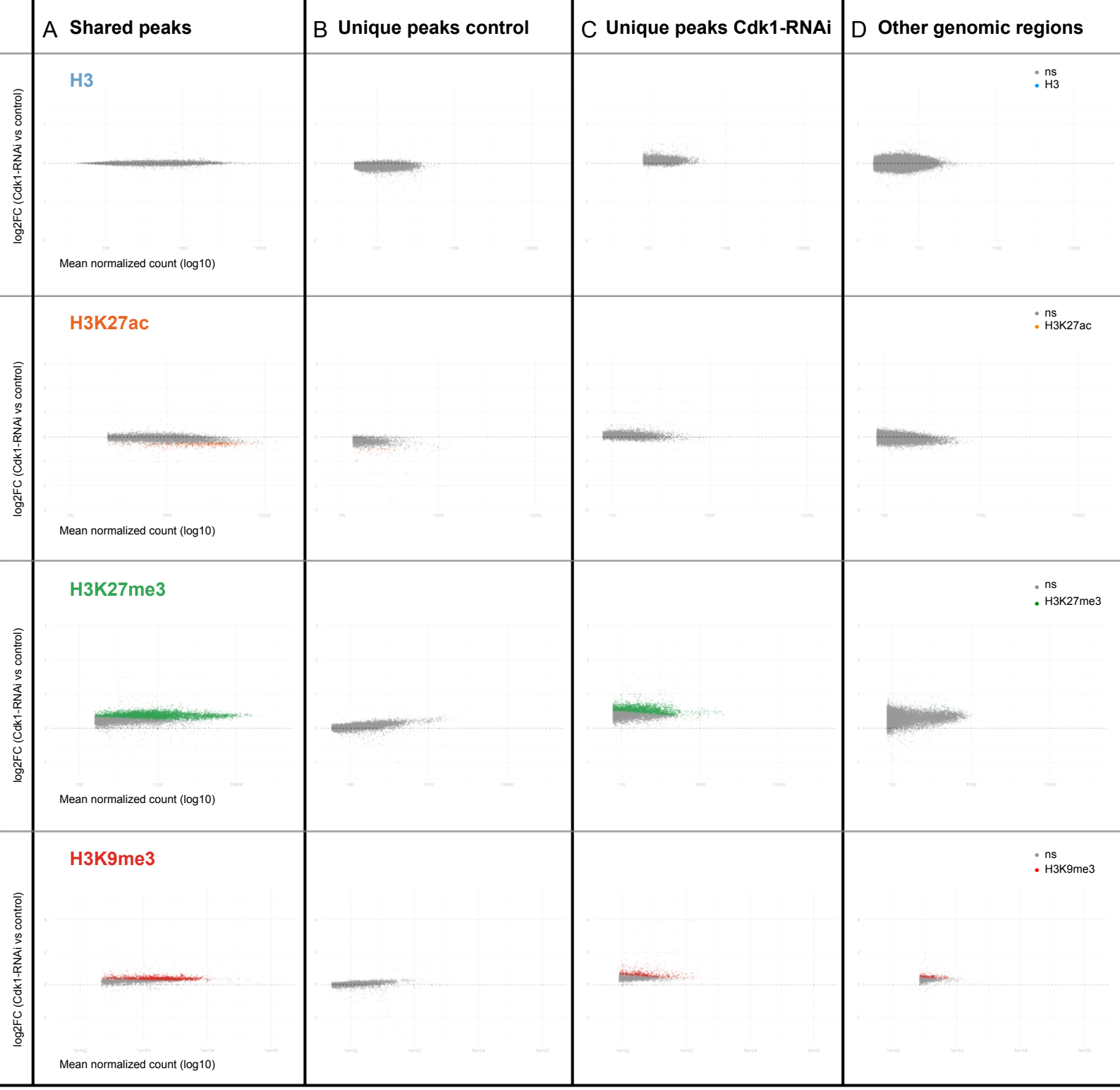
A Shared peaks
B Unique peaks control
C Unique peaks Cdk1-RNAi
D Other genomic regions
H3
H3K27ac
H3K27me3
H3K9me3
ns
log2FC (Cdk1-RNAi vs control)
Mean normalized count (log10)

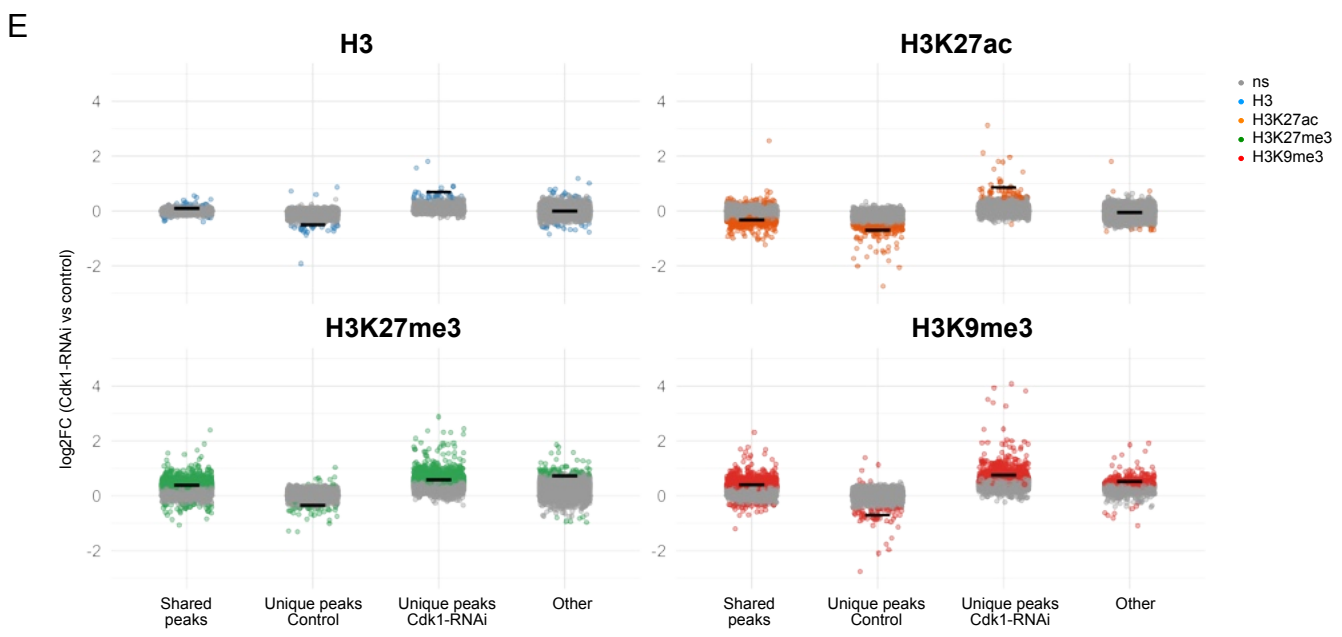
E
H3
H3K27ac
H3K27me3
H3K9me3
ns
log2FC (Cdk1-RNAi vs control)
Shared peaks
Unique peaks Control
Unique peaks Cdk1-RNAi
Other

S2.1

Figure S2.1. Comparative analysis of Histone H3 and H3K27ac, H3K27me3, and H3K9me3 histone modifications by CUT&Tag in control and Cdk1 RNAi- expressing discs

---

A-D. MA plots displaying differential enrichment of histone modifications analysed by by CUT&Tag for H3, H3K27ac, H3K27me3, and H3K9me3 (in rows). Each point represents a shared or unique genomic peak identified by our analysis in control and Cdk1-RNAi expressing discs (shared peaks **(A)**, unique peaks in control **(B)**, unique peaks in cdk1-RNAi **(C)**), or a 500 bp genomic fragment not called as any peak in our analysis (other genomic regions **(D)**). The x-axis displays the mean normalized read count on a log10 scale, representing an average signal intensity across samples or conditions. The y-axis displays the log2 fold change (log2 ratio of read counts) between the Cdk1-RNAi and control conditions, reflecting the magnitude and direction of differential enrichment. Peaks are color-coded by modification type: blue for H3, orange for H3K27ac, green for H3K27me3, and red for H3K9me3. Regions with an adjusted p-value<0.1 are colored accordingly, highlighting statistically significant differential peaks; non-significant peaks (ns, adjusted p-value ≥0.1) are shown in gray.

E. Each subplot depicts the distribution of log2 fold change values (Cdk1-RNAi compared to control) for genomic regions categorized as Shared (peaks detected in both conditions), Control-Unique (peaks specific to control), Cdk1-RNAi-Unique (peaks specific to Cdk1-RNAi expressing discs), and Other (genomic fragments of 500bp not included in any called peaks). The x-axis indicates these categorical groups, and the y-axis shows the log2 fold change of normalized counts between Cdk1-RNAi and control samples. Each point represents an individual genomic region, colored by histone mark: blue (H3), orange (H3K27ac), green (H3K27me3), and red (H3K9me3). Black horizontal bars indicate the mean log2 fold change within each group. Peaks are color-coded by modification type: blue for H3, orange for H3K27ac, green for H3K27me3, and red for H3K9me3. Regions with an adjusted p-value<0.1 are colored accordingly, highlighting statistically significant differential peaks; non-significant peaks (ns, adjusted p-value ≥0.1) are shown in gray.

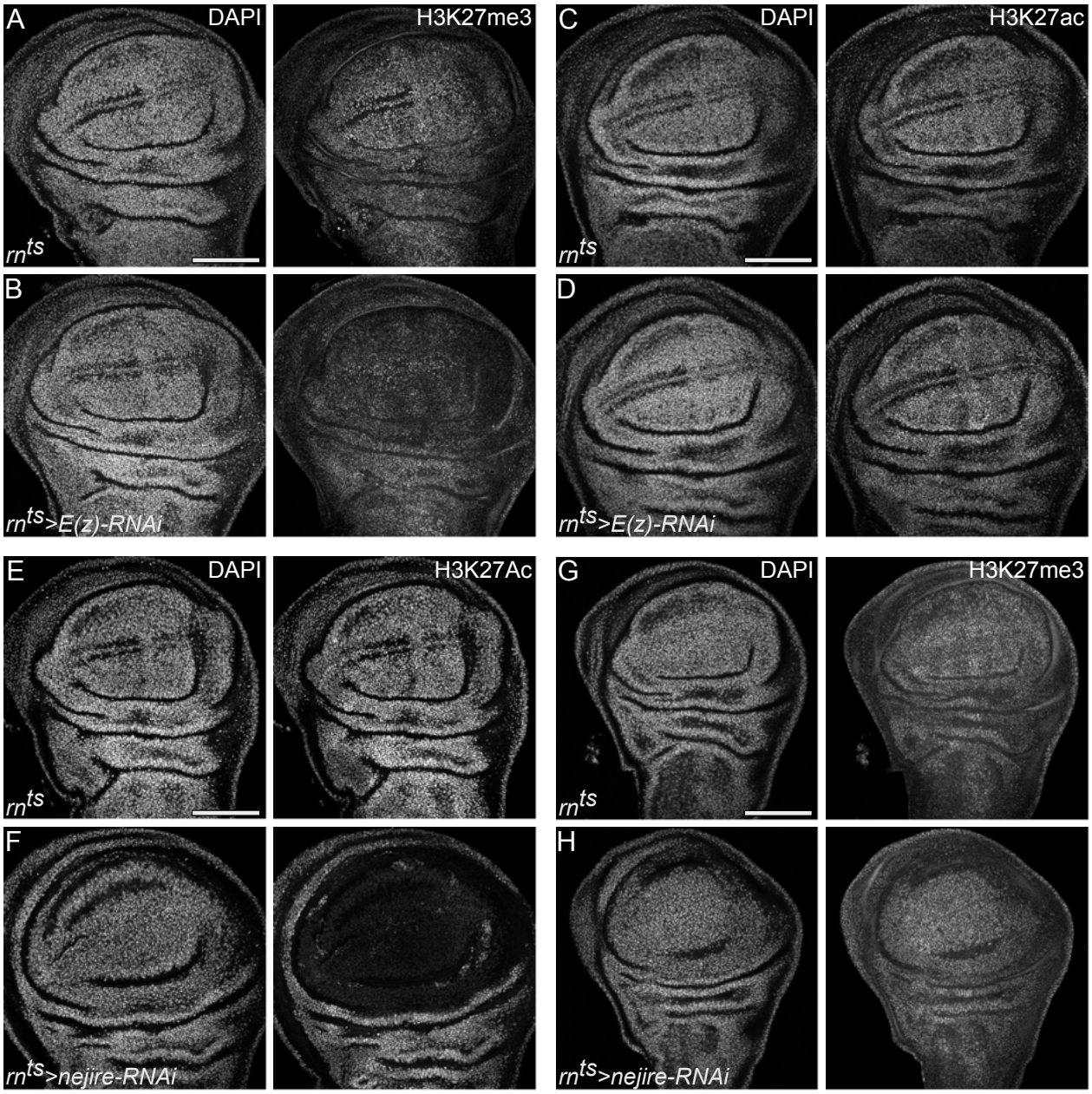
A
DAPI
H3K27me3
rn^ts
B
rn^ts>E(z)-RNAi
C
DAPI
H3K27ac
rn^ts
D
rn^ts>E(z)-RNAi
E
DAPI
H3K27Ac
rn^ts
F
rn^ts>nejire-RNAi
G
DAPI
H3K27me3
rn^ts
H
rn^ts>nejire-RNAi

S2.2

Figure S2.2. Cell cycle–dependent fluctuations of H3K27ac and H3K27me3 are not due to competitive residue occupancy

---

A-B. H3K27me3 staining in control **(A)** or *E(z)-RNAi*-expressing **(B)** discs. Knockdown of the H3K27me3 writer E(z) causes a reduction in H3K27me3 level in the pouch of the wing disc.

C-D. H3K27ac staining in control **(C)** or *E(z)-RNAi*-expressing **(D)** discs. Knockdown of the H3K27me writer E(z) causes no corresponding increase in H3K27ac level.

E-F. H3K27ac staining in control **(E)** and *nejire-RNAi*-expressing **(F)** discs. Knockdown of the H3K27ac writer CBP/nej causes a reduction of H3K27ac level in the pouch of the wing disc.

G-H. H3K27me3 staining in control **(G)** and *nejire-RNAi*-expressing **(H)** discs. Knockdown of the H3K27ac writer CBP/nej causes no corresponding increase in H3K27me3 level.

Discs were stained with DAPI to visualize nuclei.
Maximum projections of multiple confocal sections are shown in **A-B.**
Sum projections of multiple confocal sections are shown in **C-D, E-F** and **G-H.**
Scale bars: 100 μm.

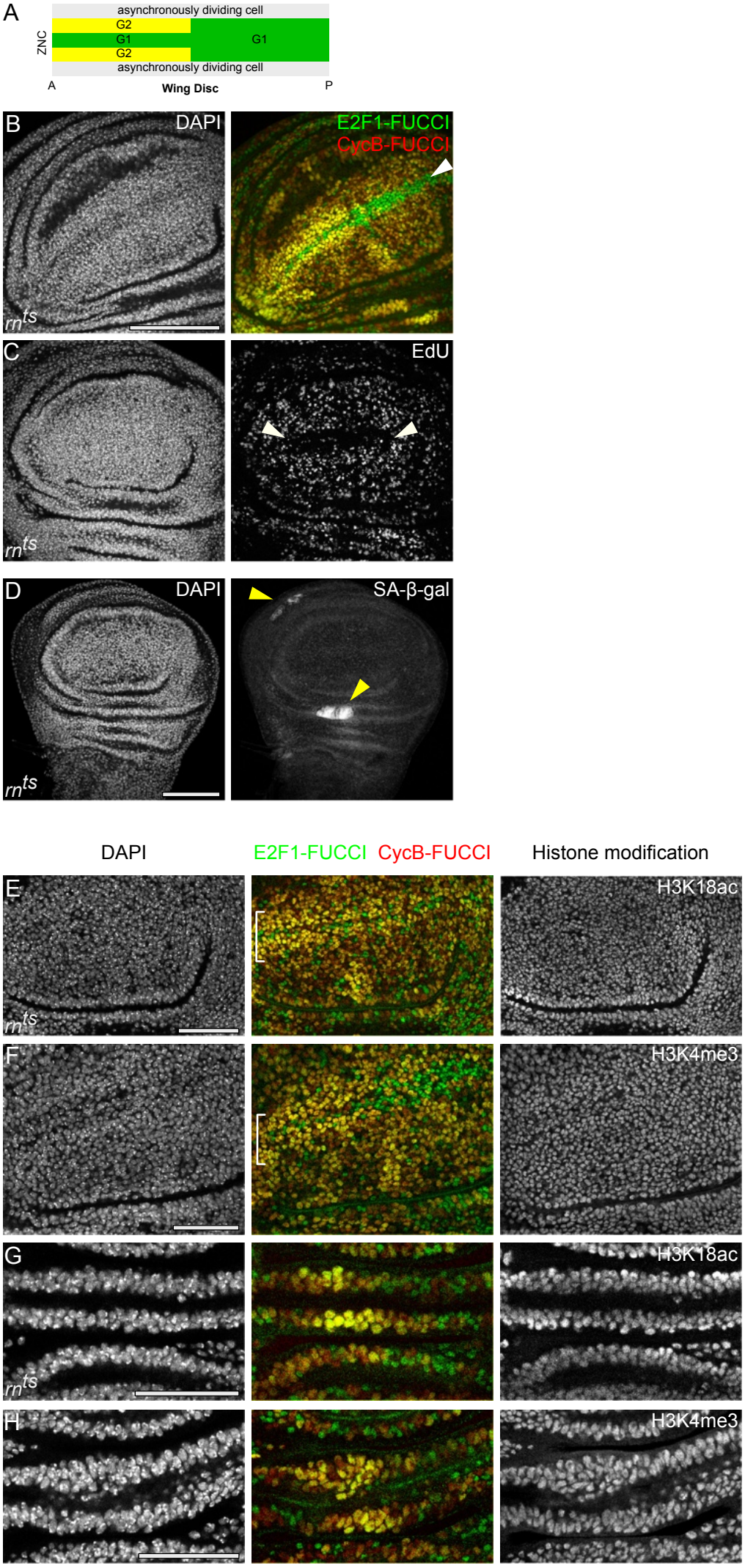
A
asynchronously dividing cell
G2
G1
G1
G2
asynchronously dividing cell
ZNC
A
Wing Disc
P
B
DAPI
E2F1-FUCCI
CycB-FUCCI
rn^ts
C
EdU
rn^ts
D
DAPI
SA-β-gal
rn^ts
DAPI
E2F1-FUCCI CycB-FUCCI
Histone modification
E
H3K18ac
rn^ts
F
H3K4me3
G
H3K18ac
rn^ts
H
H3K4me3

S3.1

Figure S3.1. Visualization of cell cycle-arrested cell populations and histone modifications in developing wing imaginal disc

---

A. Schematic representation of the zone of non-proliferation cells (ZNC) (adapted from (Johnston and Edgar, 1998)).

B-C. The Fly-FUCCI system and EdU incorporation assay were used to visualize the spatial pattern of cell cycle arrest within the ZNC. In the anterior ZNC, central margin cells arrest in G1 phase, while adjacent cells arrest in G2. Cells in the posterior ZNC uniformly arrest in G1. The entire ZNC region also lacks EdU incorporation, indicating absence of S-phase entry. White arrowheads indicate the ZNC.

D. Elevated SA-β-gal activity marks two clusters of cell cycle–arrested cells undergoing programmed senescence (indicated by yellow arrowheads) in developing wing discs.

E,F. Immunostaining for H3K18ac **(E)** and H3K4me3 **(F)** in the zone of non-proliferation cells (ZNC) of developing wing discs. Neither histone modification shows detectable changes in this region.

G,H. Immunostaining for H3K18ac **(G)** and H3K4me3 **(H)** in senescent cell populations of the hinge in developing wing discs. Neither histone modification shows detectable changes in this region.

Discs were stained with DAPI to visualize nuclei.
Maximum projection of multiple confocal sections is shown in **C.**
Sum projections of multiple confocal sections are shown in **A-B and D.**
Scale bars: 100 μm in **B-D**; 50 μm in **E-H.**

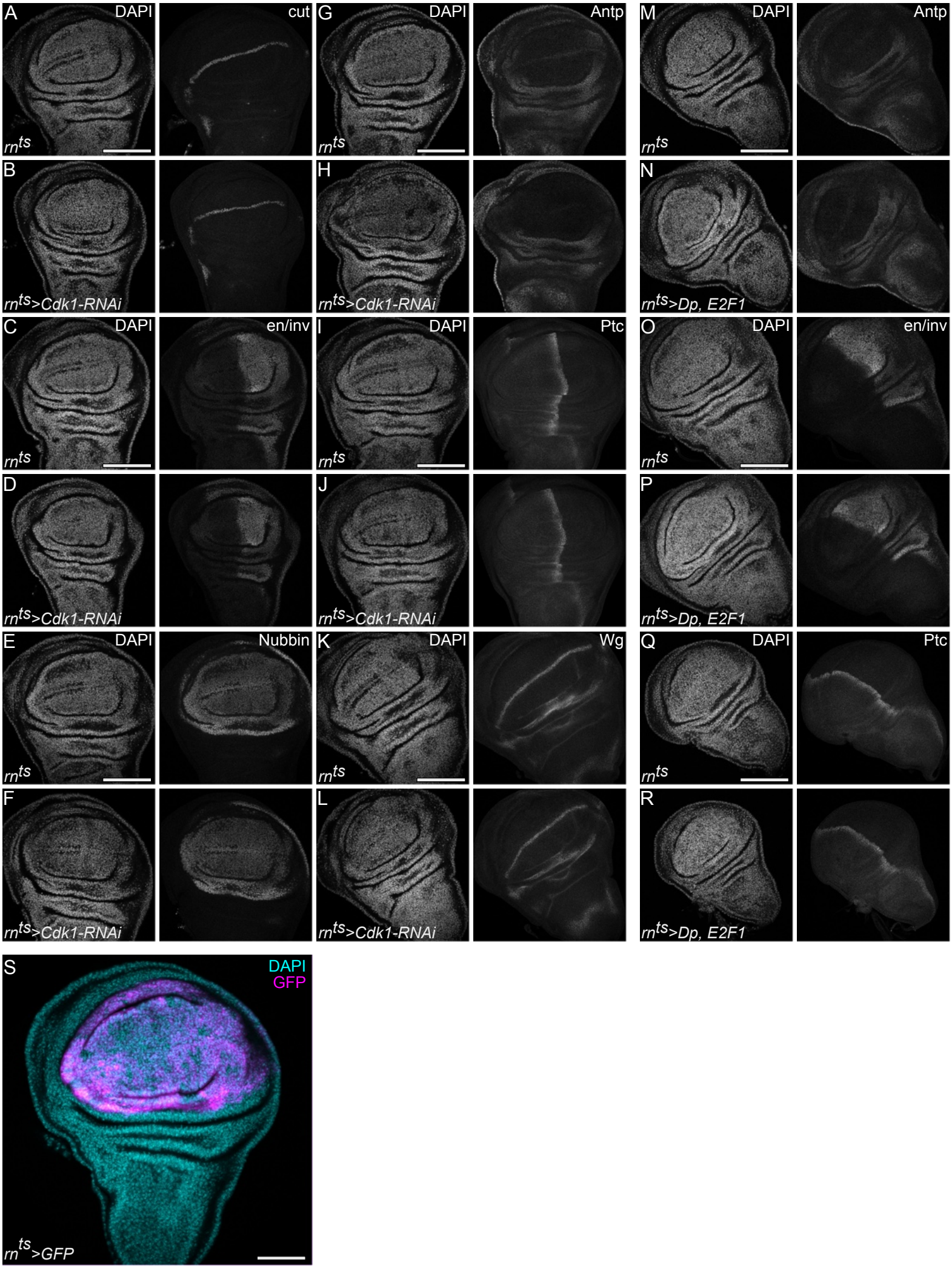
A
DAPI
cut
rn ts
B
rn ts>Cdk1-RNAi
C
DAPI
en/inv
rn ts
D
rn ts>Cdk1-RNAi
E
DAPI
Nubbin
rn ts
F
rn ts>Cdk1-RNAi
G
DAPI
Antp
rn ts
H
rn ts>Cdk1-RNAi
I
DAPI
Ptc
rn ts
J
rn ts>Cdk1-RNAi
K
DAPI
Wg
rn ts
L
rn ts>Cdk1-RNAi
M
DAPI
Antp
rn ts
N
rn ts>Dp, E2F1
O
DAPI
en/inv
rn ts
P
rn ts>Dp, E2F1
Q
DAPI
Ptc
rn ts
R
rn ts>Dp, E2F1
S
DAPI
GFP
rn ts>GFP

S3.2

Figure S3.2. Polycomb target gene expression remains stable despite altered cell cycle dynamics

---

A-L. Immunostaining for proteins expressed by Polycomb target genes: Cut **(A, B),** Engrailed/invected **(C, D),** Nubbin **(E, F),** Antennapedia **(G, H),** Patched **(I, J)** and Wingless **(K, L)** in control **(A, C, E, G, I, K)** and *Cdk1-RNAi*-expressing **(B, D, F, H, J, L)** wing discs.

M-R. Immunostaining for proteins expressed by Polycomb target genes: Antennapedia **(M, N),** Engrailed/i**nvected (O, P)** and Patched **(Q, R)** in control **(M, O, Q)** and *Dp, E2F1*-coexpressing **(N, P, R)** wing discs.

S. A control wing disc after 24 h of *UAS-GFP*-expression in the pouch (magenta), under the control of the *rn-GAL4* (*rotund-GAL4*) driver, displayed to reference the manipulated pouch domain in Figures A-R. Please note that this is the same disc shown in **Fig S1.1 A**.

Discs were stained with DAPI to visualize nuclei.
Sum projections of multiple confocal sections are shown in **A-S.**
Scale bars: 100 µm.

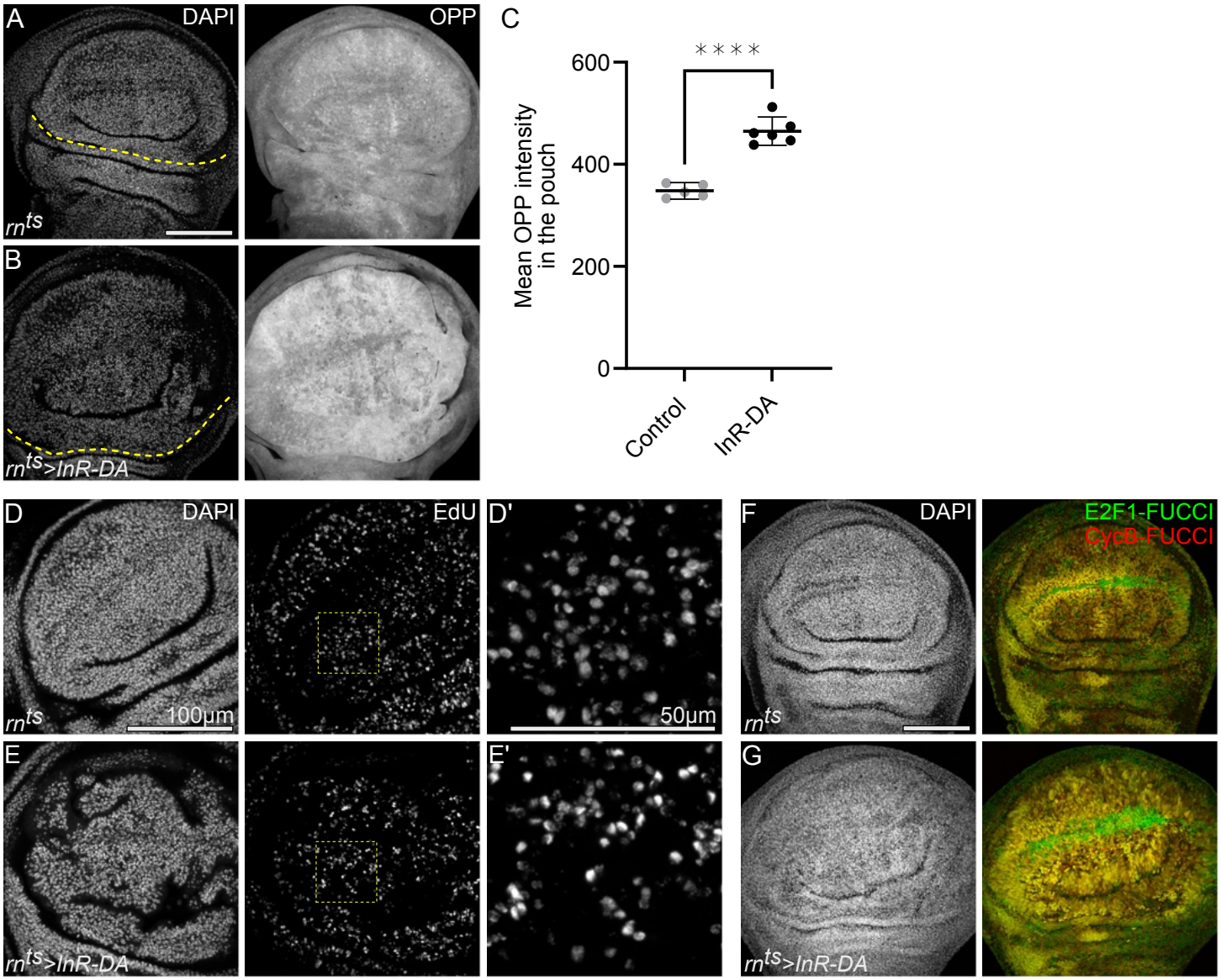
A
DAPI
OPP
rn^ts
B
rn^ts>InR-DA
C
****
600
400
200
0
Mean OPP intensity in the pouch
Control
InR-DA
D
DAPI
EdU
rn^ts
100µm
D'
50µm
F
DAPI
E2F1-FUCCI
CycB-FUCCI
rn^ts
E
rn^ts>InR-DA
E'
G
rn^ts>InR-DA

S4.1

Figure S4.1. Increased insulin signaling promotes faster proliferation and growth independent of changes to the distribution of cell cycle phases

---

A-B. Protein synthesis visualized by OPP incorporation in control **(A)** and *InR-DA*-expressing **(B)** discs. Yellow dashed lines indicate the boundary between the wing pouch and hinge regions. The area above the line corresponds to the *rn-GAL4* expression domain, while the area below represents wild-type cells. The *InR-DA*-expressing wing pouch exhibits higher rates of protein synthesis, reflecting an increased biosynthetic capacity promoted by higher InR/PI3K/Akt activity.

C. Quantification of mean OPP intensity in the pouch region of control and *InR-DA*-expressing discs. Mean and 95% CI is shown. Statistical significance was tested using two-tailed Unpaired t test, p value<0.0001. (control discs: n=5, *InR-DA*-expressing discs: n=6).

D-E. EdU incorporation visualizes DNA replication in the pouch region of control **(D)** and *InR-DA*-expressing **(E)** discs. Dashed yellow squares highlight the magnified regions shown in **(D',E')**. *InR-DA*-expressing wing pouch shows higher levels of EdU intensities, reflecting accelerated speed of DNA replication. Rates of EdU incorporation in *InR-DA*-expressing discs were previously reported and quantified (Crucianelli et al., 2022).

F-G. Cell cycle dynamics in control **(F)** and *InR-DA*-expressing **(G)** discs. FUCCI reporters *GFP-E2F1*$^{1-230}$ (green) and *mRFP-NLS-CycB*$^{1-266}$ (red) were used to visualize cell cycle phases. Note that expression of a constitutively active Insulin receptor does not alter the cell cycle phase profile of the wing pouch compared to control disc.

Discs were stained with DAPI to visualize nuclei.
Fluorescence intensities are reported as arbitrary units.
Maximum projections of multiple confocal sections are shown in **F-G.**
Sum projections of multiple confocal sections are shown in **A-B** and **D-E.**
Scale bars: 100 μm in **A,B**, **D,E**, **F,G;** 50 μm in zoomed-in **D,E.**

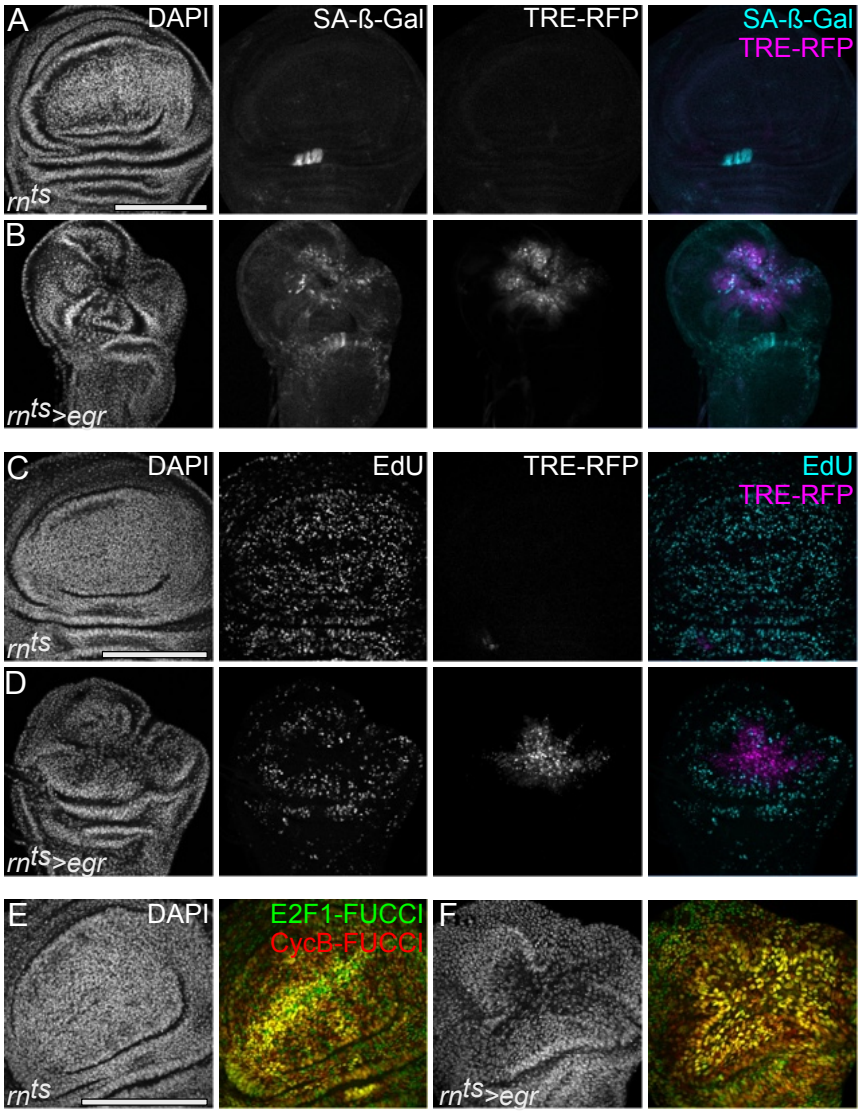
A
DAPI
SA-ß-Gal
TRE-RFP
SA-ß-Gal
TRE-RFP
rn^ts
B
rn^ts>egr
C
DAPI
EdU
TRE-RFP
EdU
TRE-RFP
rn^ts
D
rn^ts>egr
E
DAPI
E2F1-FUCCI
CycB-FUCCI
rn^ts
F
rn^ts>egr

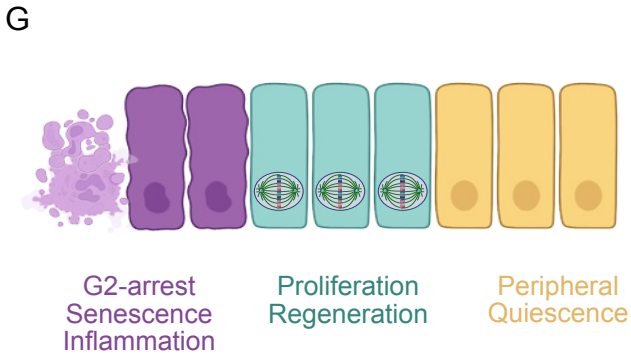
G
G2-arrest
Senescence
Inflammation
Proliferation
Regeneration
Peripheral
Quiescence

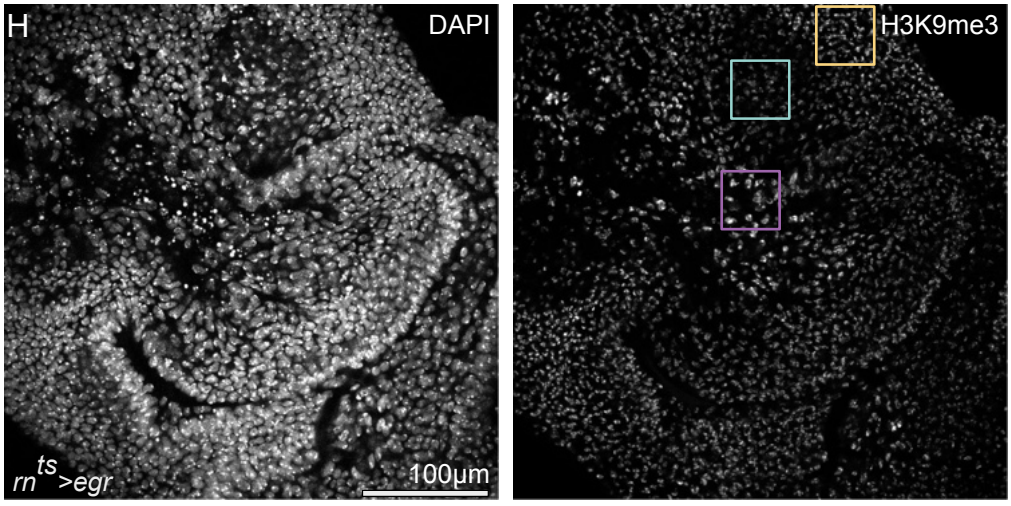
H
DAPI
H3K9me3
rn^ts>egr
100µm

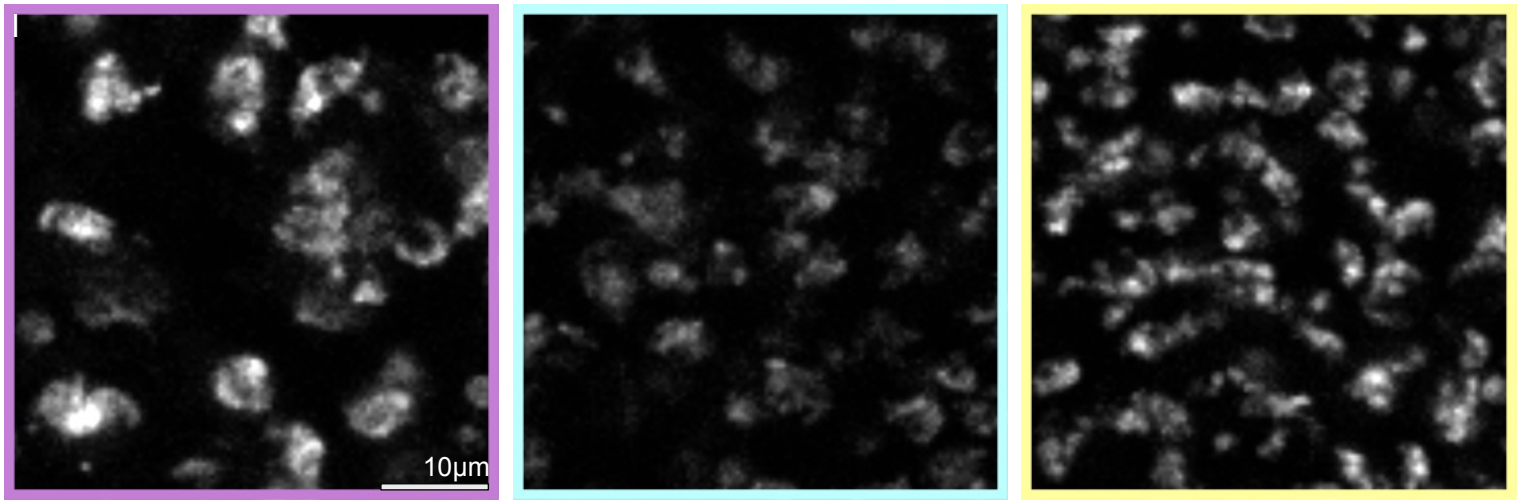
I
10µm

S4.2

Figure S4.2. Persistence methyltransferase activity drives H3K9me3 accumulation through metabolic changes coupled to a senescent cell cycle arrest

---

A-B. Senescence-associated β-galactosidase (SA-β-gal) activity (cyan or gray) in control **(A)** and *egr*-expressing **(B)** discs. TRE-RFP reporter (magenta) visualizes JNK-pathway activity. SA-β-gal activity in *egr*-expressing discs was previously reported and quantified (Jaiswal et al., 2023).

C-D. EdU incorporation (gray or cyan) visualizes DNA replication in control (B) and *egr*-expressing (D) discs. TRE-RFP reporter (magenta) visualizes JNK-pathway activity. EdU incorporation was previously reported and quantified (Jaiswal et al., 2023, Floc'hlay et al., 2023) .

E-F. Cell cycle dynamics in control **(E)** and *egr*-expressing **(F)** discs. FUCCI reporters *GFP-E2F1*$^{1-230}$ (green) and *mRFP-NLS-CycB*$^{1-266}$ (red) were used to visualize cell cycle phases.

G. A model illustrating inflammatory tissue damage in *Drosophila* wing imaginal discs. Eiger expression activates the JNK pathway, an early stress response, which induces a senescence-like cell-cycle arrest in the G2 phase at center of the tissue damage and triggers a senescence program (Cosolo et al., 2019). These arrested cells secrete Unpaired cytokines, which activate the JAK/STAT pathway in surrounding cells, promoting compensatory proliferation during tissue regeneration (Crucianelli et al., 2022; Floc'hlay et al., 2023; Herrera & Bach, 2019; Jaiswal et al., 2023; La Fortezza et al., 2016; Santabarbara-Ruiz et al., 2015; Worley et al., 2022). At the periphery of the damage site, cells remain in a quiescent state (Maya et al., 2024).

H-I. Immunostaining for H3K9me3 in *egr*-expressing disc **(H).** The magenta frame highlights G2-arrested senescent cells, which show elevated H3K9me3 levels. The cyan frame marks cells undergoing compensatory proliferation, where H3K9me3 levels are reduced. The yellow frame indicates quiescent cells, which have higher H3K9me3 levels than proliferating cells **(I).**

Discs were stained with DAPI to visualize nuclei.
Maximum projections of multiple confocal sections are shown in **H.**
Sum projections of multiple confocal sections are shown in **A-D** and **E-F.**
Scale bars: 100 µm in **A-B**, **C-D**, **E-F** and **H**; 10 µm in **I**.

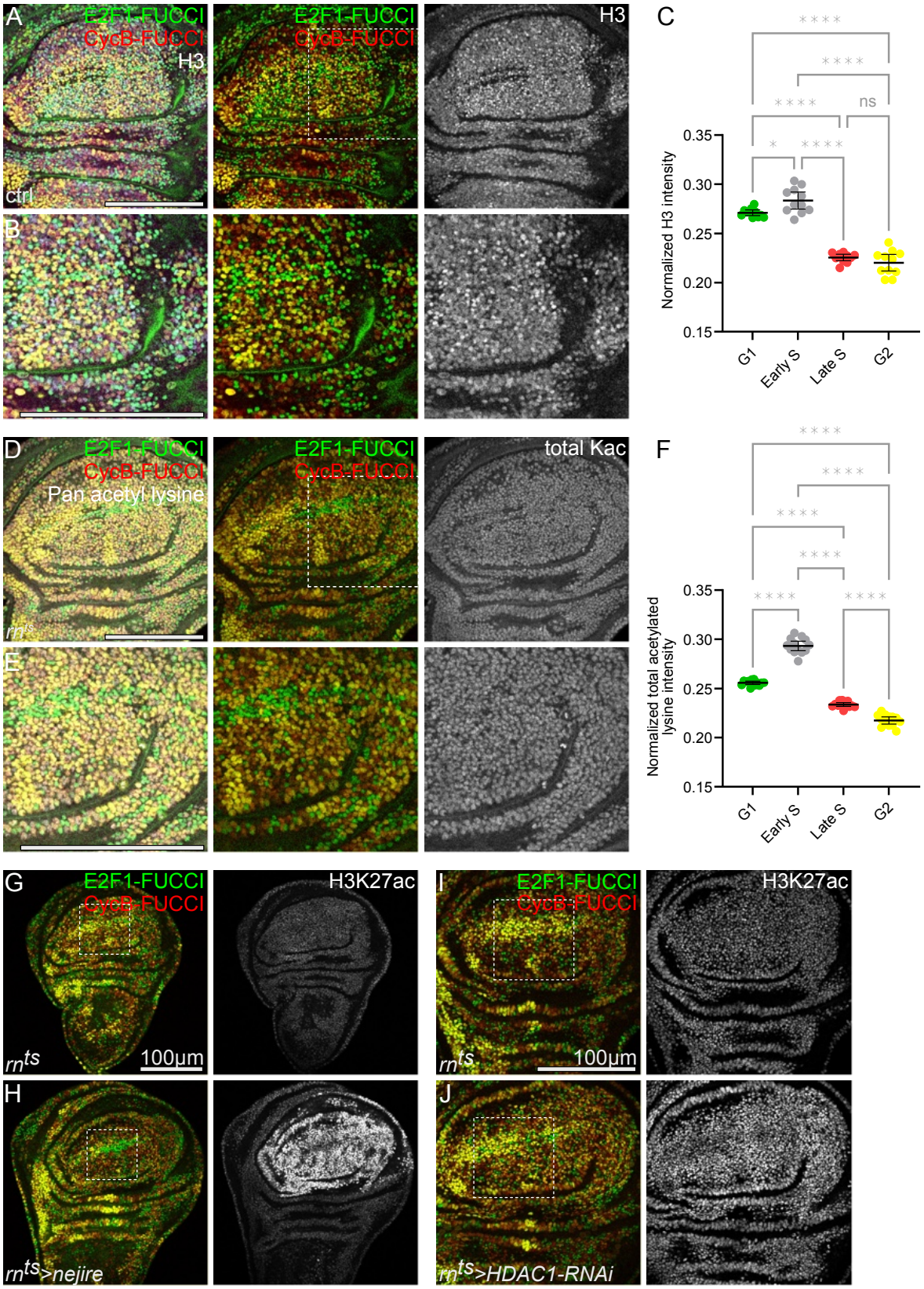
A
E2F1-FUCCI
CycB-FUCCI
H3
ctrl
B
C
Normalized H3 intensity
0.35
0.30
0.25
0.20
0.15
G1
Early S
Late S
G2
ns
D
Pan acetyl lysine
rn^ts
E
total Kac
F
Normalized total acetylated lysine intensity
G
H3K27ac
100µm
H
rn^ts>nejire
I
J
rn^ts>HDAC1-RNAi

S5.1

Figure S5.1. Total H3 and acetyl-lysine dynamics do not recapitulate the S phase-associated increase in H3K27ac

---

A-B. Immunostaining for H3 in a developing control disc **(A**), with a magnified region (demarcated by a white dashed square) shown in panel B, also expressing the FUCCI reporter (*GFP-E2F1*$^{1-230}$ (green) and *mRFP-NLS-CycB*$^{1-266}$ (red)) to visualize cell cycle phases.

C. Quantification of normalized H3 intensity level with respect to different cell cycle phases in the pouch region of control discs. Please note that normalization was performed against the average fluorescence intensity across all cell cycle phases. Mean and 95% CI is shown. Statistical significance was tested using Repeated Measures One-Way ANOVA followed by Tukey's post-hoc test for multiple comparison (n=11 discs). Adjusted p= 0.0192 for G1 vs. Early S; p<0.0001 for G1 vs. Late S; p<0.0001 for G1 vs. G2; p<0.0001 for Early S vs. Late S; p<0.0001 for Early S vs G2 and p=0.4147 for Late S vs G2.

D-E. Immunostaining for total acetylated lysine level in a developing control disc **(D),** with a magnified region (demarcated by a white dashed square) in panel E, also expressing the FUCCI reporters (*GFP-E2F1*$^{1-230}$ (green) and *mRFP-NLS-CycB*$^{1-266}$ (red)) to visualize cell cycle phases.

F. Quantification of normalized total acetylated lysine level in different cell cycle phases in the pouch region of control discs. Please note that normalization was performed against the average fluorescence intensity across all cell cycle phases. Mean and 95% CI is shown. Statistical significance was tested using Repeated Measures One-Way ANOVA followed by Tukey's post-hoc test for multiple comparison (n=13 discs). Adjusted p<0.0001 for G1 vs. Early S; p<0.0001 for G1 vs. Late S; p<0.0001 for G1 vs. G2; p<0.0001 for Early S vs. Late S; p<0.0001 for Early S vs G2 and p<0.0001 for Late S vs G2.

G-H. Immunostaining for H3K27ac in control **(G)** and *nejire*-expressing **(H)** discs, also expressing the FUCCI reporters (*GFP-E2F1*$^{1-230}$ (green) and *mRFP-NLS-CycB*$^{1-266}$ (red)) to visualize cell cycle phases. The location of magnified regions shown in Main Figure 5F and G is indicated by white dashed squares.

I-J. Immunostaining for H3K27ac in control **(I)** and *HDAC1-RNAi*-expressing **(J)** discs also expressing the FUCCI reporters (*GFP-E2F1*$^{1-230}$ (green) and *mRFP-NLS-CycB*$^{1-266}$ (red)) to visualize cell cycle phases. The location of magnified regions shown in Main Figure 5H and I is indicated by white dashed squares.

Fluorescence intensities are reported as arbitrary units.
Maximum projections of multiple confocal sections are shown in **D-E.**
Scale bars: 100 µm.

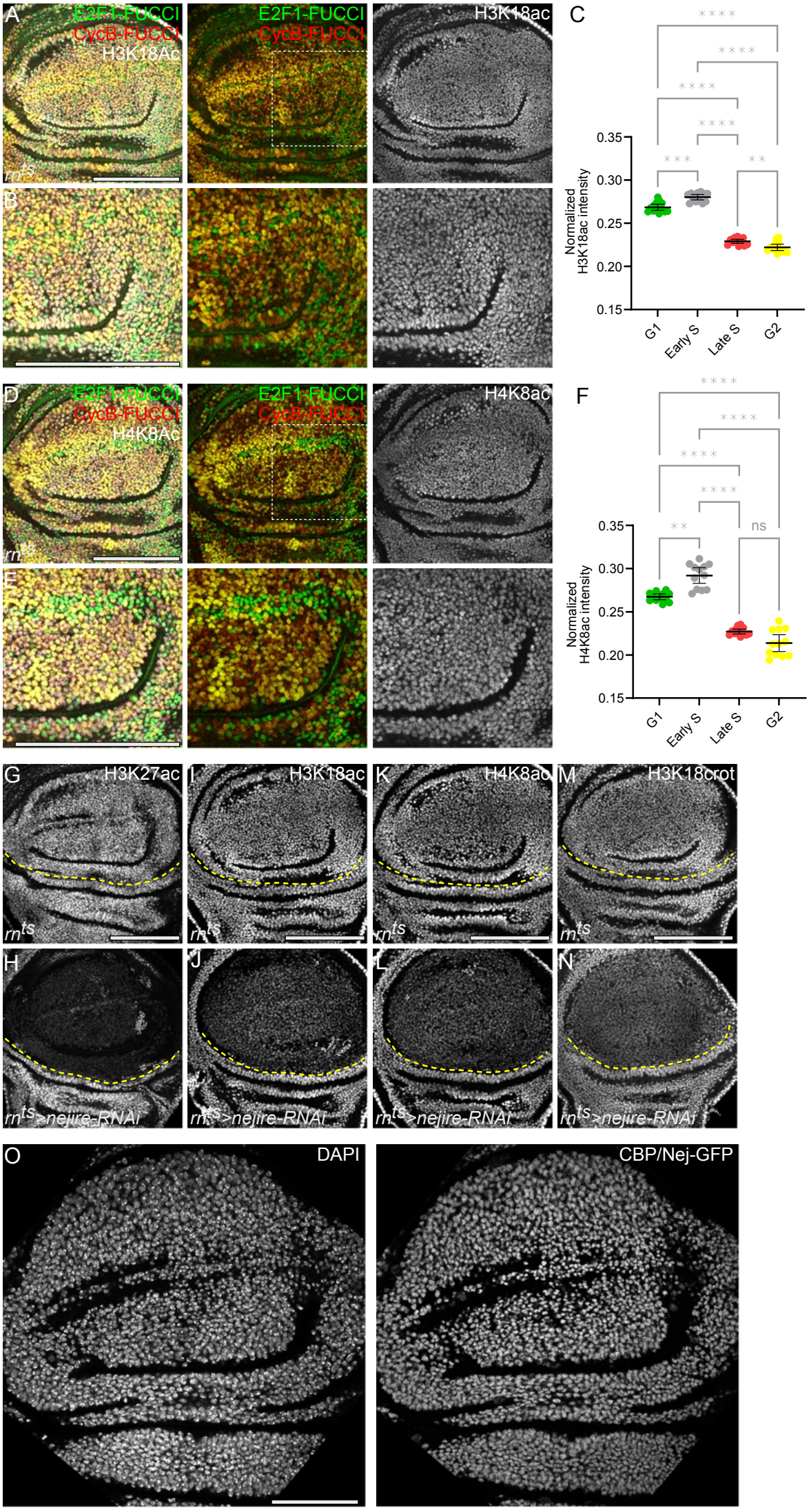
A
E2F1-FUCCI
CycB-FUCCI
H3K18Ac
H3K18ac
rn^ts
B
C
Normalized H3K18ac intensity
0.35
0.30
0.25
0.20
0.15
G1
Early S
Late S
G2
D
H4K8Ac
H4K8ac
E
F
Normalized H4K8ac intensity
ns
G
H3K27ac
I
H3K18ac
K
H4K8ac
M
H3K18crot
H
J
L
N
rn^ts>nejire-RNAi
O
DAPI
CBP/Nej-GFP

S5.2

Figure S5.2. Total H3K18ac and H4K8ac dynamics only partially recapitulate the S phase-associated increase in H3K27ac

---

A-B. Immunostaining for H3K18ac in a developing control disc **(A),** with a magnified region (demarcated by a white dashed square) in panel B, in the background of FUCCI reporters (*GFP-E2F1*$^{1-230}$ (green) and *mRFP-NLS-CycB*$^{1-266}$ (red)) to visualize cell cycle phases.

C. Quantification of normalized H3K18ac intensity level in different cell cycle phases in the pouch region of control discs. Please note that normalization was performed against the average fluorescence intensity across all cell cycle phases. Mean and 95% CI is shown. Statistical significance was tested using Repeated Measures One-Way ANOVA followed by Tukey's post-hoc test for multiple comparison (n=13 discs). Adjusted p=0.0003 for G1 vs. Early S; p<0.0001 for G1 vs. Late S; p<0.0001 for G1 vs. G2; p<0.0001 for Early S vs. Late S; p<0.0001 for Early S vs G2 and p=0.0042 for Late S vs G2.

D-E. Immunostaining for H4K8ac in a normally developing control disc **(D),** with a magnified region (demarcated by a white dashed square) in panel E, also expressing the FUCCI reporters (*GFP-E2F1*$^{1-230}$ (green) and *mRFP-NLS-CycB*$^{1-266}$ (red)) to visualize cell cycle phases.

F. Quantification of normalized H4K8ac intensity level in different cell cycle phases in the pouch region of control discs. Please note that normalization was performed against the average fluorescence intensity across all cell cycle phases. Mean and 95% CI is shown. Statistical significance was tested using Repeated Measures One-Way ANOVA followed by Tukey's post-hoc test for multiple comparison (n=12 discs). Adjusted p=0.0018 for G1 vs. Early S; p<0.0001 for G1 vs. Late S; p<0.0001 for G1 vs. G2; p<0.0001 for Early S vs. Late S; p<0.0001 for Early S vs G2 and p=0.1076 for Late S vs G2.

G-H. Immunostaining for H3K27ac in control **(G)** and *nejire-RNAi*-expressing **(H)** discs. Same disc is also shown in Figure 5D and E but repeated here to allow for direct comparison with **(I-N)**.

I-J. Immunostaining for H3K18ac in control **(I)** and *nejire-RNAi*-expressing **(J)** discs.

K-L. Immunostaining for H4K8ac in control **(K)** and *nejire-RNAi*-expressing **(L)** discs.

M-N. Immunostaining for H3K18crot in control **(M)** and *nejire-RNAi*-expressing **(N)** discs. Yellow dashed lines indicate the boundary between the wing pouch and hinge regions.

O. Expression of a Crisper-tagged CBP/nej-GFP (Marsh et al., 2025) in a developing disc.

Discs were stained with DAPI to visualize nuclei.

Fluorescence intensities are reported as arbitrary units.

Maximum projections of multiple confocal sections are shown in **A-B** and **D-E.**

Sum projections of multiple confocal sections are shown in **G-H, I-J, K-L** and **M-N.**

Scale bars: 100 µm

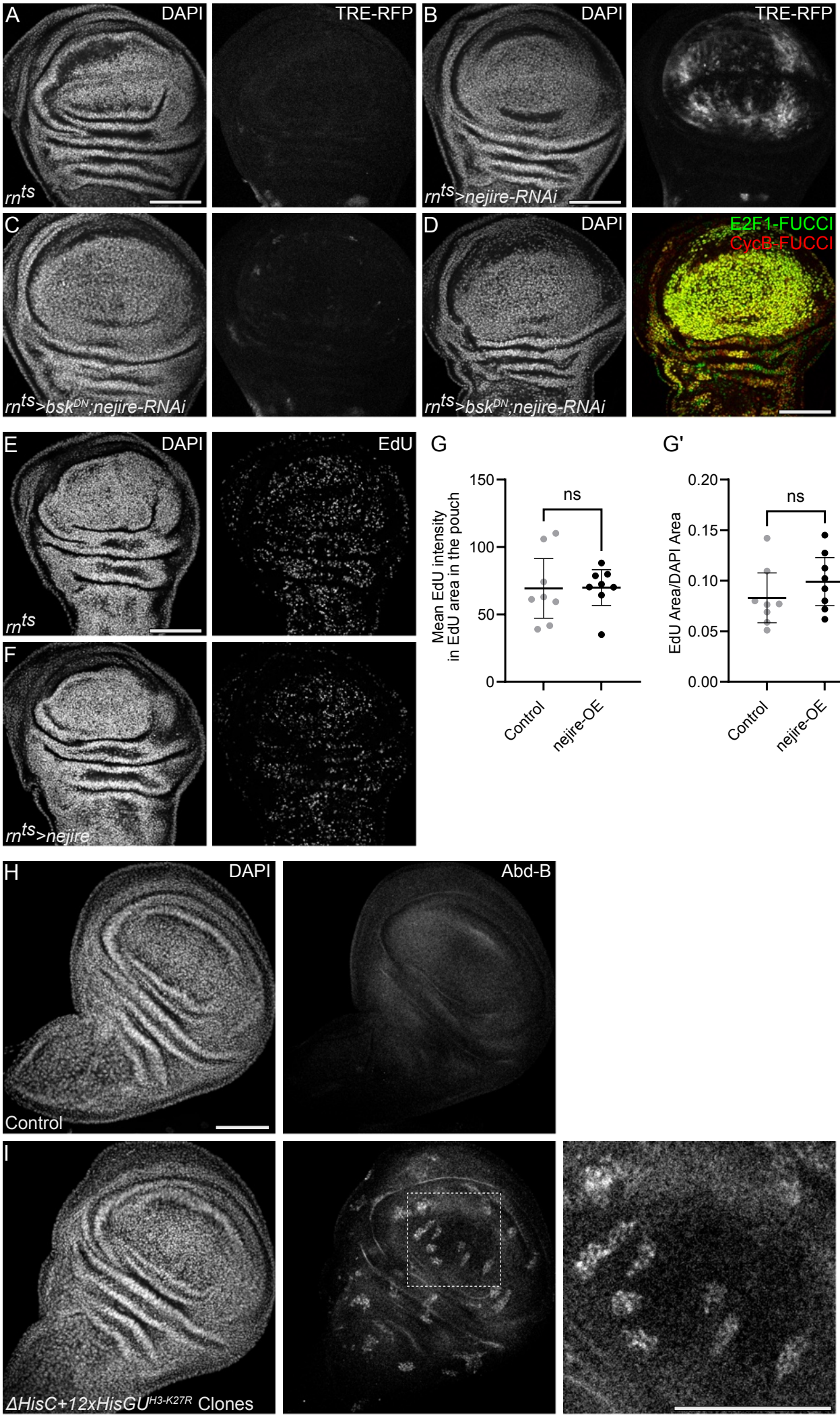
A
DAPI
TRE-RFP
rn^ts
B
DAPI
TRE-RFP
rn^ts>nejire-RNAi
C
rn^ts>bsk^DN;nejire-RNAi
D
DAPI
E2F1-FUCCI
CycB-FUCCI
rn^ts>bsk^DN;nejire-RNAi
E
DAPI
EdU
rn^ts
F
rn^ts>nejire
G
Mean EdU intensity in EdU area in the pouch
150
100
50
0
ns
Control
nejire-OE
G'
EdU Area/DAPI Area
0.20
0.15
0.10
0.05
0.00
ns
Control
nejire-OE
H
DAPI
Abd-B
Control
I
ΔHisC+12xHisGU^H3-K27R Clones

S6

Figure S6. CBP/nej and H3K27ac are required to prevent replication stress

A-C. Expression of the JNK pathway reporter TRE-RFP in control (A), *nejire-RNAi*-expressing (B) and *bsk*^{DN}, *nejire-RNAi*-coexpressing (C) discs.

D. Cell cycle dynamics in *bsk*^{DN}, *nejire-RNAi*-coexpressing (D) disc. FUCCI reporters *GFP-E2F1*$^{1-230}$ (green) and *mRFP-NLS-CycB*$^{1-266}$ (red) were used to visualize cell cycle phases. Even when JNK pathway activity is suppressed, one can still observe a shift of cells to the G2 phase of the cell cycle *nejire-RNAi*-expressing discs.

E-F. EdU incorporation to visualize DNA replication in the pouch region of control (E) and *nejire*- expressing (F) discs.

G. Quantification of mean EdU intensity per EdU area in the pouch region of control and *nejire*- expressing discs, serving as a proxy for speed of DNA replication. Mean and 95% CI are shown. Statistical significance was tested using two-tailed Mann Whitney test, p value=0.5737 (control discs: n=8, *nejire*-expressing discs: n=8).

G'. Quantification of EdU area per DAPI area in the pouch region of control and *nejire*-expressing discs, serving as a proxy number of cells undergoing DNA replication. Mean and 95% CI are shown. Statistical significance was tested using a two-tailed Mann Whitney test, p value=0.2345 (control discs: n=8, *nejire*-expressing discs: n=8).

H-I. Immunostaining for Abd-B in control discs **(H)** and in discs expressing *12×His-GU*$^{H3-K27R}$ transgenes and containing clones homozygous mutant for a deletion of the histone gene cluster *ΔHisC* **(I)**.

Discs were stained with DAPI to visualize nuclei.
Fluorescence intensities are reported as arbitrary units.
Sum projections of multiple confocal sections are shown in **A-C**, **E-F** and **H-I**.
Scale bars: 100 µm.